Versatile functions of bacterial exometabolites in microbe-microbe and plant-microbe interactions

Inaugural Dissertation

zur

Erlangung des Doktorgrades

der Mathematisch-Naturwissenschaftlichen Fakultät

der Universität zu Köln

vorgelegt von

Felix Ben Christopher Getzke

aus Bonn – Deutschland

Köln

2022

Die vorliegende Arbeit wurde am Max-Planck-Institut für Pflanzenzüchtungsforschung in Köln in der Abteilung für Pflanzen-Mikroben Interaktionen (Direktor: Prof. Dr. Paul Schulze-Lefert), in der Arbeitsgruppe von Dr. Stéphane Hacquard angefertigt.

Publications

Getzke, F., Thiergart, T., & Hacquard, S. (2019). **Contribution of bacterial-fungal balance to plant and animal health.** *Current opinion in microbiology*, *49*, 66–72.

Getzke, F., & Hacquard, S. (2022). **High-Throughput Profiling of Root-Associated Microbial Communities.** *Methods in molecular biology (Clifton, N.J.)*, *2494*, 325–337.

Getzke, F., Hassani, M. A., Crüsemann, M., Malisic, M., Zhang, P., Ishigaki, Y., Böhringer, N., Jiménez Fernández, A., Wang, L., Ordon, J., Ma, K.-W., Thiergart, T., Harbort, C. J., Wesseler, H., Miyauchi, S., Garrido-Oter, R., Shirasu, K., Schäberle, T. F., Hacquard, S. & Schulze-Lefert, P. **Co-functioning of bacterial exometabolites drives root microbiota establishment.** *In peer review*

Getzke, F., Wang, L., Denissen, N., Mesny, F., Ma, K.-W., Wesseler, H., Jiménez Fernández, A., Schulze-Lefert, P., Schäberle, T. F. & Hacquard, S. **Physicochemical interaction between osmotic stress and a bacterial secondary metabolite promotes plant disease.** *In preparation*

Vannier, N., **Getzke, F.**, Mesny, F., Dethier, L., Ordon, J., Thiergart, T. & Hacquard, S. **Meta-transcriptomic profiling of synthetic microbial communities identifies genes determining root-colonization potential.** *In preparation*

Kumar Basak, A., Piasecka, A., Hucklenbroich, J., Türksoy, G., Guan, R., Zhang, P., **Getzke, F.**, Garrido-Oter, R., Hacquard, S., Strzałka, K., Bednarek, P., Yamada, K. & Nakano, R. T. (2019). **Tryptophan specialized metabolism and ER body-resident myrosinases modulate root microbiota assembly.** *In preparation*

Table of contents

Abstract

In nature, roots of *Arabidopsis thaliana* are colonized by taxonomically diverse, soil-derived communities mainly comprising bacteria and fungi. Collectively, these root-associated microbial communities are termed root microbiota and are characterized by reduced microbial diversity and robust community structures compared to soil-associated communities. While plant secondary metabolism and the innate immune system have been demonstrated to influence root microbiota establishment, the role of microbial interactions and the underlying mechanisms for root microbiota establishment remain largely elusive. Using combinatorial approaches of binary interaction screens, forward and reverse genetics, targeted metabolomics, microbiota reconstitution, and marker gene amplicon sequencing-based community profiling, we provide genetic evidence for a root-specific functioning of bacterial secreted exometabolites in root microbiota establishment. We further demonstrate that a sole antimicrobial bacterial secondary metabolite is sufficient to cause plant disease under hyperosmotic conditions, illustrating the versatile role of these inhibitory molecules for microbe-microbe and host microbe interactions. Finally, we provide evidence for the modulation of microbial interactions by the availability of easily accessible carbon, collectively, suggesting that root exudates drive microbial interactions in the rhizosphere, likely contributing to the observed reduction of microbial diversity across the soil-root continuum. Collectively, our data demonstrate the relevance of bacterial exometabolites for root microbiota establishment and host health.

List of abbreviations

½ MS	½ Murashige and Skoog medium
16S	bacterial *16S* rRNA gene
Abs_{600}	absorption at 600 nm
ASV	amplicon sequence variant
A. thaliana	*Arabidopsis thaliana*
approx.	approximately
ARE	artificial root exudates
BFI	bacterial fungal interactions
BGC	biosynthetic gene cluster
C. hirsute	*Cardamine hirsute*
CAS	Cologne agricultural soil
Col-0	Columbia-0, *A. thaliana* accession
d	days
DAPG	2,4-diacetylphloroglucinol
DEG	differentially enriched gene
DNA	Deoxyribonucleic acid
dNTPs	deoxyribonucleotide triphosphate
dpi	days past inoculation
e.g.	lat, *exempli gratia*; eng, for example
et al.	lat, *et alii*; eng, and others
Fig.	Figure
Figure S1	supplementary figure 1
HK	heat-killed
i.e.	lat, *id est*; eng, that is
ITS1	fungal internally transcribed spacer 1
lat	Latin
MAMP	Microbe-associated molecular pattern
mBA	modified Burkholder assay
MES	2-ethanesulfonic acid
Milli-Q	ultrapure water
min	minute/ minutes
mini-Tn5	Tn5-derived mini transposon

n	number of
NADPH	reduced nicotinamide adenine dinucleotide phosphate
NO	nitric oxide
NRPS	non-ribosomal peptide synthetase
OD_{600}	optical density at 600 nm
OTU	operational taxonomic unit
PCR	polymerase chain reaction
PGB	potato glucose broth
PRR	pattern recognition receptor
RBO	respiratory burst oxidase
RBOHD	respiratory burst oxidase homologue D
ROS	reactive oxygen species
rpm	rounds per minute
Rs	*Ralstonia solanacearum*
RT	room temperature
s	second/ seconds
SN	supernatant
sp.	lat, *species*; eng, species
spp.	lat, *species pluralis*; eng, multiple species
SW	Sweden
Table S1	supplementary table 1
TSB	tryptic soy broth
v5v7	*16S* variable regions v5 to v7
WT	wild type

General introduction

Plant tissues are colonized by diverse microbial communities comprising mainly bacteria and fungi (Agler *et al.*, 2016; Bulgarelli *et al.*, 2012; Thiergart *et al.*, 2019). While detrimental and beneficial associations of plants with mutualistic or pathogenic microorganisms, respectively, have been studied extensively, the diversity of presumably neutral – *i.e.*, commensal – microorganisms has only been unrevealed recently (Bulgarelli *et al.*, 2012; Teixeira *et al.*, 2019; Trivedi *et al.*, 2020). Microbial assemblages associated with plant organs are collectively referred to as plant microbiota and have been demonstrated to fulfil a variety of functions for the host plant. This includes nutrient solubilisation in the rhizosphere – *i.e.*, the soil that is under the influence of plant exudates – and alleviation of abiotic stresses (Harbort *et al.*, 2020; Hiruma *et al.*, 2016; Hou *et al.*, 2021; Naylor *et al.*, 2017; L. Xu *et al.*, 2021). For instance, it has been shown that taxonomically diverse commensal fungi associating with roots of the non-mycorrhizal plant species *Arabidopsis thaliana* and *Arabis alpina* can facilitate plant growth under phosphate limiting conditions by provisioning phosphate to the host (Almario *et al.*, 2017; Bakshi *et al.*, 2015; Hiruma *et al.*, 2016). Root-secreted coumarins modulate the bacterial root microbiota of *A. thaliana* resulting in solubilisation of iron in the rhizosphere thereby enhancing plant growth (Harbort *et al.*, 2020). Furthermore, phytohormone production or degradation by commensal microorganisms can modulate plant development under favourable or stressed conditions (Conway *et al.*, 2022; Finkel *et al.*, 2020; Glick, 2014; F. Xu *et al.*, 2021). Collectively, this illustrates the involvement of the root microbiota in modulating diverse interactions of plants with their abiotic environment. Similarly, root-associated microorganisms can affect interactions of plants with their biotic environment. *A. thaliana* and *Zea maize* root exudation has been demonstrated to modulate the root microbiota across plant generations, resulting in increased protection towards leaf pathogenic *Pseudomonas syringae* and the herbivorous insect *Spodoptera frugiperda*, respectively (Hu *et al.*, 2018; Yuan *et al.*, 2018). Furthermore, the occurrence of sudden wilt disease caused by members of the fungal genus *Fusarium* has been linked to different soil types and soil microbiota composition (Schroth & Hancock, 1982). Microbiota transplants from disease suppressive soils to non-suppressive soils are sufficient to abolish disease symptoms (Santhanam *et al.*, 2015). *A. thaliana*, furthermore, relies on the bacterial fraction of its root microbiota for protection against root-colonizing fungi and for promoting fungal-host homeostasis (Durán *et al.*, 2018; Wolinska *et al.*, 2021). Collectively, this illustrates that the root microbiota is required for direct or indirect suppression of diverse biotic diseases in various plant species (Carrión *et al.*, 2019; Mendes *et al.*, 2011;

Raaijmakers & Weller, 1998; Tracanna *et al.*, 2021). As the plant microbiota fulfils various functions that are essential for the survival of the host, plant-associated microbial communities have become promising targets to improve plant survival and productivity in agricultural settings.

Informed and predictable application of individual microorganisms or microbial communities (*i.e.*, biologics) in agricultural settings, however, requires a molecular and ecological understanding of microbiota establishments and functions. In natural soils, edaphic factors – such as soil pH or iron availability – shape the soil microbiota that serve as inoculum for plant roots and shoots. Environmental and climatic factors further affect microbial – specifically fungal – community compositions (Bahram *et al.*, 2018; Thiergart *et al.*, 2019). The microbial diversity decreases from bulk soil towards plant surfaces and endospheric compartments, resulting in a clear separation of soil- and plant-associated microbial community structures (Bulgarelli *et al.*, 2012; Lundberg *et al.*, 2012; Thiergart *et al.*, 2019). This indicates that host induced factors are involved in shaping the plant microbiota and selecting for putatively beneficial microorganisms. Here, root secreted photoassimilates and secondary metabolites modulate the microbial composition at the root. For example, *A. thaliana* produces linage-specific β-thioglucosides – *i.e.*, glucosinolates – that are required for suppressing excessive proliferation of commensal fungi and modulating beneficial effects to the host (Hiruma *et al.*, 2016; Koprivova & Kopriva, 2022; Lahrmann *et al.*, 2015; Wolinska *et al.*, 2021). Root secreted secondary metabolites can also modulate bacterial activity. As indicated above, coumarins are essential for bacterial rescue of plant growth under iron limiting conditions (Harbort *et al.*, 2020). Similarly, the phytoalexin camalexin is required for beneficial associations of *A. thaliana* with two *Pseudomonas spp.* isolates (Root9 and CH267; Koprivova *et al.*, 2019). Collectively, this demonstrates that root exudates can restrict or enhance root association with diverse microbiota members with cascading consequences for host health.

The initial layer of the plant innate immune system detects both pathogenic and commensal microorganisms due to a large overlap in immunogenic microbial-associated molecular patterns (MAMPs) irrespective of microbial lifestyle (Ma *et al.*, 2021; Teixeira *et al.*, 2019; Teixeira *et al.*, 2021). Root commensals have developed molecular tools to suppress MAMP-triggered immunity (Garrido-Oter *et al.*, 2018; Ma *et al.*, 2021; Teixeira *et al.*, 2021; Yu *et al.*, 2019). The widespread occurrence of this immune-suppressive trait in approx. 40% of all tested *A. thaliana* root-derived bacterial isolates supports an involvement of the plant immune system in root microbiota establishment (Ma *et al.*, 2021; Teixeira *et al.*, 2021; Yu *et al.*, 2019).

Furthermore, the production of reactive oxygen species (ROS) restricts bacterial colonisation in the *A. thaliana* rhizosphere (Song *et al.*, 2021). Similarly, in aerial tissues ROS production *via* the NADPH-dependent respiratory burst oxidase RBOHD is required for microbiota homeostasis and suppression of microbiota-induced disease symptoms (Pfeilmeier *et al.*, 2021). Furthermore, the immunocompromised *A. thaliana* quadruple mutants *atmin7 fls2 efr cerk1* (*mfec*) and *atmin7 bak1-5 bkk1-1 cerk1* (*mbbc*) showed extensive proliferation of commensal bacteria and development of chlorotic lesions, indicative of disease (Xin *et al.*, 2016). Collectively, this demonstrates that the plant innate immune system and its interplay with microbiota members is required in the establishment and homeostasis of plant-associated microbial communities.

It is further believed that interactions between microbial organisms are involved in the establishment of the plant-associated microbial communities. Microbial mechanisms that lead to both cooperative and competitive interactions between individual microbiota members have been extensively studied in the past. While cooperative interactions *via* metabolic interdependencies have been described in microorganisms from nutrient poor environments (Harcombe, 2010; Hassani *et al.*, 2018; Mataigne *et al.*, 2022; Wintermute & Silver, 2010), evidence for the occurrence of nutrient interdependencies in *e.g.*, the carbon-rich rhizosphere is still lacking. Fungi have been proposed to facilitate bacterial root colonisation through bacterial migration along fungal hyphae – so called 'fungal highways' (Kohlmeier *et al.*, 2005; Worrich *et al.*, 2016; Y. Zhang *et al.*, 2018). Competitive intermicrobial interactions have been described primarily in the context of pathogen suppression. The production of bacterial or fungal exometabolites with cytotoxic or cytostatic activity have been intensively studied, resulting in the descriptions of antimicrobials with various modes of actions (Crits-Christoph *et al.*, 2018; Dimkic *et al.*, 2017; Dimkić *et al.*, 2022; Falardeau *et al.*, 2013; Keel *et al.*, 1992; Rajniak *et al.*, 2018). Furthermore, secreted enzymes, such as chitinases or lysozymes can contribute to pathogen suppression *via* contact independent mechanisms (Eitzen *et al.*, n.d.; Hjort *et al.*, 2009; Kobayashi *et al.*, 2002; Z. Zhang & Yuen, 2007). Furthermore, bacteria engage in contact-depending killing of competitors *via* type IV or type VI secretion system-mediated effector translocation (de Maayer *et al.*, 2011; Haapalainen *et al.*, 2012; Ho *et al.*, 2014; Purtschert-Montenegro *et al.*, 2022; Records, 2011; Russell *et al.*, 2014). Collectively, diverse mechanisms utilized by microorganisms to engage in primarily competitive interactions have been well characterised, however, the contribution of these mechanisms to plant microbiota establishment remains elusive.

Here, we aim at shedding light on the impact of microbe-microbe interactions on *A. thaliana* root microbiota establishment and the impact thereof on host health. In **Chapter I**, we systematically assess interbacterial interactions mediated by bacterial secondary exometabolites. Using metabolomics, genetics, and microbiota reconstitution experiments, we provide evidence for a contribution of bacterial exometabolites in shaping the root-associated microbiota and the reduction in bacterial diversity along the soil-root continuum. In **Chapter II**, we identify a bacterial secondary metabolite with antifungal and antibacterial activity to be causal for plant disease caused by an opportunistic root pathogen. We demonstrate a root-specific virulence mechanism caused by physicochemical interaction of the produced metabolite with hyperosmotic conditions in the rhizosphere. In **Chapter III**, we establish a minimal synthetic community comprising bacteria and fungi based on continental-scale ecological data. Using systematic assessment of all competitive and cooperative pairwise interactions under two nutritional regimes, we provide evidence for easily accessible carbon-dependent modulation of interkingdom interactions that is likely explaining the protectiveness of bacterial root commensals towards detrimental fungal communities. Collectively, we demonstrate the involvement of microbe-microbe interactions and inhibitory bacterial secondary metabolites in root microbiota establishment and plant health.

Chapter I: Co-functioning of bacterial exometabolites drives root microbiota establishment

Authors

Felix Getzke[1,12], M. Amine Hassani[1,9,12], Max Crüsemann[2], Milena Malisic[1,3], Pengfan Zhang[1], Yuji Ishigaki[4], Nils Böhringer[5,6], Alicia Jiménez Fernández[1], Lei Wang[5], Jana Ordon[1], Ka-Wai Ma[1], Thorsten Thiergart[1], Christopher J. Harbort[1,10], Hidde Wesseler[1], Shingo Miyauchi[1,3,11], Ruben Garrido-Oter[1,3], Ken Shirasu[4,7], Till F. Schäberle[5,6,8], Stéphane Hacquard[1,3,*] , Paul Schulze-Lefert[1,3,*]

Affiliations

1 Department of Plant Microbe Interactions, Max Planck Institute for Plant Breeding Research, 50829 Cologne, Germany

2 Institute for Pharmaceutical Biology, University of Bonn, 53115 Bonn, Germany

3 Cluster of Excellence on Plant Sciences (CEPLAS), Max Planck Institute for Plant Breeding Research, 50829 Cologne, Germany

4 RIKEN Center for Sustainable Resource Science, Yokohama, 230-0045, Japan

5 Institute for Insect Biotechnology, Justus-Liebig-University Giessen, 35392 Giessen, Germany.

6 German Centre for Infection Research (DZIF), Partner Site Giessen-Marburg-Langen, 35392 Giessen, Germany

7 Graduate School of Agricultural and Life Sciences, The University of Tokyo, 113-8657 Tokyo, Japan

8 Fraunhofer Institute for Molecular Biology and Applied Ecology (IME), Branch for Bioresources, 35392 Giessen, Germany

9 Present address: Department of Plant Pathology and Ecology, The Connecticut Agricultural Experiment Station, 123 Huntington Street, New Haven 06511, CT USA.

10 Present address: Max Planck Institute for Infection Biology, Department of Cellular Microbiology, Berlin 10117, Germany

11 Present address: Okinawa Institute of Science & Technology Graduate University, 1919–1 Tancha, Onna-son, Okinawa 904–0495, Japan

12 These authors contributed equally

***Correspondence: Stéphane Hacquard – hacquard@mpipz.mpg.de; Paul Schulze-Lefert – schlef@mpipz.mpg.de**

I.1 Summary

Soil-dwelling microbes are the principal inoculum for the root microbiota, but the role of microbe-microbe interactions in microbiota establishment remains fragmentary. We tested 39,006 binary interbacterial interactions for inhibitory activities *in vitro*, allowing us to identify taxonomic signatures in bacterial inhibition profiles. Using genetic and metabolomic approaches, we identified the antimicrobial 2,4-diacetylphloroglucinol and the iron-chelator pyoverdine as exometabolites whose combined functions explain most of the inhibitory activity of the strongly antagonistic *Pseudomonas brassicacearum* R401. Microbiota reconstitution with a core of *Arabidopsis thaliana* root commensals in the presence of wild-type or mutant strains revealed a root niche-specific co-function of these exometabolites as root competence determinants and drivers of predictable changes in the root-associated community. In natural environments, both corresponding biosynthetic operons are enriched in roots, a pattern likely linked to their role as iron sinks, indicating that these co-functioning exometabolites are adaptive traits contributing to pseudomonad pervasiveness throughout the root microbiota.

Keywords
root microbiome, microbe-microbe interactions, synthetic ecology, competition, niche competition, antimicrobials, iron nutrition, secondary metabolites, microbiota

I.2 Author contributions

P.S.-L., S.H., M.A.H. and F.G. developed the project. F.G., M.A.H., M.M., M.C., T.F.S., S.H., and P.S.-L. designed experiments. F.G., M.C., N.B. and M.M. generated the figures. M.A.H. performed the initial mBA experiments. Y.I. and K.S. performed the initial *Rs* mBA experiments. F.G. performed all subsequent mBA experiments. S.M. assembled the R401 genome. P.Z., R.G.-O. and F.G. predicted and analysed the BGCs. M.A.H., M.C. and T.F.S. performed the untargeted MS experiments. A.J.F., H.W. and F.G. generated the R401 mutants. A.J.F and F.G. established the R401 Tn5 mutant library and established the forward genetic screen. N.B., L.W. and T.F.S. performed MS experiments on R401 DAPG and pyoverdine. J.O. and K.-W.M. established the R569 Tn5 mutant library. M.M. and C.J.H. identified R569 pyoverdine mutants. M.M., C.J.H. and F.G. performed siderophore assays. F.G. performed SynCom reconstitution experiments, mono-association experiments, and bacterial growth assays. T.T. generated ASV tables. P.S.-L. and S.H. supervised the project. F.G., S.H. and P.S.-L. wrote this chapter.

I.3 Introduction

The establishment of the plant root microbiota from the soil biome is a multi-step process involving an interplay between edaphic/climatic factors, the host, and its microbiota, as well as an additional layer of complexity in the form of microbe-microbe interactions (Durán *et al.*, 2018; Naylor *et al.*, 2017; Song *et al.*, 2021; Thiergart *et al.*, 2020; Wippel *et al.*, 2021). These bacterial communities – collectively referred to as the root microbiota – assist the host in mobilizing mineral nutrients for plant nutrition, provide tolerance to abiotic stresses (Castrillo *et al.*, 2017; Harbort *et al.*, 2020; Hou *et al.*, 2021; Santos-Medellín *et al.*, 2021; Xu *et al.*, 2021) and furnish plants with indirect protection against soil-borne fungal pathogens or modulate the host's innate immune response (Carrión *et al.*, 2019; Durán *et al.*, 2018; Ma *et al.*, 2021; Teixeira *et al.*, 2021). Reduced taxonomic diversity and class-level dominance of Alpha-, Beta-, and Gammaproteobacteria, Actinobacteria, Flavobacteriia, and Bacilli are hallmarks of the root microbiota (Bai *et al.*, 2015; Bulgarelli *et al.*, 2012; Lundberg *et al.*, 2012).

Host genetic determinants underlying root microbiota establishment have been extensively studied (Pascale *et al.*, 2020) and include carbon-rich photoassimilates (*i.e.*, primary metabolites) that are continuously released by plants in the rhizosphere, acting as key mediators of root microbiota assembly and activity (Eilers *et al.*, 2010a; Ling *et al.*, 2022; Wippel *et al.*, 2021). Apart from host-derived metabolites, it is conceivable that specialised metabolites produced by root commensals also contribute to the establishment of the microbiota, as these molecules may be responsible for cooperative or competitive relationships with other bacterial taxa. In particular, specialised inhibitory metabolites (Clough *et al.*, 2022; Dimkić *et al.*, 2022; Fira *et al.*, 2018) are often produced by complex and energetically costly enzymatic mechanisms encoded by biosynthetic gene clusters (BGCs; Charlop-Powers *et al.*, 2014; Crits-Christoph *et al.*, 2018). These molecules have been primarily described in the context of antimicrobial discovery and pathogen suppression and display diverse antagonistic activities, including inhibition of prokaryotic cell wall biosynthesis, pore formation in the cell envelope, or inhibition of ATP biosynthesis (Dimkic *et al.*, 2017; Falardeau *et al.*, 2013; Jasim *et al.*, 2016; Kwak *et al.*, 2011; Makovitzki *et al.*, 2006). For example, the antimicrobial 2,4-diacetylphloroglucinol (DAPG) from fluorescent *Pseudomonas* strains plays a dominant role in suppressing the fungal-elicited take-all disease that affects the roots of grass and cereal plants in temperate climates and has been demonstrated to inhibit bacteria as well (Isnansetyo *et al.*, 2003; Julian *et al.*, 2020; Keel *et al.*, 1992; Lanteigne *et al.*, 2012; Raaijmakers & Weller, 1998; H. Zhou *et al.*, 2005; T. T. Zhou *et al.*, 2014). Furthermore, suppression of tomato infections

with pathogenic *Ralstonia solanacearum* can be achieved by chelating inorganic iron with bacterial siderophores that cannot be taken up by the pathogen, including pyoverdines, while growth-promoting siderophores facilitate infections of this bacterial root pathogen (Gu, Wei, *et al.*, 2020; Gu, Yang, *et al.*, 2020). *In vitro*, pyoverdine from *P. chlororaphis* YL-1 inhibits Gram-positive and -negative bacteria in an iron concentration dependent manner and is required for the suppression of the leaf pathogen *Xanthomonas oryzae pv. oryzae* in rice (Liu *et al.*, 2021). However, it remains unknown whether such specialised exometabolites contribute to root microbiota differentiation from the surrounding soil-biome.

Here, we assessed the prevalence of antagonistic binary interactions within the root microbiota using a collection of *A. thaliana* root-derived commensals comprising all six core classes of root-associated bacteria (Bai *et al.*, 2015). Applying genetic, genomic and metabolomic approaches, we identify the antimicrobial DAPG and the high-affinity iron-chelator pyoverdine as exometabolites underpinning the activities of the highly antagonistic *Pseudomonas brassicacearum* R401. Although the two exometabolites employ different modes of action, they co-function as R401 root competence determinants and influence key ecological indices of the synthetic root microbiota based on their inhibitory activities *in vitro*. Surveys of the genomes of bacterial culture collections from plants grown in natural environments suggest that these specialized exometabolites might act as adaptive traits that contribute to the pervasiveness of the genus *Pseudomonas* in the root microbiota.

I.4 Results

I.4.1 Widespread production of specialised exometabolites among root-associated bacteria

To investigate the prevalence of interbacterial competition mediated by secreted metabolites (hereafter referred to as exometabolites), we used a modified Burkholder plate-based assay (mBA; Burkholder *et al.*, 1966; **Fig. S1A**) and tested 39,006 binary interbacterial interactions, *i.e.*, 198 producer *versus* 198 target isolates. We detected an inhibition halo in 1,011 interactions (*i.e.*, 2.6% of tested pairwise interactions involving 66% of the isolates, **Fig. S1B, Table S1**), suggesting antibiosis due to specialised exometabolites. Antagonistic interactions were detected between all bacterial classes tested, indicating that the production of exometabolites is common in the *At*-RSphere culture collection of commensals (Bai *et al.* 2015). Actinobacteria isolates were most sensitive to all other classes, especially to Gammaproteobacteria, which showed the highest aggregated frequency and average intensity of inhibitory activities (**Fig. 1A**). Since we observed taxonomic signals at the class level, we calculated the average halo of inhibition size for all target and producer isolates across all bacterial classes tested (see sensitivity scores in **Fig. 1B** and inhibition scores in **Fig. 1C**, see also **Fig. S1B**). This revealed that only a few bacteria – mainly belonging to Pseudomonadaceae (R9, R68, R71, R329, R401, R562, and R569) – exhibited broad inhibition of phylogenetically diverse isolates (**Fig. 1C**). Extensive strain-specific variation in inhibition scores across closely related bacteria was observed, suggesting large standing genetic variation for the production of bacterial exometabolites among root-derived isolates **(Fig. 1C)**. Finally, we observed a 2.7x higher inhibitory activity for root-derived bacteria compared to those originating from soil ($p=0.011$; Kruskal-Wallis followed by Dunn's post-hoc test and Benjamini-Hochberg correction, **Fig. 1D**), suggesting that the production of exometabolites might be advantageous for bacterial root colonisation.

Ralstonia spp. are core members of the root microbiota of healthy *Arabidopsis* plants in nature (Thiergart *et al.* 2021). We hypothesized that the bacterial root microbiota of *A. thaliana* contributes to preventing disease in natural environments and tested the inhibitory activities of 167 of the aforementioned bacteria against pathogenic *Ralstonia solanacearum* GMI1000 (hereafter referred to as *Rs*; Boucher *et al.*, 1985; **Fig. 1C**). A subset of root- and soil-derived bacteria inhibited the growth of *Rs* in mBA experiments (10.9% and 10.3%, respectively). These inhibitory activities were mainly manifested by bacteria from three genera: *Pseudomonas*, *Streptomyces,* and *Bacillus* (**Fig. 1C**).

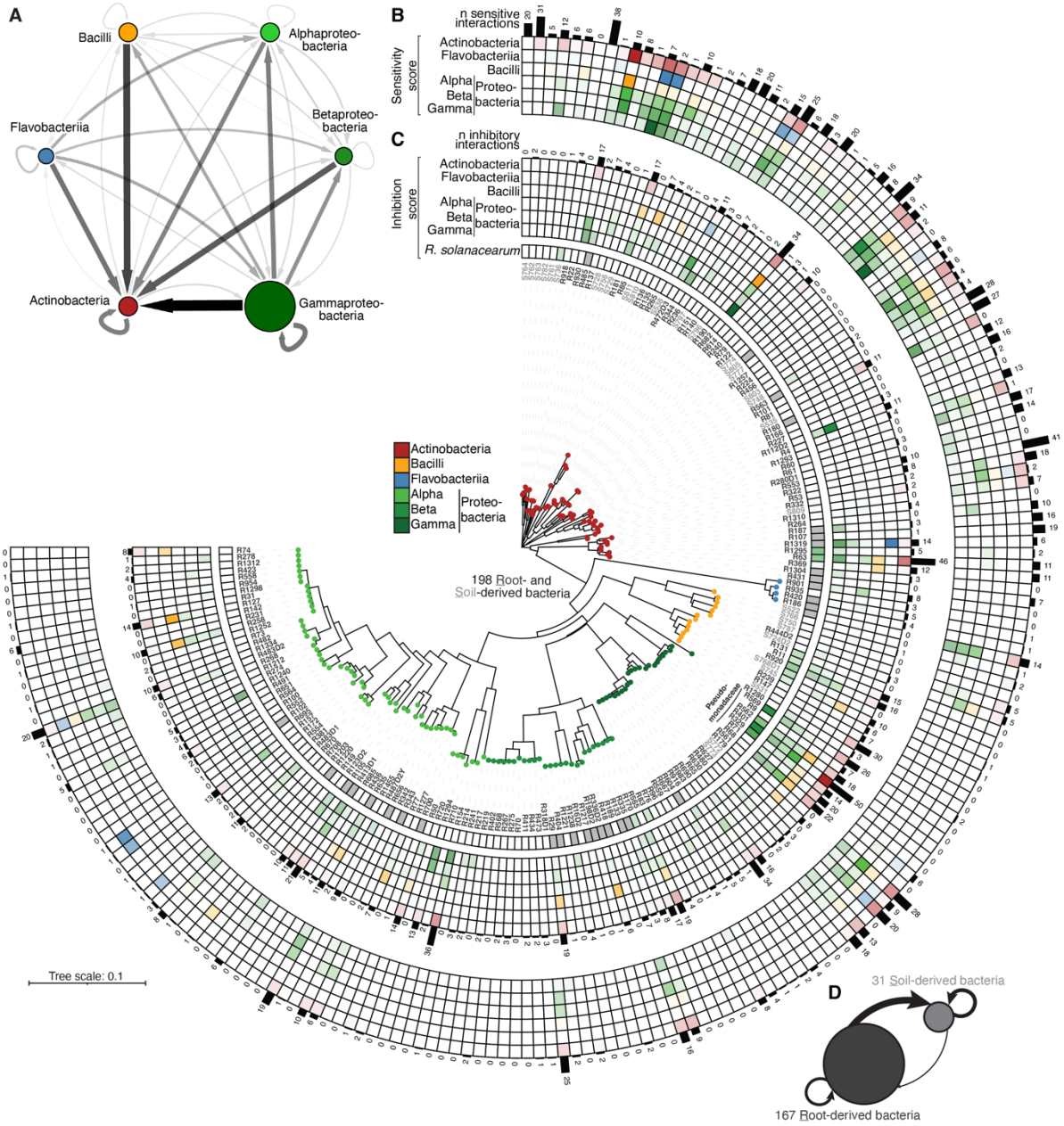

Figure 1 Widespread production of specialised exometabolites among root- and soil-derived bacteria. **(A)** Inhibitory interaction network computed based on binary interaction data from a modified Burkholder assay (mBA; n = 198 strains, 39,006 pairwise combinations tested, 1-2 biological replicates). Edge width and colour depicts the aggregated frequency of inhibitions at the class level while node size indicates the mean halo size, measured at 4 days post-inoculation (dpi). Arrows reflect inhibition directionality and intensity. For the complete list of interactions see **Table S1**. **(B–C)** Phylogenetic tree showing inhibition and sensitivity scores for each strain. The tree was built based on the full-length 16S rRNA gene sequences of 167 root- (dark grey) and 31 soil-derived (light grey) bacteria. All bacteria were reciprocally screened against each other and against *Ralstonia solanacearum* GMI1000. For each strain, sensitivity scores (average sensitivity of a strain to exometabolites produced by a given bacterial class **(B)** and inhibition scores (average exometabolites-dependent inhibition of a given strain to a bacterial class **(C)** are shown in the outer and inner heatmap, respectively. These scores represent the average halo size for a given strain at the class level as determined by a mBA. The number ('n') of sensitivities per strain and the number of inhibitory interactions is indicated by black bars. **(D)** Network showing the aggregated frequency of inhibitions measured for root- and soil-derived bacteria. Node size indicates the mean magnitude of inhibitions from mBA experiments. Arrows reflect inhibition directionality and intensity.

I.4.2 Genomic capacity for specialised metabolite production explains pronounced inhibitory activity

We hypothesized that the ability to produce halos of inhibitions might be correlated with the genome-encoded potential for the biosynthesis of specialized metabolites. We predicted BGCs for all strains tested in mBA experiments (**Table S2**) and tested whether halo-producer strains encode more BGCs than non-producers. The total number of BGCs was significantly increased in the antagonistic isolates ($p = 0.0166$). Furthermore, BGCs with putative involvement in the biosynthesis of non-ribosomal-peptides (NRPS), aryl polyene and redox-cofactors were significantly enriched in halo-producing isolates compared to nonproducers (**Fig. 2A**), suggesting that these compounds may be important for interbacterial competition.

Using liquid chromatography-tandem mass spectrometry (UPLC-MS/MS), we investigated the diversity of bacterial metabolites that could explain the observed interaction profiles. Network analysis of the resulting mass spectra revealed 247 families of molecules with similar fragmentation patterns, each representing at least two structurally related analogues (**Fig. S2**). While 2,220 nodes were shared between multiple classes, the remaining 1,094 nodes were found to be produced only by individual bacterial classes. Here, Gammaproteobacteria showed the greatest diversity of class-specific metabolites, indicating that their pronounced inhibitory activity (**Fig. 1C**) can be explained by the production of an enormous diversity of specialised metabolites.

To determine whether bacteria secrete an increased diversity of specialised metabolites upon interactions with competitors (Cornforth & Foster, 2013), we analysed metabolite mass spectra of 16 inhibitory zones from 10 producer isolates (R63, R71, R68, R342, R401, R562, R569, R690, R920 and R1310) with broad inhibitory activity against three target isolates (R472D3, R480 and R553) using the same workflow and compared them with the data of the individually cultured strains in a separate network. This revealed 224 new nodes secreted exclusively upon interaction with competing isolates (**Fig. 2B**). Dereplication of the interaction metabolome revealed that the biosynthesis of polyketides, such as two additional congeners of the nactin antibiotics and peptidic compounds, such as cyclo(Trp-Pro) and congeners of a novel lipopeptide family, was specifically triggered by interactions with other bacterial strains, pointing to a possible role of these molecules in interbacterial competition.

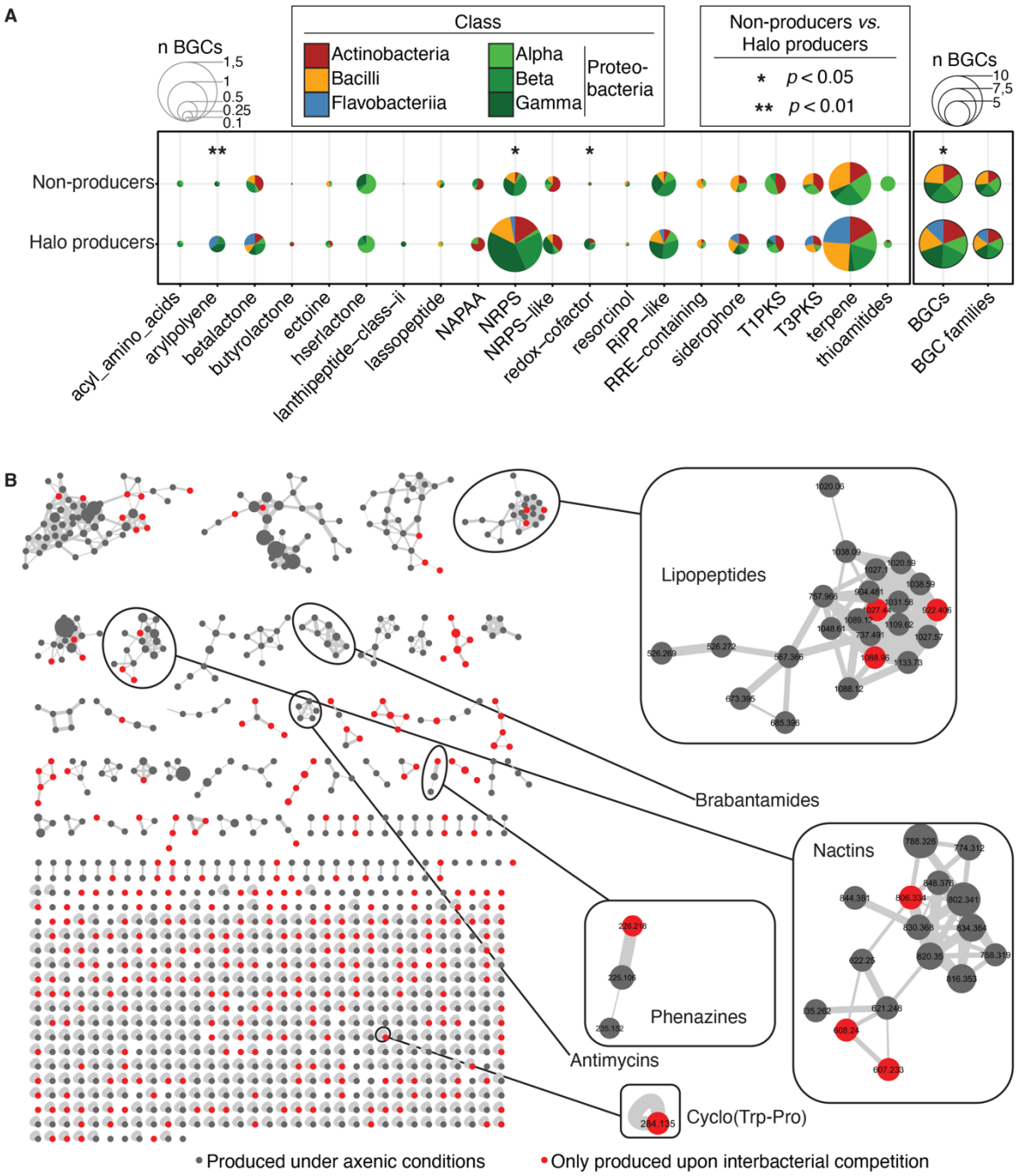

Figure 2 Genomic capacity for specialised metabolite production explains inhibitory activity. (A) Balloon plot depicting the genetic potential for specialized metabolite production. Using antiSMASH 6.0, we predicted BGCs for the genomes of all analysed bacteria. On the x-axis the 20 most abundant BGC families across all tested bacterial taxa are depicted. Size of pie charts depicts the number of a given BGC averaged across all halo producers or non-producer strains ('n BGCs'; **Fig. 1C** and **Table S1**). Sections of pie charts represent the distribution of BGCs across the bacterial classes. Sections are coloured by bacterial classes. The total number of BGCs and BGC families is depicted with black outlines. The full data set can be found in **Table S2**. Statistical significance was determined by Kruskal-Wallis followed by Dunn's post-hoc test and Benjamini-Hochberg adjustment. Significance between halo producer and non-producers is indicated by black asterisks (∗, ∗∗, indicate $p < 0.05$, and 0.01, respectively). **(B)** Molecular network of extracts from 10 producer strains with broad antagonistic activity, including extracts from inhibition halos with sensitive strains. Nodes found to be produced by sensitive strains were removed. 298 nodes (29.5% of the network) are exclusively produced in the interaction zones and highlighted in red.

I.4.3 2,4-diacetylphloroglucinol (DAPG) contributes to the inhibitory activity of *Pseudomonas brassicacearum* R401

Among all tested isolates, *Pseudomonas brassicacearum* R401 showed the greatest number of inhibitory interactions (>17x greater than average) and the largest average halo size (>10x greater than average; **Fig. 3A**). Except for Bacilli and Flavobacteria, 50 isolates belonging to all other tested bacterial classes were sensitive to the inhibitory activity of R401, particularly Actinobacteria (**Fig. 3B**), indicating the production of exometabolites with a broad spectrum of inhibitory activity. The antiSMASH-based analysis of a re-sequenced, circular R401 genome identified 16 predicted BGCs (**Fig. S3**; **Table S2**). One of these BGCs exactly matches the *phl*-operon of *Pseudomonas protegens Pf-5*, which has been shown to encode the enzymatic machinery for the production of the *Pseudomonas*-specific polyketide 2,4-diacetylphloroglucinol (DAPG; **Fig. 3C;** Keel *et al.*, 1996). Since no other genome of our culture collection isolates harbours the *phl* operon (see **Fig. S3**), this points to DAPG as a candidate molecule causing the pronounced inhibitory activity of R401. We generated a marker-free deletion mutant of the key biosynthetic gene *phlD* in R401 (**Fig. 3C**). UPLC-MS/MS-based analysis of culture supernatants validated the production of DAPG in wild-type R401 and its absence in the Δ*phld* mutant (**Fig. 3D**). In mBA experiments, the R401 Δ*phld* mutant was significantly – yet only partly – impaired in its antagonistic activity (**Fig. 3E**), retaining 71% of its inhibitory activity towards *Rs*. This result suggests that DAPG alone is insufficient to explain the full inhibitory activity of R401 towards *Rs.*

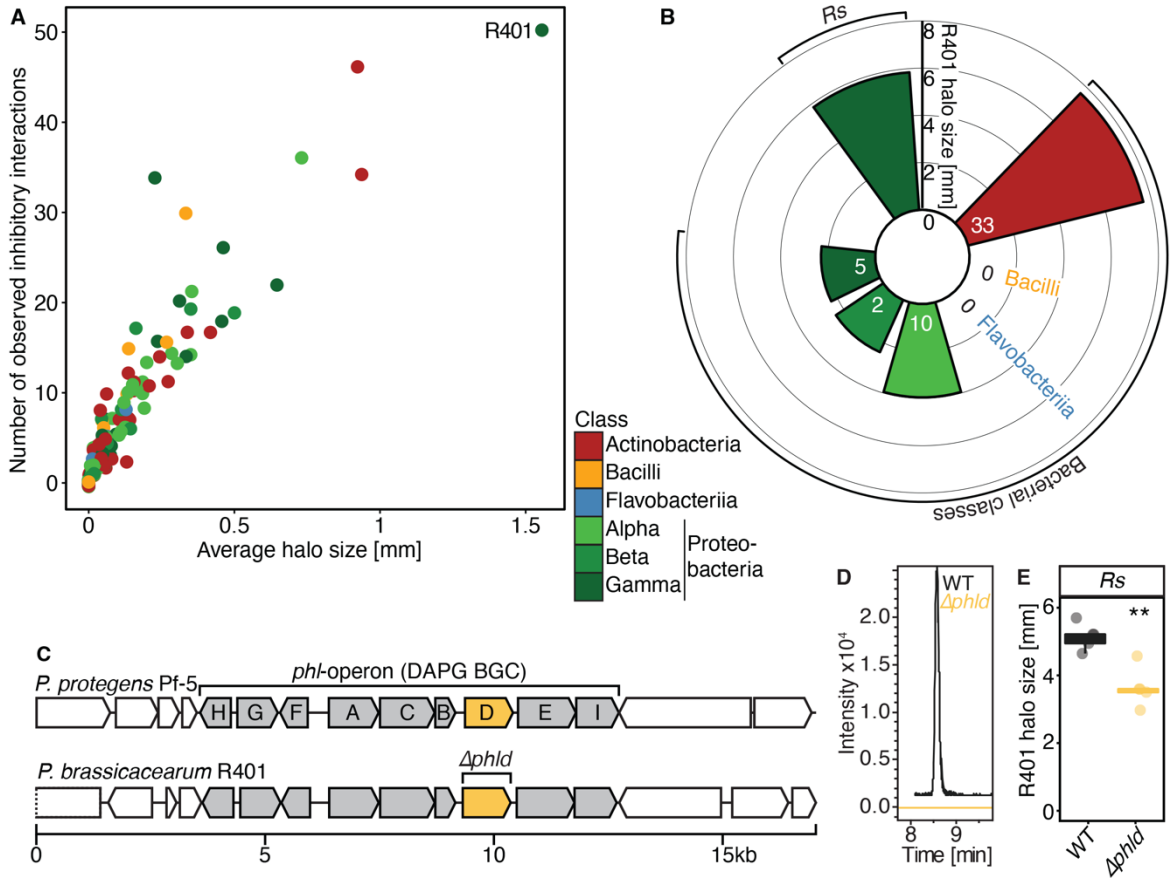

Figure 3 2,4-diacetylphloroglucinol (DAPG) contributes to the inhibitory activity of *Pseudomonas brassicacearum* R401. (A) Projection of the number of observed inhibitory activities (out of 198) as a function of the mean halo size for each producer strain as measured in mBA experiments. The most antagonistic strain (*Pseudomonas brassicacearum* R401) is highlighted. **(B)** Mean halo size of R401 against target bacterial classes or *R. solanacearum* (*Rs*) are indicated by bar height. Numbers indicate the number of observed inhibitory interactions of R401 per target bacterial class as measured in mBA. **(C)** Schematic overview of the *phl*-operon that encodes all 2,4-diacetylphloroglucinol (DAPG) biosynthetic genes in *Pseudomonas protegens Pf-5* and R401. Genes within the BGC are coloured in grey, the gene encoding the initial anabolic enzyme phlD is highlighted in yellow. **(D)** Extracted ion chromatograms for R401 DAPG (EICs: 211.0601 m/z ± 0.01 $[M+H]^+$) of the WT and mutant extracts, confirming complete lack of DAPG production in the tested mutant. **(E)** Halo production of R401 WT and Δ*phld* using *Rs* as target bacterium as measured in mBA. Statistical significance was determined by Kruskal-Wallis followed by Dunn's post-hoc test and Benjamini-Hochberg adjustment. Significance compared to WT is indicated by black asterisks (** indicate $p < 0.01$; n=5).

I.4.4 DAPG and pyoverdine act additively to inhibit taxonomically distinct root microbiota members

We performed a forward genetic screen to reveal additional determinants mediating the residual inhibitory activity of R401 Δ*phld*. First, we generated a R401 mini-*Tn5* transposon library with >6,000 insertion mutants. We adopted a fluorescence-based bacterial co-culture system in

liquid medium to test all R401 insertion mutants individually for their ability to suppress growth of a GFP-expressing *Rs* GMI1000 strain (*Rs* GMI1600; Aldon *et al.*, 2000). Of the 230 candidates identified in the primary screen, 38 R401 *Tn5* mutants were robustly impaired in *Rs* suppression after two independent rounds of validation (**Fig. 4A** and **B; Table S3**). One of these candidate R401 mutants was also significantly impaired (on average 26.6%) in its inhibitory activity against *Rs* in mBA experiments on solid agar, suggesting that this mutant is impaired in the production of an inhibitory exometabolite (**Table S3**). This R401 mutant carries a *Tn5* transposon insertion within the gene of a putative acyltransferase (*pvdY*) involved in the biosynthesis of the siderophore pyoverdine in *Pseudomonas aeruginosa* (Lamont *et al.*, 2006). We validated the contribution of R401 *pvdY* to pyoverdine biosynthesis and *Rs* inhibition by generating an independent *pvdY* deletion mutant, Δ*pvdy*, and a R401 deletion mutant of the gene encoding NRP synthetase *pvdL,* located downstream of *pvdY* (Δ*pvdl*, **Fig. 4C**). In mBA experiments with *Rs* GMI1000, the R401 Δ*pvdy* strain phenocopied the R401 *tn5::pvdy* mutant and the mutant phenotype was complemented by expression of *pvdY* under its native promoter in the R401 Δ*pvdy* background *(*Δ*pvdy::pvdY*). R401 Δ*pvdl* exhibited a slightly weaker impairment of halo production compared to R401 Δ*pvdy*, suggesting that *pvdY* may be involved in the biosynthesis of an additional exometabolite. We also generated a R401 double deletion strain, Δ*pvdy* Δ*pvdl*, which is impaired in its inhibitory activity against pathogenic *Rs* to a similar extent as the R401 Δ*pvdy* single mutant (**Fig. 4D**). Using mass spectrometry, we confirmed that all generated R401 pyoverdine mutants had lost their ability to produce pyoverdine (measured as dihydropyoverdine with the sequence: Glu-Q-Lys-AcOHOrn-Ala-Gly-Ser-Ser-OHAsp-Thr, with Q being the fluorophore dihydroxyquinoline; **Fig. 4E**). This is consistent with the assumption that both *pvdY* and *pvdL* in R401 are needed for pyoverdine biosynthesis.

All tested *Pseudomonas* isolates in *At*-RSphere contain pyoverdine biosynthetic genes; however, for R9 no characteristic pyoverdine fluorescence was detected (**Fig. S3**), potentially explaining its low inhibitory activity in mBAs (**Fig. 1C**). Therefore, we hypothesized that pyoverdines contribute more broadly to explaining the unusually high inhibitory activity of the Pseudomonadaceae detected in the mBA experiments and isolated pyoverdine mutants in another *Pseudomonas* root commensal in our collection. We generated a mini-*Tn5* mutant library of approx. 6,000 insertion mutants of pyoverdine-producing *Pseudomonas fluorescens* R569 and assayed about 2,000 mutants for loss of pyoverdine-mediated fluorescence of individual mutants grown in axenic liquid cultures by fluorimetry (**Fig. S4A**). Characterization

of the *Tn5* integration sites revealed one mutant in each of the R401 *pvdY* and *pvdL* homologues (**Table S3, Fig. S4B**). Unlike the partial loss of inhibitory activity of the R401 Δ*pvdy* and Δ*pvdl* single and Δ*pvdy* Δ*pvdl* double mutants against *Rs*, the R569 Δ*pvdy* and Δ*pvdl* single mutants both showed a complete loss of inhibitory activity to *Rs* in mBA experiments (**Fig. S4D**). Although the genomes of root commensals R401 and R569 are assigned to different *Pseudomonas* sublineages (**Fig. 1B**) and the arrangement of genes in the *pvd*-operon is different (**Fig. 4C** and **Fig. S4C**), it is likely that the corresponding pyoverdines are directly responsible for the observed inhibitory activity. Our findings indicate that pyoverdine might either be the sole or one of several exometabolites produced by root commensals that limit the growth of *Rs*. Since pyoverdines function as iron-chelators, we tested whether their inhibitory activity can be explained by interbacterial competition for iron by supplementing mBA agar medium with excess ferric iron (100 µM $FeCl_3$), which resulted in significantly impaired inhibitory activity to *Rs* when confronted with wild-type R401 or undetectable *Rs* growth inhibition when confronted with wild-type R569, thus phenocopying results obtained with the corresponding strain-specific pyoverdine mutants (**Fig. 4D** and **Fig. S4D**). Given that the isolated pyoverdine mutants of both *Pseudomonas* isolates also exhibit drastically reduced iron mobilisation capacity compared with the corresponding wild-type isolates (**Fig. 4F** and **Fig. S4E**), we conclude that their inhibitory activities against root commensals and pathogenic *Rs* are likely mediated through their iron chelator function. However, we cannot exclude a possible additional pyoverdine activity under limited iron conditions.

To test whether these two classes of compounds are sufficient to account for the full inhibitory activity of R401, we generated two R401 double pyoverdine and DAPG mutants, Δ*pvdy* Δ*phld* and Δ*pvdl* Δ*phld*, and conducted mBA assays using *Rs* and a representative set of the aforementioned commensals previously shown to be sensitive to R401 in our pairwise interaction screen as target isolates (**Table S1**). Remarkably, the double pyoverdine and DAPG mutants showed severely reduced inhibitory activity against *Rs,* and all other tested isolates compared to the single mutants, suggesting a cumulative impact of the two metabolites. Although the general sensitivity patterns were again isolate-specific, Actinobacteria were typically inhibited by DAPG alone. DAPG and pyoverdine collectively explained >70% of R401 inhibitory activity, but a residual halo of inhibition was still observed, pointing to at least a third – yet to be defined – exometabolite (**Fig. 4G**). The results collectively confirm that DAPG and pyoverdine likely have broad relevance for shaping the root microbiota.

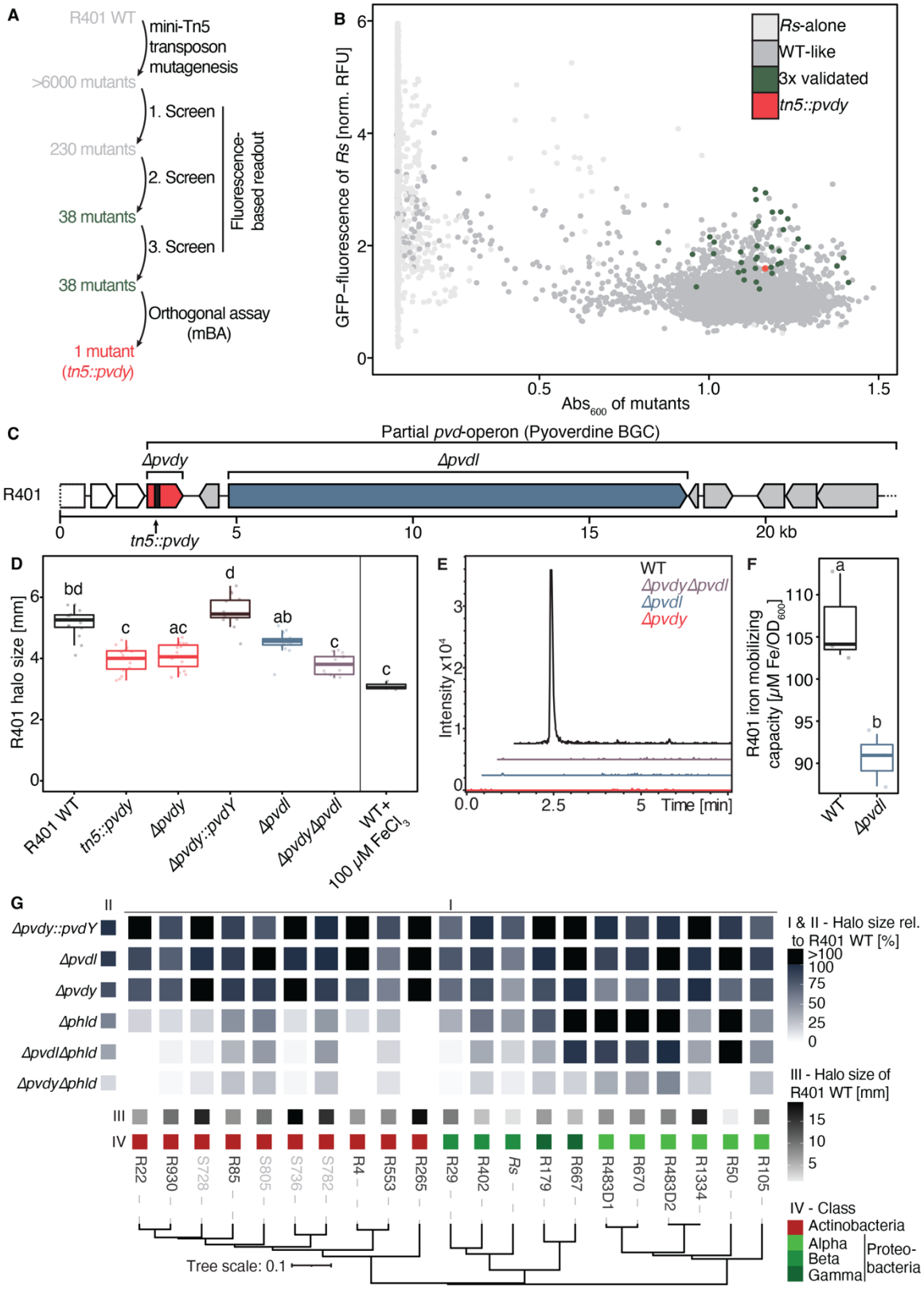

Figure 4 DAPG and pyoverdine act additively to inhibit taxonomically distinct root microbiota members. (A) Schematic overview of the mini-Tn5 transposon mutant screen workflow in R401. **(B)** Effect of >6000 R401 transposon mutants on the growth of GFP-expressing *R. solanacearum* (*Rs* GMI1600) as a function of the absorption at 600 nm of axenically grown mutants. *Rs*-alone indicates reaction vessels without R401 mutants. All other points correspond to individual R401 mutants that have been coloured based on their

phenotype in this screen. **(C)** Schematic overview of the genomic context of the fragmented *pvd*-operon which encodes a fraction of pyoverdine biosynthetic genes of R401. Genes within the BGC are coloured in grey, *pvdY* and *pvdL* are highlighted in red and blue, respectively. Transposon integration sites are highlighted by vertical black bars. **(D)** Halo production of R401 WT and four different mutants that are impaired in the production of pyoverdine (*tn5::pvdy, Δpvdy, Δpvdl, ΔpvdyΔpvdl)* as measured in mBA. Mutant names and colours are depicted as in panel **(C)**. Δ*pvdy::pvdY* is a complementation line of Δ*pvdy*. Halo production of R401 WT strains after medium supplementation with 100 µM $FeCl_3$. *Rs* was used as a target strain. Halo size measurements were taken after 3 days of interaction. Letters indicate statistically significant differences as determined by Kruskal-Wallis followed by Dunn's post-hoc test and Benjamini-Hochberg adjustment with $p < 0.05$ (n=15). **(E)** Extracted ion chromatograms for the R401 Dihydropyoverdine (EICs: 622.2764 m/z ± 0.1 $[M+2H]^{2+}$) of the WT and mutant extracts, confirming complete lack of production in all tested mutants. **(F)** Ferric iron mobilizing activity of R401 WT and Δ*pvdl*. Letters indicate statistically significant differences as determined by Kruskal-Wallis followed by Dunn's post-hoc test and Benjamini-Hochberg adjustment with $p < 0.05$ (n=3). **(G)** Heatmap depicting a halo of mBA screen of R401 WT and single and double mutants that are impaired in DAPG (Δ*phld*) and/or pyoverdine (Δ*pvdl* or Δ*pvdy*) production. Δ*pvdy::pvdY* is a Δ*pvdy* complementation line. A taxonomically diverse set of root- and soil-derived bacteria (comprising *Rs*) has been used as target bacteria. All target bacteria are sensitive to R401 (**Table S1**). Halo sizes have been normalized to the respective WT-halo sizes. Average, relative halo sizes are depicted in **(I)**. **(II)** shows the average thereof across all tested strains, while **(III)** shows the average absolute halo size of R401 WT on a given target strain; n=5. **(IV)** is a phylogenetic tree based on v5v7 16S rRNA genes, depicting strain taxonomy at the class level.

I.4.5 DAPG and pyoverdine modulate root microbiota assembly and restrict bacterial diversity

We conducted root microbiota reconstitution experiments with germ-free *A. thaliana* Col-0 in Flowpots to study the contribution of DAPG and pyoverdine to root microbiota structure and to limit the growth of *Rs* (Kremer *et al.*, 2021). We tested the influence of heat-killed or live wild-type R401, R401 Δ*pvdy* and Δ*pvdl* single as well as Δ*pvdy* Δ*phld* and Δ*pvdl* Δ*phld* double mutants on a phylogenetically diverse community (also referred to as a synthetic community; SynCom) that comprises 18 bacterial isolates (**Fig. S5A**; **Table S1**), in both 'soil' (peat matrix) and root compartments. After three weeks of plant-microbe co-cultivation, DNA was extracted from all soil and root samples and was subjected to *16S rRNA* amplicon sequencing at isolate-specific resolution. Shoot fresh weight did not differ between conditions, and no wilting was observed (**Fig. S5 B** and **C**), indicating that *Rs* was unable to cause disease on *A. thaliana*, possibly due to the presence of the SynCom. This is consistent with very low *Rs* relative abundances found in root samples (**Fig. S5D**) and a previous report that direct immersion of *A. thaliana* roots with a very high *Rs* inoculum of 10^8 cells/ml was needed to induce wilting symptoms in the crucifer (Deslandes *et al.*, 2007).

The addition of live, wild-type R401 to the SynCom significantly reduced bacterial alpha-diversity (Shannon index) compared to the heat-killed (HK) R401 condition in the root compartment ($p < 0.001$). This major impact on the community is gradually lost when R401 exometabolite mutants were co-inoculated with the SynCom (**Fig. 5A**). Importantly, no such effects were observed in the soil compartment (**Fig. 5B**). Bacterial beta-diversity (Bray-Curtis dissimilarity) was also drastically affected by wild-type R401 inoculation, explaining most of the variation and resulting in a clear separation along axis 1 (HK *versus* WT, $p < 0.001$; $R2 = 0.63$). All mutant samples fall in between these extremes and follow a clear trajectory, WT > single mutants > double mutants > HK, suggesting that DAPG and pyoverdine have a cumulative influence on bacterial community structure in the root compartment (**Fig. 5D**). This is likely due to direct exometabolite activities, as the production of either metabolite did not affect plant phenotypes (**Fig. S5C**). Furthermore, *in silico* depletion of R401 *16S rRNA* sequence reads leads to similar changes in beta-diversity with even higher significance levels in some cases *(*Δ*pvdl versus* WT; $p = 0.002$; $R2 = 0.14$; **Fig. S5E**), indicating that, irrespective of R401 abundance, the bacterial community is altered by DAPG and pyoverdine production. While in the soil compartment, inoculation of wild-type R401 leads to a similar shift as in the root compartment (HK *versus* WT, $p < 0.001$; $R2 = 0.66$), genetic depletion of either DAPG or pyoverdine biosynthetic abilities alone or both together does not alter community structure (**Fig. 5E**), which indicates niche-specific production of these exometabolites in the root compartment. *In silico* depletion of R401 *16S rRNA* sequence reads still results in significant effects of R401 on community structure (HK *versus* WT, $p < 0.001$; $R2 = 0.35$; **Fig. S5F**), indicating that R401 uses other, unknown mechanisms to influence community structure in soil.

To determine if the mBA results obtained *in vitro* have physiological relevance *in planta*, we inspected relative isolate abundances across conditions, reasoning that isolates insensitive to at least one of the R401 exometabolites *in vitro* would not benefit from genetic disruption of either BGC in a community context in the root compartment. This analysis revealed that only DAPG- and/or pyoverdine-sensitive isolates benefited from disruption of the corresponding BGCs present in R401 (**Fig. 5G**), suggesting that binary interaction data *in vitro* can predict the impact on individual commensal isolates in a community context in the root compartment. This observation prompted us to test whether mBA data could predict community-scale effects as well as effects on single isolates. We computed the average reduction in inhibitory activity for each R401 mutant (see **Fig. 4G**) and tested whether the lack of competitiveness could predict changes in alpha- and beta-diversity *in planta*. Linear regression analyses revealed that binary

interaction data largely explained the observed effect size in the root compartment for both alpha- and beta-diversity indices but had no predictive power in the soil compartment (**Fig. 5C** and **F**, respectively). In conclusion, two exometabolites produced by a single isolate have large effects on key ecological indices of a root-associated SynCom and can be predicted based on pairwise *in vitro* interaction experiments.

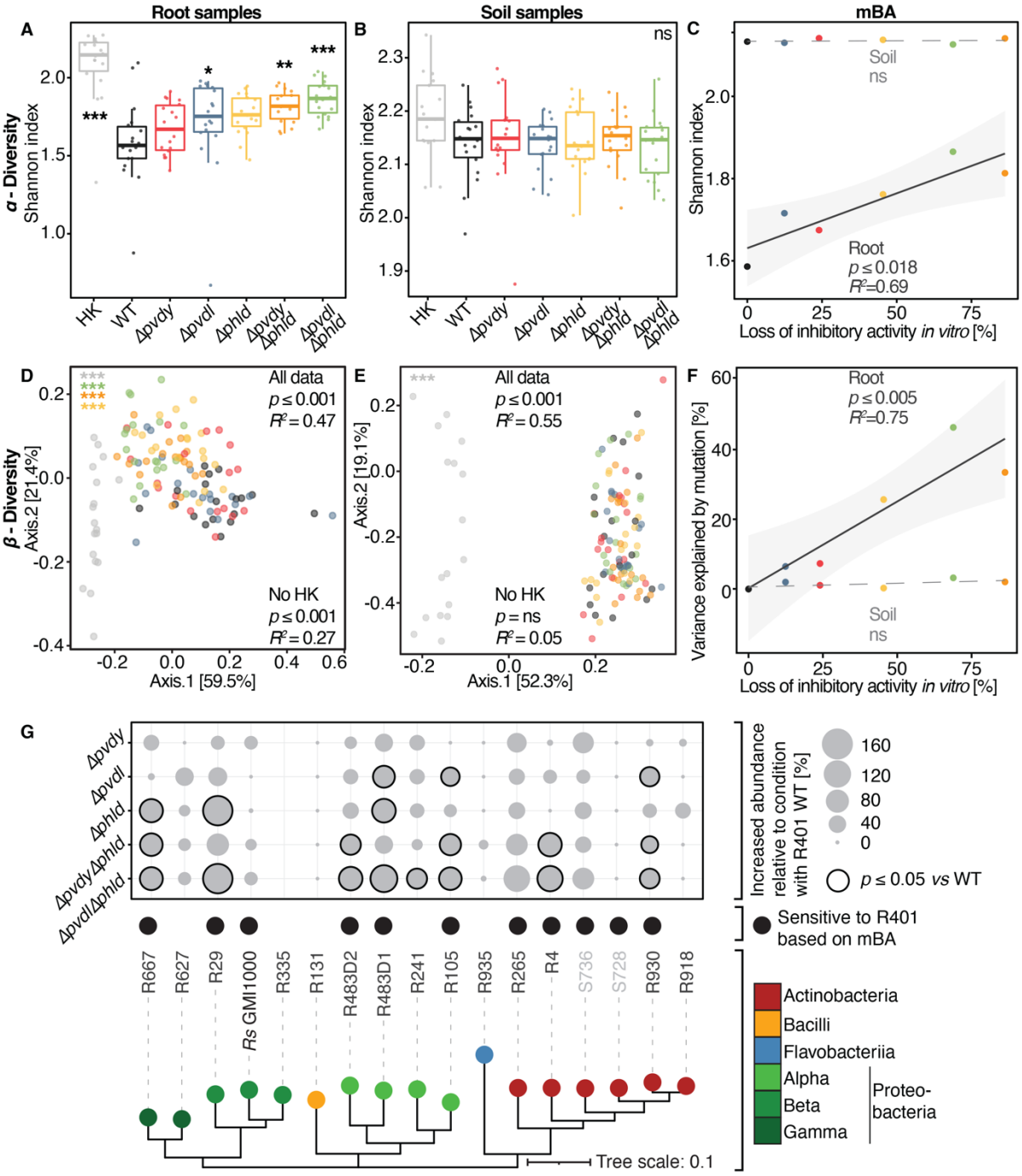

Figure 5 DAPG and pyoverdine modulate root microbiota assembly and restrict bacterial diversity. (A–G) Community profiling of an 18-member bacterial SynCom comprising either heat-killed R401 (HK, wild-type (WT) background), live R401 WT, or corresponding mutants that are impaired in the production of DAPG (*Δphld*), pyoverdine (*Δpvdγ, Δpvdl*) or both (*Δpvdγ Δphld, Δpvdl Δphld*). SynComs and *A. thaliana* Col-0 seeds were co-inoculated into the peat-based gnotobiotic Flowpot system. At 21 dpi roots and soil

samples were taken. Data from three full-factorial experiments with 6 biological replicates each. **(A, B)** Alpha diversity (Shannon index) of root **(A)** and soil **(B)** samples in response to R401 or its mutants. Statistical significance was determined by Kruskal-Wallis followed by Dunn's post-hoc test and Benjamini-Hochberg adjustment. Significance compared to WT is indicated by black asterisks (∗∗, ∗∗∗, indicate $p < 0.01$, and 0.001, respectively; 'ns': not significant; n=18). **(D, E)** unconstrained PCoA based on Bray-Curtis community dissimilarities between samples in root **(D)** and soil **(E)** in response to R401 or its mutants. PERMANOVA-derived *p*-values are represented as asterisks (∗∗∗, indicate $p < 0.001$; n=18), coloured by the respective condition. PERMANOVA analysis on the full data set before (All data) or after (No HK) *in silico* depletion of HK samples are indicated in black; R^2 represents the variance explained by R401 genotype. **(C, F)** Regression analysis of loss of inhibitory activity of R401 mutants in a mBA (**Fig. 4G**) and Shannon indices (**C**; data from **A** and **B**) or variance explained by R401 (**F**; data from **D** and **E**). *p*-values and R^2 derive from a linear model and have been computed for soil and root samples separately; ns, not significant. Confidence intervals are depicted in light grey. **(G)** Balloon plot depicting the increase in relative abundance of SynCom members at the root relative to the condition in which R401 WT has been inoculated. Statistical significance was determined by Kruskal-Wallis followed by Dunn's post-hoc test and Benjamini-Hochberg adjustment. Significance compared to WT in non-normalized dataset is indicated by black circles, indicating $p < 0.05$ (n=18). Susceptibility towards R401 wild type in the halo assay is depicted as black spheres. Black spheres indicate sensitivity towards R401 while coloured spheres represent the respective bacterial class.

I.4.6 DAPG and pyoverdine act as root competence determinants in a community context

To examine whether R401-induced modulation of bacterial assembly and diversity (*i.e.*, through co-production of DAPG and pyoverdine) promoted R401 competitiveness, we determined the relative abundance of R401 in SynCom samples collected from root and soil compartments. In both root and soil samples, the *16S rRNA* sequence reads of live R401 by far exceeded the barely detectable HK R401 reads, indicating that live R401 inoculum proliferates in both compartments under all conditions (**Fig. 6A** and **B**). However, R401 accumulated in association with roots at >2-fold higher abundance than in the soil compartment. R401 accumulation in the root compartment was gradually reduced in the SynCom context: Single or double mutations of DAPG and pyoverdine biosynthetic genes were sufficient to reduce the R401 abundance up to approx. 39% compared to wild-type R401 (**Fig. 6A**). Importantly, the capacity of these deletion mutants to colonise the soil compartment remained unaffected (**Fig. 6B**). We also investigated the root colonisation capacity of wild-type and all five R401 deletion strains in mono-associations on axenic *A. thaliana* plants in an agar-based system (Ma *et al.*, 2021) and found no significant differences in R401 root load as quantified by live R401 cell counts (colony forming units, CFUs; **Fig. 6C**). Neither the growth of R401 DAPG or pyoverdine mutants was impaired in axenic culture media (**Fig. S6B** and **C**). Similarly, colonization experiments with wild-type R401 or the Δ*pvdy* Δ*phld* double mutant in the Flowpot system revealed no difference in root colonization capacity in the absence of bacterial competitors (**Fig. S6A**). Thus, DAPG and pyoverdine co-function as R401 root competence

determinants specifically in competition with other members of this SynCom in the root compartment.

Cross-referencing of several commensal culture collections of isolates from roots or leaves of *A. thaliana* or roots of the legume *Lotus japonicus*, isolated from plants grown in the same or different natural soils on different continents (Bai *et al.*, 2015; Karasov *et al.*, 2018; Levy *et al.*, 2017; Wippel *et al.*, 2021), revealed an increased abundance of DAPG and pyoverdine BGCs in root-derived *Pseudomonas* isolates (**Fig. S6D** and **E**). These results not only support our conclusions obtained with a defined core commensal community and gnotobiotic *A. thaliana*, but also indicate a broader yet root-specific role of these two exometabolites in natural environments beyond the model crucifer.

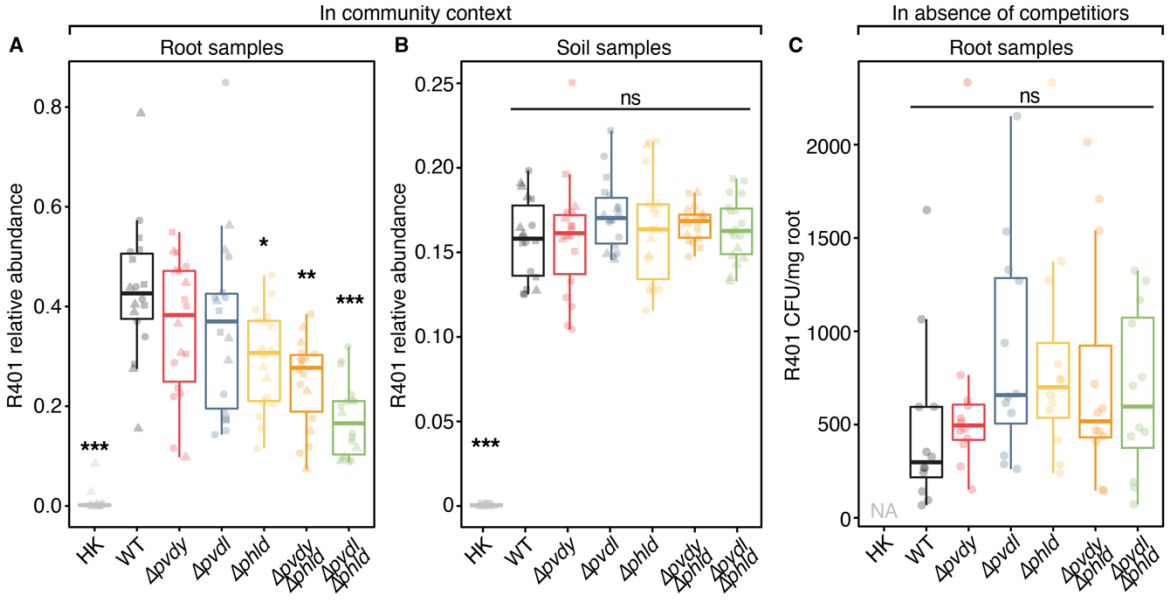

Figure 6 DAPG and pyoverdine act as root competence determinants in a community context. **(A, B)** Relative abundance of R401 WT or mutants in root **(A)** and soil **(B)** samples in competition with 18-member SynCom, as in **Fig. 5**; n=18. Statistical significance was determined by Kruskal-Wallis followed by Dunn's post-hoc test and Benjamini-Hochberg adjustment. Significance compared to WT is indicated by black asterisks (∗, ∗∗, ∗∗∗, indicate $p < 0.05$, 0.01, and 0.001, respectively; ns, not significant). **(C)** Colonization capability of R401 or its mutants in mono-associations on axenically grown *A. thaliana* Col-0 roots. Plants were grown on ½ MS-agar plates for 14 days. Colony forming units have been determined and normalized to root fresh weight; n=12. Statistical significance was determined by ANOVA followed by Tukey's HSD test. No significant differences were detected as indicated by 'ns'.

I.5 Discussion

Many specialised metabolite BGCs of microbes are expressed poorly or not at all under laboratory growth conditions, due to tight control of their expression in response to environmental or host-derived signals (Brakhage, 2013; Ogran *et al.*, 2019; Rutledge & Challis, 2015). Nevertheless, our *in vitro* results with wild-type R401 and its exometabolite mutants can predict the changes in alpha- and beta-diversity indices of an 18-member SynCom *in planta* (**Fig. 5C** and **F**). Together with the identification of a subset of specialised metabolites, primarily polyketides and non-ribosomal peptides, that are specifically produced upon competition sensing, these results suggest that interbacterial competition can activate cryptic BGCs in the *A. thaliana* root microbiota. A related study using an *A. thaliana* phyllosphere bacterial culture collection also demonstrated widespread production of specialised metabolites and identified 725 binary inhibitory interactions *in vitro* with only 3.6% of 224 strains mediating the majority of these interactions (Helfrich *et al.*, 2018). The *A. thaliana* leaf and root microbiota overlap extensively at higher taxonomic ranks and *Pseudomonas* species are core members of both communities (Bai *et al.*, 2015). However, the comparison between root- and leaf-derived *Pseudomonas* genomes collected from natural environments reveals complete or partial niche specificity, respectively, for the capacity of *Pseudomonas* to produce DAPG and pyoverdine in the root compartment (**Fig. S6D**). Furthermore, the total number of BGCs is significantly higher (approx. 1.6x) in root-derived *Pseudomonas* isolates (**Fig. S6E**). Likewise, the number of antagonistic interbacterial interactions within the root microbiota significantly exceeds those between abundant soil-derived bacteria (**Fig. 1D**). These findings could be explained by the fact that natural, unplanted soils and leaves represent oligotrophic habitats (Eilers *et al.*, 2010b; Vorholt, 2012), whereas the rhizoplane is a microenvironment with a continuous supply of root exudation-derived non-structural carbohydrates to support bacterial proliferation (Haichar *et al.*, 2016). It is likely that the large number of antagonistic interactions we found between root microbiota members *in vitro* is also influenced by the agar medium, which is rich in non-structural organic carbon to mimic the nutrient-rich rhizoplane and thereby induces the costly biosynthesis of exometabolites.

We have provided genetic evidence for a root niche-specific co-function of the exometabolites DAPG and pyoverdine as root competence determinants of commensal R401 that scale at the community level by influencing alpha- and beta-diversity indices. R401 also proliferates in the soil compartment, but its growth there and its influence on the structure of the bacterial soil community are independent of these exometabolites (**Fig. 5**; **Fig. 6A** and **B**). These

observations, together with the fact that plant roots are a major sink for the uptake of rhizospheric mineral iron (Harbort *et al.*, 2020; Kobayashi & Nishizawa, 2012; Loper & Lindow, 1994), imply that the public good iron becomes rate-limiting in the root compartment. This could explain why the high-affinity iron chelator pyoverdine and antimicrobial DAPG co-function and maximize R401 growth at the expense of its commensal competitors in the root niche, despite their different modes of action. Consistent with this model, the expression of core biosynthetic genes involved in the production of both DAPG and pyoverdine are induced under iron-limiting conditions in rhizospheric *P. fluorescens* and human pathogenic *P. aeruginosa* PAO1 (Lim *et al.*, 2012; Palma *et al.*, 2003). The indistinguishable root colonization capacity of wild-type R401, pyoverdine or DAPG single, or double mutants in mono-associations with *A. thaliana* is also consistent with our model and further supports the specific role of these exometabolites in inter-species competition during root microbiota establishment. Likewise, *Pseudomonas fluorescens* C7R12 pyoverdine mutants were unaffected in rhizosphere competence under axenic conditions (Mirleau *et al.*, 2000). All seven *A. thaliana* root-derived *Pseudomonas spp.* strains in the *At*-RSphere culture collection have the genetic capacity to produce pyoverdines (**Fig. S3**). Together with the essential function of pyoverdines produced by multiple *Pseudomonas* root commensals in limiting growth of pathogenic *Rs* (**Fig. 4D**; **Fig. S4D**; Gu, Wei, *et al.*, 2020), this suggests a widespread role for these siderophores in determining *Pseudomonas* competitiveness in the root microbiota, even in soils that contain replete bioavailable inorganic iron for plant growth (Bai *et al.*, 2015; Gu, Wei, *et al.*, 2020; Gu, Yang, *et al.*, 2020; Harbort *et al.*, 2020). Thus, it is possible that in natural soils, regulated secretion of pyoverdines is an adaptive trait of the genus *Pseudomonas* to simultaneously compete against the root iron sink and enable pervasiveness of the Pseudomonadaceae lineage *via* interbacterial competition (Bulgarelli *et al.*, 2012; Hacquard *et al.*, 2015; Lundberg *et al.*, 2012). Two of the seven leaf-derived *Pseudomonas* strains present in the *At*-LSphere culture collection do not have a predicted capacity for pyoverdine biosynthesis (**Table S2**). However, we found that only three strains (L15, L58 and L434) are capable of producing pyoverdine under laboratory conditions, and these strains exactly match the reported inhibitory patterns of leaf-derived *Pseudomonas* isolates in mBA experiments (Helfrich *et al.*, 2018). This suggests that during colonization of aerial plant organs from soil through migration *via* the root surface or by direct contact of leaves near the soil (Bai *et al.*, 2015; Massoni *et al.*, 2021), pyoverdine production costs likely exceed their benefit. This is supported by our observation that R401 pyoverdine mutants have growth benefits compared with wild-type R401 in a liquid medium lacking inorganic iron, which partially mimics the available iron-deprived surface of healthy

leaves (**Fig. S6C**; Loper and Lindow, 1994; Wensing *et al.*, 2010). Nevertheless, siderophores of *Pseudomonas* can play a role in competition with other pseudomonads in the absence of a eukaryotic host. Pyoverdine of the opportunistic human pathogen *P. aeruginosa* PAO1, which is commonly isolated from soil and water, promotes invasion into standing communities of environmental pseudomonads under iron-limiting conditions when the invader can use its siderophores to inhibit, rather than stimulate, resident growth (Figueiredo *et al.*, 2022).

Our genetic data show that a sequential reduction in the diversity of specialised exometabolites in one species is sufficient to increase alpha-diversity indices and significantly alter the beta-diversity of a synthetic root microbiota, thereby establishing a causal link between within-species genetic diversity and interspecies diversity changes. This suggests that in the root microenvironment, DAPG and pyoverdine produced by wild-type R401 co-function to locally inhibit the growth of multiple SynCom members, which in turn increases the abundance of the producer R401. Our results obtained with the SynCom in co-culture with gnotobiotic *A. thaliana* grown in peat matrix bear striking similarity to the changes in alpha-diversity reported for this plant when grown in natural soils, where bacterial alpha-diversity in bulk soil, rhizosphere and root compartments gradually decreases towards the root (Bulgarelli *et al.*, 2012; Lundberg *et al.*, 2012; Thiergart *et al.*, 2020). This suggests that exometabolite-mediated antagonistic interactions of commensals underpin at least part of the reduction of alpha-diversity consistently observed in natural environments at the soil-root interface.

Given the prevalence of operons predicted to encode pyoverdines among root-derived *Pseudomonas spp.* isolates in the *At*-RSphere culture collection (Bai *et al.*, 2015; **Fig. S3**), we consider the moderately complex 18-member SynCom employed here as necessary to overcome the genetic redundancy, at least for pyoverdine production and probably also for the DAPG exometabolite in the root microbiota, when *A. thaliana* plants are grown in natural soils (**Table S2**; Keel *et al.*, 1996; Tracanna *et al.*, 2021). It remains to be tested, whether the genetic depletion of individual bacterial exometabolites can cause similarly striking effect on highly complex natural microbial communities, as the assessment of microbial antagonism *in vitro* does often not translate towards field conditions (Knudsen *et al.*, 1997; Shtienberg & Elad, 2007; Whitaker & Bakker, 2019). However, DAPG- and phenazine overproducing mutants of *Pseudomonas putida* WCS358r have been demonstrated to differentially shape the root-associated fungal communities of field-grown wheat over experimental durations of up to 139 dpi compared to the WCS358r wild type strain (Bakker *et al.*, 2002; Glandorf *et al.*, 2001). This suggests that bacterial exometabolites – such as DAPG – can have long lasting effects on

the structure of complex microbial communities in natural conditions. The approach described here to remove genetic redundancy by using annotated genomes of cultured microbiota members may be more generally applicable to explore community functions of other microbial genetic determinants with SynComs in gnotobiotic plant growth systems. Taken together, our study suggests that high-throughput binary interaction experiments, combined with genome mining for BGCs of root microbiota culture collections, can be applied to identify strains with broad-spectrum antagonistic activities that are candidates for robust root colonizers. This might have relevance for future interventions in the root microbiota with rational biologicals that confer beneficial traits to the host, including indirect pathogen protection and mineral nutrition.

I.6 Material and methods

I.6.1 Material availability

All generated bacterial mutant strains have been deposited in the bacterial culture collection of the Department of Plant Microbe Interactions at the Max Planck Institute for Plant Breeding Research in Cologne, Germany, and are available upon request from Stéphane Hacquard (hacquard@mpipz.mpg.de).

I.6.2 Data and code availability

Raw sequencing data from SynCom reconstitution experiments (MiSeq *16S* rRNA reads) has been deposited in the European Nucleotide Archive ENA at Accession: PRJEB56224. The circular PacBio-sequenced genome of R401 has been submitted to NCBI (BioProject: SUB12090952). The MS data are deposited and publicly available at GNPS as a MassIVE dataset at ftp://massive.ucsd.edu/MSV000081381. BGC predictions using antiSMASH can be found in **Table S2**. All supplementary tables have been deposited at EDMOND: https://doi.org/10.17617/3.I1ABIM. All code and data files to reproduce the figures of this chapter were deposited to https://github.com/scriptsFG/Getzke-Hassani-et-al.-2023.git.

I.6.3 Biological material and culture conditions

Bacterial strains

The bacterial strains used in this study have been initially isolated from unplanted soil, *A. thaliana* roots or shoots (Bai *et al.*, 2015) and are summarized in **Table S1**. *Ralstonia solanacearum* GMI1000 and GMI1600 have also been reported previously (Boucher *et al.*, 1985 and Aldon *et al.*, 2000, respectively). All mutants that were generated in the R401 or R569 backgrounds in this study have been deposited at the Max Planck Institute for Plant Breeding Research and are listed in **Table S3**.

Plant growth conditions

Arabidopsis thaliana Col-0 wild-type (N60000) was obtained from the Nottingham Arabidopsis Stock Centre (NASC). *A. thaliana* seeds were sterilized using 70% ethanol and bleach. Seeds were submerged in 70% ethanol and left shaking at 40 rpm for 14 minutes.

Ethanol was removed before the seeds were submerged in 8.3% sodium hypochlorite (Roth) containing 1 µl of Tween 20 (Sigma-Aldrich) and left shaking at 40 rpm for 4 minutes. Under sterile conditions, the seeds were washed 7x times and finally taken up with sterile 10 mM $MgC1_2$. Seeds were left for stratification at 4 °C for 3 days. Seed sterility was confirmed by plating approx. 100 seeds on a 50% TSA plate.

Flowpot

Flowpots were assembled and inoculated as described below. Each Flowpot was first flushed with 50 ml sterile Milli-Q water and then 50 ml half strength Murashige and Skoog medium with vitamins (½ MS; 2.2 g/l, Duchefa Biochemie, 0.5 g/l MES, pH 5.7) containing the bacterial inoculum. Per Flowpot, five surface-sterilized and stratified *A. thaliana* Col-0 seeds were pipetted. Microboxes were then incubated in a light cabinet under short day conditions (10 h light at 21 °C, 14 h dark at 19 °C) for 14 days and randomized every 2–3 days.

Agar-media

Surface-sterilized and stratified *A. thaliana* Col-0 seeds were sown on plates containing 1% agar (Bacto Agar, Difco) in ½ MS medium supplemented with 0.5% sucrose and placed vertically in a climate chamber (Panasonic, MLR-352) and grown for six days (10 h light, 21 °C; 14 h dark, 19 °C). Using a forceps, uniform seedlings were then transferred to freshly prepared ½ MS plates without sucrose.

Bacterial culture conditions

Bacteria were streaked from glycerol stocks (25% glycerol) on TSA plates (15 g/l Tryptic Soy Broth, Sigma Aldrich; with 10g/l Bacto Agar, Duchefa Biochemie) and grown at 25 °C. Single colonies were inoculated into liquid 50% TSB (15 g/l Tryptic Soy broth, Sigma Aldrich) and grown until dense at 25 °C with 180 rpm agitation. Dense cultures were then stored at 4 °C and diluted 1 to 10 in TSB the day before the experiment and cultured at 25 °C with 180 rpm agitation overnight to ensure sufficient cell densities for slow- and rapidly growing bacteria. Glycerol stocks were stored at -80 °C and kept on dry ice when transported.

I.6.4 Screen for antagonistic interbacterial interactions

For the initial mBA experiment (**Fig. 1**), bacterial strains were cultured for seven days in 25% TSB (7.5 g/l Tryptic Soy Broth, Sigma-Aldrich). Briefly, 100 µl of a bacterial solution were re-suspended in 50 ml cooled (~38 ºC), but still molten, 25% TSA (15 g/l Bacto-Agar, Duchefa Biochemie) and poured into a square petri dish (120x120 mm). After medium solidification, 24 bacterial isolates were spotted on top of the medium using a multi-stamp replicator. The replicator was sterilized by dipping in 70% EtOH (v/v) followed by flaming and cooling. The screen comprising 39,006 binary interactions was conducted once and validated by randomly re-screening 7,470 interaction pairs as described above. All bacterial strains that showed antagonistic activity were re-screened two more times. For the *Ralstonia* inhibition screen, *R. solanacearum* GMI1000 was pre-cultured for two days in CPG medium (1% peptone, 0.5% glucose and 0.1% casamino acids; pH7.0). Before spotting the bacterial cultures, each CPG agar plate (1% Peptone, 0.5% D-glucose, 0.1% casamino acids and 1.5% agar; pH 7.0) was overlaid with 5 ml of *R. solanacearum* suspension (50 µl of pre-cultured *R. solanacearum* in pure sterile water). Excess *R. solanacearum* suspension was removed and the plates were briefly dried, then 5 µl of the bacterial culture were spotted onto the *R. solanacearum*-overlaid plates. All isolates were tested three times. For all subsequent halo assays, strains were cultivated in 50% TSB until turbidity, stored at 4 °C and diluted 1:10 in 50% TSB one day before the experiment. Bacterial cultures were pelleted at 4,000 rpm for 15 min. The resulting bacterial pellets were subsequently washed 3 times and resuspended in 1 ml 10 mM $MgCl_2$. OD_{600} were measured and set depending on the strain. One hundred microliters bacterial culture were inoculated per 50 ml 25% TSA. After drying, up to nine different 3 µl droplets of bacterial suspensions with 0.4 OD_{600} were applied with equal distances. For all experiments, plates were incubated at 25 °C for up to 96 hours and photographs were taken thereafter for quantitative image analysis. The size of the halo of inhibition was measured using ImageJ with up to five separate measurements, which were subsequently averaged to reduce variation. Raw data of **Fig. 1** are indicated in **Table 2**.

I.6.5 Metabolomic analyses

Metabolites were extracted from individual isolates (n = 198) grown on the same agar medium used in mBA experiments with two organic solvents with different polarity, ethyl acetate and methanol, to capture greater small molecule diversity. Each bacterial strain was grown separately on 25% TSA plates (25% BBL™ Trypticase™ Soy, BD with 1.8% Bacto-Agar; BD,

Germany). After seven days of incubation at 25 °C, three to four agar plugs were taken from the periphery and inside of the bacterial colony. Agar plugs were crushed and washed with 500 µl water followed by extraction in 500 µl ethyl acetate and methanol. Between each extraction step, samples were vortexed for 30–45 s. After each extraction, the solvents were evaporated, and the residue was redissolved in 500 µl LC-MS-grade methanol and filtered through a 0.2-µm membrane into HPLC vials. Solvents for blanks (uninoculated medium) were extracted according to the same protocol. The extraction protocol was also used to analyse the inhibition zones upon inter-bacterial interactions. To this end, a bacterial lawn of a sensitive target strain, either R472D3, R480 or R553, was prepared as top agar and the antibiotic producer strains (R63, R68, R71, R342, R401, R562, R569, R690, R920 and R1310, respectively) were inoculated on top. The agar plugs were taken from the zone of inhibition and inside of the antibiotic-producing colony. In total, 20 interactions were analysed. All samples were analysed by HPLC-MS/MS on a micrOTOF-Q mass spectrometer (Bruker) with ESI-source coupled with a HPLC Dionex Ultimate 3000 (Thermo Scientific, Germany) using a Zorbax Eclipse Plus C18 1.8 µm column, 2.1×50 mm (Agilent). The column temperature was 45 °C. MS data were acquired over a range 100–3000 m/z in positive mode. Auto MS/MS fragmentation was achieved with rising collision energy (35–50 keV over a gradient from 500–2000 m/z) with a frequency of 4 Hz for all ions over a threshold of 100. uHPLC began with 90% H_2O containing 0.1% acetic acid. The gradient started after 0.5 min to 100% acetonitrile (0.1% acetic acid) in 4 min. Two microliters sample solution were injected to a flow of 0.8 ml/min. All MS/MS data were converted to '.mzxml' format and transferred to the GNPS server (gnps.ucsd.edu; Wang *et al.*, 2016). Molecular networking was performed based on the GNPS data analysis workflow using the spectral clustering algorithm (Aron *et al.*, 2020). The data was filtered by removing all MS/MS peaks within +/- 17 Da of the precursor m/z. MS/MS spectra were window-filtered by choosing only the top 6 peaks in the +/- 50 Da window throughout the spectrum. The data was then clustered with MS-Cluster with a parent mass tolerance of 0.02 Da and a MS/MS fragment ion tolerance of 0.02 Da to create consensus spectra. Consensus spectra that contained less than two spectra were discarded. Networks were then created from the single cultivation and from the competition experiments. Edges were filtered to have a cosine score above 0.5 (0.6 for interaction network) and more than four matched peaks. Further edges between two nodes were kept in the network only if each of the nodes appeared in each other's respective top ten most similar nodes. Sample attributes were assigned to the data files (strain, genus, family, order, class phylum extraction solvent). For the network analysis, all nodes that contained ions from the blank medium were removed. The network was visualized using Cytoscape 3.5.1.

I.6.5 Detection of R401 DAPG and pyoverdine

For the detection of iron-chelating compounds, a R401 preculture was grown over night in 5 ml LB medium at 30 °C and 200 rpm. Before inoculation of the main culture, cells were washed twice with the main culture medium to remove potential traces of iron from the medium. Erlenmeyer flasks containing 20 ml of modified MM63 (KH_2PO_4 13.61 g/L KOH 4.21 g/L, $(NH_4)SO_4$ 1.98 g/L, $MgSO_4$*7 H_2O 0.25 g/L, NaCl 0.5g/L, Glucose*H_2O 5,00 g/L, pH 7.1 KOH/HCl) with or without addition of 0.0011 g/L $FeSO_4$*7 H_2O were inoculated with 100 µl of preculture and cultivated for 6 days at 30 °C and 200 rpm. Every second day, 0.5 ml sample were taken, cells were removed by centrifugation and 5 µl of supernatant were analysed on a Bruker microTOFq-II high-resolution mass spectrometer coupled to an Agilent 1290 UPLC system with an Acquity UPLC BEH C-18 reverse phase column, run in a gradient of MeCN/H2O + 0.1% formic acid. Higher accuracy measurements were performed on a maXis-II qTOF, coupled to an identical LC setup as described earlier.

I.6.6 PacBio sequencing and assembly

PacBio-sequenced reads were obtained from Max Planck Genome Centre (https://mpgc.mpipz.mpg.de). PacBio 2kb sequence control reads were removed with blasr (Chaisson & Tesler, 2012). Reads were assembled using Flye v2.8-b1673 (Kolmogorov *et al.*, 2019) and polished four times using the internal function. Then, assembly went through a final polishing step with Medaka v1.0.3 (Oxford Nanopore Technologies Ltd, 2018). Annotation was conducted using Prokka 1.12-beta (Seemann, 2014), and output files (.ffn, .faa, .gff) were parsed with a custom Python script. Then, we examined; (I) statistics of assemblies and visualisation of assemblies with Bandage v0.8.1 (Wick *et al.*, 2015); (II) integrity of assemblies using BUSCO v4.0.6 (Seppey *et al.*, 2019) with bacteria_odb10 (https://busco-data.ezlab.org/v4/data/lineages/); and (III) potential contamination with other species with Blobtools2 v2.2 (Challis *et al.*, 2020). Phylogenetic assignment of R401 as *Pseudomonas brassicacearum* is based whole genome phylogeny.

I.6.7 BGC prediction using antiSMASH

Bacterial genomes were downloaded from "www.at-sphere.com" (Bai *et al.*, 2015) or NCBI and submitted to https://antismash.secondarymetabolites.org/ version 6.0 (Blin *et al.*, 2021).

Output data from antiSMASH analysis are listed as BGC classes and predicted BGCs for each genome in **Table S2**. Only high-quality genomes, as assessed by CheckM with ≥90% completeness and ≤5% contamination ratio were used for the analysis. For R401, the PacBio-sequenced high-quality genome was used for BGC prediction using antiSMASH.

I.6.8 Mutant generation

Marker-free knockouts in R401 were generated through homologous recombination using the cloning vector pK18mobsacB (GenBank accession: FJ437239), which encodes the *kanR* and *sacB* genes conferring resistance to kanamycin and susceptibility to sucrose, respectively. In this method, upstream and downstream sequences of the gene to be deleted are integrated into the pKl8mobsacB suicide plasmid by Gibson assembly (Gibson *et al.*, 2009). The resulting plasmid is transformed into BW29427 *E. coli* cells and subsequently conjugated into R401. The plasmid is then integrated into the chromosome by homologous recombination and deletion mutants are generated by a second sucrose counter-selection-mediated homologous recombination event. The protocol is adapted from (Kvitko & Collmer, 2011).

Generation of pK18mobsaB-derived plasmid containing flanking regions of the gene of interest.

Primers were designed to amplify a 750-bp DNA sequence (*i.e.*, flanking region) directly upstream and downstream of the target region, sharing terminal sequence overlaps to the linearized pK18mobsacB vector and the other respective flanking region using Geneious Prime. R401 genomic DNA was isolated from 6 µl dense R401 culture in 10 µl of buffer I (pH 12) containing 25 mM NaOH, 0.2 mM EDTA at 95 °C for 30 min, before the pH was readjusted using 10 µl of buffer II (pH 7.5) containing 40 mM Tris-HCl. The R401 genomic DNA was used for amplification of the flanking regions through PCR using the respective flanking region-specific primer combinations (**Table S4**). PCR was conducted with 0.2 µl Phusion Hot Start High-Fidelity DNA polymerase (New England Biolabs) in 20-µl reactions containing 4 µl 5x Phusion HF buffer (New England Biolabs), 0.4 µl 10 mM dNTPs, 1 µl of 10 µM forward primer, 1 µl of 10 µM reverse primer, 2 µl of R401 genomic DNA as template, filled up to 20 µ1 with nuclease-free water. The tubes were placed into a preheated (98 °C) thermal cycler set at the following program: 98 °C for 30 s, 35 cycles of 98 °C for 7 s, 60 °C for 20 s, 72 °C for 15 s, then a final extension at 72 °C for 7 min. Five microliters of the PCR product were

combined with 1 µl Orange DNA Loading Dye (6x; New England Biolabs), loaded on 1% agarose gels containing 0.05% EtBr, and run at 110 mV. After confirmation of successful amplification, the PCR product was purified using AMPure XP (Beckman-Coulter) and subsequently quantified using Nanodrop (Thermo Fisher Scientific). Plasmid purification was performed on an *E. coli* culture containing plasmid pK18mobsacB using the QIAprep Spin Miniprep Kit for plasmid DNA purification (QIAGEN) following the manufacturer's instructions. The pkl8mobsacB vector was then amplified and linearized through PCR using the PKSF and PKSR primers (**Table S4**). PCR was conducted with 0.2 µl Phusion Hot Start High-Fidelity DNA polymerase (New England Biolabs) in 20-µl reactions, largely as described above with 1 µl 0.1 ng/µl pkl8mobsac as a template. Annealing temperature was decreased to 55 °C and extension time increased to 150 s for each cycle. Template DNA was digested by DpnI (New England Biolabs) in 50-µl reactions containing 1 µl DpnI, 1 µg DNA, 5 µl Cutsmart buffer (New England Biolabs) and filled up to 50 µl with nuclease-free water. The tubes were then incubated at 37 °C for 15 min followed by heat inactivation at 80 °C for 20 min. Five microliters of the DpnI-digested plasmid were combined with 1 µl Orange DNA Loading Dye and analysed by DNA agarose electrophoresis. Upon successful verification of amplification and digestion, the remaining sample was purified using AMPure XP and subsequently quantified using Nanodrop. Linearized pK18mobsacB and both flanking regions were mixed in a molar ratio of 1:3:3 into a 10-µl total volume, added to 10 µl 2X Gibson Assembly® Master Mix (New England Biolabs) and incubated at 50 °C for 1 h.

Transformation into chemically competent *E. coli* BW29427 cells

The vector was transformed into 50 µl chemically competent BW29427 *E. coli* cells according to the following heat shock protocol: 2 µl of the vector were gently mixed with 50 µl of competent cells, and the resulting mixture was incubated on ice for 30 min. The mixture was transferred to a water bath at 42 °C for 1 min and put back on ice for 2 min. Then, 1 ml of 50% TSB with 50 µg/ml diaminopimelic acid (DAP; Sigma-Aldrich) was added to the heat-shocked cells, the mixture was left to regenerate at 37 °C for 1 h and then plated on 50% TSA containing 25 µg/ml Kanamycin (Kan) and 50 µg/ml DAP. The plates were incubated at 37 °C overnight. Resulting colonies were validated by colony PCR using the M13F and M13R primers. Colony PCR was performed on at least four separate colonies with 0.4 µl DFS-Taq polymerase (BIORON) in 25 µl reactions containing 2.5 µl l0x incomplete buffer (BIORON), 0.5 10 mM MgC12, 0.5 µl 10 mM dNTPs, 0.75 µl 10 µM forward primer, 0.75 µl 10 µM reverse primer,

a small fraction of a colony and filled up to 25 µl with nuclease-free water. The tubes were placed in a thermocycler set at the following program: 94 °C for 2 min, 35 cycles of 94 °C for 30 s, 55 °C for 30 s, 72 °C for 2 min, then a final extension at 72 °C for 10 min. Five microliters of the PCR product were combined with 1 µl Orange DNA Loading Dye and analysed by DNA agarose electrophoresis. Positive colonies were purified by streaking on new 50% TSA plates containing 25 µg/ml Kan and 50 µg/ml DAP and further verified by Sanger sequencing (Eurofins Scientific) following the manufacturer's protocol.

Conjugation of *E. coli* and R401 and selection for first homologous recombination event

E. coli BW29427 cells containing the plasmid and R401 were inoculated into 4 ml of 50% TSB containing 25 µg/ml Kan and 50 µg/ml DAP or 50% TSB and incubated overnight at 37 °C with 180 rpm agitation or 25 °C with 180 rpm agitation, respectively. Cells were harvested by centrifugation at 8,000 rpm for 2 min at room temperature, then washed 3x and subsequently resuspended in 1 ml of 50% TSB followed by centrifugation, after which the supernatant was discarded. After quantifying OD_{600}, both cultures were mixed to equal parts and approx. 10x concentrated by centrifugation. The bacterial suspension was plated on 50% TSA plates containing 50 µg/ml DAP and incubated at 25 °C overnight to allow for conjugation events. The mating patches were scraped of the plate and resuspended in 1 ml 50% TSB. Then, 100 µl were spread on 50% TSA plates containing 25 µg/ml Kan and 50 µg/ml Nitrofurantoin (Nitro; Sigma-Aldrich; to counter-select *E. coli*) and incubated at 25 °C. Colonies were validated for successful genomic insertion of the plasmid *via* colony PCR using a primer specific to the genomic DNA approx. 150 bp upstream of the upward flanking region (upup) and the plasmid specific M13F primer. Colony PCR was performed on at least 15 separate colonies and a WT control with 0.4 µl DFS-Taq polymerase in 25-µl reactions as described previously, but with an annealing temperature of 60 °C. Five microliters of the PCR product were combined with 1 ml Orange DNA Loading Dye and analysed by DNA agarose electrophoresis followed by Sanger sequencing following the manufacturer's protocol.

Sucrose counter-selection to induce the second homologous recombination event

A R401 colony with a successful genomic insertion of the plasmid was resuspended from a plate into 1 ml of 50% TSB. The cell density in the medium was then measured using the Multisizer 4e Coulter Counter (Beckman Coulter) following the manufacturer's protocol. One

hundred microliters of 500 cells/µl, 5,000 cells/µl and 50,000 cells/µl dilutions were spread on three separate 50% TSA plates containing 300 mM sucrose. The plates were incubated at 25 °C for approx. 48 h. At least 30 colonies were examined by colony PCR using the respective upup and dwdw primers. Colony PCR was performed with 0.4 µl DFS-Taq polymerase in 25-µl reactions as described previously with an annealing temperature of 60 °C. Five microliters of the PCR product were combined with 1 µl Orange DNA Loading Dye and analysed by DNA agarose electrophoresis. Positive colonies were purified by streaking on new 50% TSA plates and further verified by Sanger sequencing (Eurofins Scientific) following the manufacturer's protocol. They were also streaked on 50% TSA containing 25 µg/ml Kan to verify loss of the plasmid. A second colony PCR was performed on positive colonies and a WT control to validate the absence of the GOI, using a forward (inF) and reverse (inR) primer inside the GOI. Colony PCR was performed with 0.4 µl DFS-Taq polymerase in 25 µl reactions as described previously. Five microliters of the PCR product were combined with 1 ml Orange DNA Loading Dye and analysed by DNA agarose electrophoresis. Upon successful verification, 4 ml of 50% TSB were inoculated with a positive colony and grown overnight at 25 °C at 180 rpm. Finally, 750 µl of the overnight culture were added to 750 µl of 50% glycerol in an internally threaded 1.8 ml Nunc CryoTube, gently mixed, and stored at -80 °C.

I.6.9 Establishment of mini-Tn5 transposon mutant collections in R401 and R569

Mini Tn5-mutant collections of R401 and R569 were established similarly with only minor changes as described below. Liquid cultures of R401 or R569 and *E. coli* strain BW29427 carrying plasmid pUTmTn5Km2 (Merrell *et al.*, 2002) were grown overnight in no antibiotics or 25 µg/ml Kan and 50 µg/ml DAP at 25 °C or 37 °C, respectively. Conjugation was carried out as described above in "*Conjugation of E. coli and R401 and selection for first homologous recombination event"*. For R401, the mating patch was taken up in 1 ml 50% TSB liquid medium and subsequently plated on 50% TSA plates containing 25 µg/ml Kan and 50 µg/ml Zeocin in four different dilutions (undiluted, 1:3, 1:4, and 1:5) and left to grow at 25 °C for 48 h. Individual colonies were picked in 100 µl sterile 50% TSB in 96-well culture plates, sealed and left to grow at 25 °C and 180 rpm for 24 h. Subsequently, 100 µl 50% glycerol were added to each well and plates were frozen until further processing. The outer rows and columns were left uninoculated as to avoid positional effects in the subsequent forward genetic screen. For R569, resuspended mating patches were stocked at -80 °C in 700-µl aliquots using a final concentration of 25% Glycerol. 1:4 dilutions were plated onto 50% TSA plates supplemented

with 120 µg/ml Kan, 50 µg/ml Rifampicin and 50 µg/ml Zeocin and incubated at 25 °C for 48h. Individual colonies were inoculated in 100 µl 50% TSB supplemented with the same antibiotics at the same concentrations in 96-well plates and incubated at 25 °C and 180 rpm for 48 h. Then, 100 µl 50% glycerol were added to each culture and plates were frozen at -80 °C.

I.6.10 Mini-Tn5 transposon mutant screen for loss of R401s growth inhibition of *Rs* GMI1600

Each R401 mini-Tn5 transposon mutant was screened individually for loss of inhibitory activity against GFP-expressing *Rs* GMI1600 and for wild type-like growth, as we observed in first trials that mutants that are impaired in growth are also more likely to have reduced inhibitory activity against *Rs* GMI1600. This screen was conducted in a 96-well plate format with GFP expression of *Rs* GMI1600 in response to individual R401 mutants and Abs_{600} of axenically grown, individual R401 mutants as readouts. Therefore, for each mutant, two wells were inoculated in parallel, one in the presence of *Rs* GMI1600 and one grown axenically. *Rs* GMI1600 was streaked on 50% TSA plates and left to grow at 25 °C for 96 h. The same day, R401 mutants were each inoculated into 150 µl Artificial Root Exudates (ARE; **Table S5**) in 96-well culture plates ('R401 preculture plates') from glycerol stocks using a multi-stamp replicator and left to grow at 25 °C and 150 rpm for 96 h until saturation. Then, a *Rs* GMI1600 preculture was inoculated into 10 ml ARE and grown overnight at 25 °C and 150 rpm. Approximately 24 h later, the preculture was 1:10 diluted with 90 ml ARE and left to grow under the same conditions. Approximately 24 h later, the 100 ml *Rs* GMI1600 culture was concentrated by centrifugation at 4,000 rpm for 15 min, washed 3x and resuspended in ARE. Subsequently, OD_{600} was quantified and set to 0.2 in ARE. Then, 75 µl of this *Rs* GMI1600 suspension were transferred to each well of a sterile 96-well bacterial culture plate (Greiner-CELLSTAR-96-Well plate, transparent, flatbottom; Sigma-Aldrich) per 'R401 preculture plate', referred to as the 'R401-*Rs* interaction plate'. Per 'R401 preculture plate' one sterile 96-well bacterial culture plate (Greiner-CELLSTAR-96-Well plate, transparent, flatbottom; Sigma-Aldrich) was filled with 150 µl ARE per well and R401 mutants were inoculated from the 'R401 preculture plate' using a multi-stamp replicator; this plate is referred to as the 'axenic R401 plate'. After mixing by pipetting, 75 µl R401 mutant suspension were transferred from the 'axenic R401 plate' to the 'R401-*Rs* interaction plate'. Finally, 75 µl ARE were added to each well of the 'axenic R401 plate'. The 'axenic R401 plate' and 'R401-*Rs* interaction plate' thereby contain the same volume and concentration of R401 mutants, while the latter also

contains a final concentration of OD_{600} 0.1 *Rs* GMI1600 per well. Both plates were closed with a lid and incubated at 25 °C and 150 rpm for 48 h. Subsequently, Abs_{600} was measured for the 'axenic R401 plate' and GFP fluorescence was quantified at $\lambda_{excitation}$=475 nm and $\lambda_{emission}$=510 nm for the 'R401-*Rs* interaction plate'. Both measurements were taken using a microplate reader (Infinite M200 PRO, Tecan). Subsequently, candidate R401 mutants were selected based on two criteria: (I) loss of *Rs* GMI1600 inhibition; a mutant was considered a candidate if the GFP fluorescence in the 'R401-*Rs* interaction plate' was lower than 3-fold the absolute deviation around the median (MAD; Leys *et al.*, 2013) compared to the respective plates median, and (II) wild-type-like growth; a mutant was considered a candidate if the Abs_{600} in the 'axenic R401 plate' was not lower than 3x MAD compared to the respective plate's median. Candidate R401 mutants were freshly picked from glycerol stocks and validated twice more independently using the same assay. Finally, 38 mutants that showed wild-type-like growth and robustly reduced inhibitory activity against *Rs* GMI1600 were subsequently tested in an orthogonal mBA experiment with *Rs* as target bacterium, as described before.

I.6.11 Mini-Tn5 transposon mutant screen for lack of pyoverdine fluorescence of R569

R569 mini-Tn5 mutants were cultured in 96 well plates at 25 °C and 180 rpm for five days in 50% TSB medium. For the initial mutant screen, fluorescence was acquired at $\lambda_{excitation}$=395 nm and $\lambda_{emission}$=470 nm in a microplate reader (Infinite M200 PRO, Tecan). Out of ~2,000 mutants analysed, the fluorescence-based screening identified twelve R569 mutants that showed severely reduced pyoverdine-specific fluorescence but retained median-like growth behaviour (Thresholds: -6x MAD fluorescence, >-1x MAD Abs_{600}). For validation, cultures were pre-grown for five days in 50% TSB before sub-culturing into fresh siderophore medium (see **Table S5**) and growth for five additional days. Finally, bacterial culture density (Abs_{600}) was determined, and pyoverdine-specific fluorescence of bacterial culture supernatants was captured at $\lambda_{excitation}$=410 nm and $\lambda_{emission}$=500 nm. For comparison between genotypes, fluorescence capacity was calculated by dividing the pyoverdine-specific fluorescence by culture density.

Identification of mini-Tn5 transposon integration sites in the genomes of R401 and R569

The chromosomal mini-Tn5 transposon integration sites in the R401 or R569 genomes were determined similarly as described before (Merrell *et al.*, 2002). Briefly, a colony from each

strain was resuspended in 20 µl of sterile deionized water. Subsequently, a two-step PCR (TAIL-PCR) was performed starting with an arbitrarily primed PCR (PCR1), followed by a nested PCR (PCR2) on the generated product using the primers as described (**Table S4**). PCR reactions were conducted using the BIORON DFS-Taq polymerase reaction kit according to the manufacturer's instructions. One microliter of a resuspended bacterial colony was used as template for PCR1 in a total PCR reaction volume of 25 µl. PCR1 was conducted using primers JO4 and JO28 and the following steps were applied: 95 °C for 5 min, six cycles of 95 °C for 15 sec, 30 °C for 30 sec and 1 min elongation at 72 °C, followed by 30 cycles with 95 °C for 15 seconds, 45 °C for 30 seconds and 1 min elongation at 72 °C. Final elongation was for 5 min at 72°C. PCR2 was conducted using 0.3 µl of the PCR1 product and the primers JO1 and JO5. The following steps were applied: 95 °C for 5 min followed by 30 cycles of 95 °C for 15 sec, 57 °C for 30 sec and 1 min elongation at 72 °C. Final elongation was for 5 min at 72°C. R401 or R569 wild type was included to account for unspecific amplifications. PCR products were separated by agarose gel electrophoresis. One of the most prominent bands from each sample was extracted using the Nucleospin Gel and PCR clean-up kit (Macherey-Nagel). The PCR product was eluted into a final buffer volume of 20 µl; DNA concentration was determined with a spectrophotometer (NanoDrop One, Thermo Scientific), and 75 ng of each product were sent for Sanger sequencing (Eurofins genomics). Finally, chromosomal Tn5 integration sites were assessed by alignment of the obtained sequences flanked by the integrated Tn5 transposon in the R401 or R569 genome using the Geneious Prime or CLC Genomics Workbench software, respectively (Qiagen Digital Insights). Matching open reading frames (ORFs) were further aligned to the NCBI BLAST (Altschul *et al.*, 1990) nucleotide and protein data base (using BLASTn and BLASTp algorithm).

I.6.12 Complementation of R401 Δ*pvdy*

Complementation of R401 Δ*pvdy* was conducted by expressing the coding region of R401 *pvdY* under its putative native promoter from a low-copy plasmid in the Δ*pvdy* mutant background. Plasmid construction was conducted using Gibson assembly as described before. In brief, the coding region of R401 *pvdY* was co amplified with a 1.5 kb region upstream of the gene and ligated into a linearized pSEVA22l (Martínez-García *et al.*, 2020) vector backbone. This vector was integrated into *E. coli* BW29427 cells and subsequently integrated into R401 Δ*pvdy via* bi-parental conjugation.

I.6.13 *In vitro* iron mobilization assay

The capability of R401 and R569 mutants of solubilizing inaccessible ferric iron was tested using a previously described photometric assay (Arora & Verma, 2017). Bacteria were cultured at 25 °C and 180 rpm for five days in 50% TSB and subsequently subcultured and 1:50 diluted in siderophore medium (**Table S5**). Diluted cultures were grown for an additional five days under the same conditions. At five days post inoculation (dpi), bacterial load was quantified by OD_{600} determination. Subsequently, cells were pelleted by centrifugation for 15 min at 4,000 rpm. The cell-free supernatant was diluted 5-fold with 10 mM $MgCl_2$ and 25 µl were mixed with 100 µl of CAS assay solution (Schwyn & Neilands, 1987) in three technical replicates and incubated for approx. 40 min at room temperature in the dark. Using an Infinite 200 PRO plate reader (TECAN), Abs_{636} was measured as an indication for the transition from complexed iron (blue complex) to solubilized or siderophore-bound iron (yellow). Finally, bacterial iron mobilizing capacity was computed according to the following formula:

$$Fe\text{–}mobilizing\ capacity\left[\frac{\mu M\ Fe}{OD_{600}}\right] = \frac{\left(\frac{(Abs_{636}(Medium) - Abs_{636}(Sample))}{(Abs_{636}(Medium)}\right) * 2\ nmol}{(Volume(Supernatant) * OD_{600})}$$

I.6.14 Validation of bacterial growth rates

The growth of individual R401 mutants and wild type was assessed by continuously measuring OD_{600} of actively growing bacterial cultures in an Infinite 200 PRO plate reader (TECAN) over 48 h at 25 °C and approx. 300 rpm. Overnight cultures in 50% TSB were pelleted and washed as described before. Subsequently, OD_{600} was measured and set to 0.02 in either artificial root exudates (ARE) or ARE lacking $FeCl_3$. Composition of ARE was adopted from Baudoin *et al.* (2003) and can be found in **Table S5**.

I.6.15 Microbiota reconstitution in the gnotobiotic Flowpot system

Flowpot assembly was performed according to Kremer *et al.* (2021) with minor adjustments. A 2:1 mixture of peat potting mix and vermiculite was used as a matrix. The matrix was sterilized two times (25 min liquid cycle (121 °C) and 45 min solid cycle (134 °C)) and stored at 60 °C until completely dry. Prior to Flowpot assembly, the matrix was rehydrated with sterile Milli-Q water. Flowpots were assembled by adding a layer of glass beads to the conical end of a truncated syringe, followed by a layer of the rehydrated, sterile substrate, subsequently covered

with a sterile mesh secured by a cable tie. Assembled Flowpots were sterilized on a 25 min liquid cycle, stored at 60 °C overnight and sterilized twice on a 45 min solid cycle. Bacterial strains, cultivated as described before, were harvested, 3x washed and pooled in equal ratios. Then, 1.25 ml bacterial pool (OD_{600} 1.0) were added to 500 ml of ½ MS medium for a final bacterial OD_{600} of 0.0025. Flowpots were first flushed with sterile Milli-Q water, then inoculated with 50 ml of ½ MS. Eight inoculated Flowpots were placed into each sterile microbox (TP1200, Sac O2) and stored at room temperature overnight. Exactly five sterilized seeds were sown per Flowpot and left to grow under the previously described conditions. At 21 dpi, shoot fresh weight was measured individually for each plant. Roots from a single Flowpot were thoroughly cleaned from soil particles in sterile water using tweezers. Six representative Flowpots were selected for harvesting root and matrix samples. Cleaned roots from each Flowpot were pooled in 2 ml lysing matrix E tubes (MP Biomedicals), snap-frozen and stored at -80 °C until further use. Additionally, <100 mg of soil was taken from each Flowpot, snap-frozen and stored in weighed 2 ml lysing matrix E tube (MP Biomedicals) at -80 °C until further use.

I.6.16 Mono-association experiment of R401 on *A. thaliana* seedlings in agar plates

This protocol is adapted from Ma *et al.* (2021). In brief, *A. thaliana* seeds were sterilized, germinated, and transferred to ½ MS agar plates without sucrose, as described before. After transfer of seedlings, plants were grown for another 14 days under the same conditions. R401 wild-type and mutants were grown in 50% TSB overnight as described before. Bacterial cells were pelleted by centrifugation, washed 3x in 10 mM $MgCl_2$ and OD_{600} was measured and adjusted to 0.0001. Agar plates were flushed with 15 ml of bacterial suspension for 5 min. The bacterial suspension was removed, and plants were carefully transferred to new ½ MS agar plates. After 24 h, roots were cut using a sterile scalpel and collected in pre-weighed, sterile 2 ml tubes containing 1 steel bead (3 mm diameter). Tubes were weighed again to assess the root fresh weight. Subsequently, roots were ground in a Precellys 24 TissueLyser (Bertin Technologies) for 2 x 30 s at 6,200 rpm at 15 s intervals. Then, 250 µl of sterile 10 mM $MgCl_2$ were added to each tube and roots were ground again under the same conditions. Each sample was subsequently 5x 1:10 diluted in sterile 10 mM $MgCl_2$. Undiluted samples and each dilution were plated on 50% TSA square plates, dried and left to grow at 25 °C until single colonies appeared. Pictures were taken and single colonies were counted blinded.

I.6.17 Mono-association experiment of R401 on *A. thaliana* seedlings in Flowpots

Flowpots were assembled, autoclaved, and flushed with sterile Milli-Q water, as described before. R401 wild-type and the Δ*pvdl*Δ*phld* double mutant were grown in 50% TSB overnight as described previously. Bacterial cells were pelleted by centrifugation, washed three times in 10 mM $MgCl_2$ and OD_{600} was measured and adjusted. Finally, 600 µl of OD_{600} 1 were inoculated into 300 ml ½ MS medium resulting in a final bacterial concentration of OD_{600} 0.002. Each Flowpot was flushed with 50 ml of ½ MS containing the bacterial inoculum. Per condition, six Flowpots were placed in a sterile microbox (Sac O2) and stored overnight. The next morning, exactly five seeds were inoculated per Flowpot and left to grow under the previously described conditions. After 21 days, roots were carefully cleaned as described above, dried and collected in pre-weighed, sterile 2 ml tubes containing 1 steel bead (3 mm diameter). Tubes were weighed again to assess the root fresh weight. Subsequently, roots were ground in a Precellys 24 TissueLyser (Bertin Technologies) for 2 x 30 s at 6,200 rpm with 15 s intervals. Then, 150 µl of sterile 10 mM $MgCl_2$ were added to each tube and roots were ground again under the same conditions. Each sample was subsequently dilute five times 1:10 in sterile 10 mM $MgCl_2$. Undiluted samples and each dilution were plated on 50% TSA square plates, dried and left to grow at 25 °C until single colonies appeared. Pictures were taken and single colonies were counted blinded.

1.6.18 DNA isolation

For DNA extractions, root and soil samples were homogenized in a Precellys 24 TissueLyser (Bertin Technologies) for 2 x 30 s at 6,200 rpm with 15 s intervals. DNA was extracted with a modified, high-throughput version of the FastDNA SPIN kit for Soil (MP Biomedicals). In brief, samples were taken up in sodium phosphate buffer (MP Biomedicals) and MT buffer (MP Biomedicals), then homogenized as described before. After centrifugation for 15 min at 13,000 rpm, 150 µl of the supernatant were transferred to a 96-well Acroprep Advance filter plate (with 0.2 µm Supor filter; Pall). Once full, the filter plate was positioned on a PCR plate filled with 50 µl Binding Matrix (MP Biomedicals) per well and centrifuged for 15 min to remove residual soil particles. This and all subsequent centrifugation steps were carried out in a swing out centrifuge at 1,500 rpm. The PCR plate was sealed and shaken for 3 min to allow binding of the DNA to the Binding Matrix. The suspension was pipetted onto a second filter plate of the same kind, positioned on a collection plate, and centrifuged for 15 min. The flowthrough was discarded. Then, 200 µl SEWS-M washing buffer (MP Biomedicals) were pipetted into each

well of the filter plate and centrifuged for 5 min. This washing step was carried out a second time. The flowthrough was discarded and followed by centrifugation for 5 min to remove residual SEWS-M buffer. Finally, 30 µl nuclease-free water were added to each well and left to incubate at room temperature for 3 min. Subsequent centrifugation for 5 min eluted the DNA into a clean PCR plate. The resulting DNA was used for v5v7 *16S* rRNA region amplification without prior adjustment of DNA concentrations.

I.6.19 Library preparation for bacterial *16S rRNA* gene profiling

The v5v7 variable regions of the bacterial *16S* rRNA gene were amplified in 96-wells plates through PCR using 799F and 1192R primers (PCR I; **Table S4**). PCR I was performed with 0.4 µl DFS-Taq polymerase (BIORON) in 25-µl reactions containing 2.5 µl l0x incomplete buffer (BIORON), 0.5 µl l0 mM $MgC1_2$, 2.5 µl 3% BSA, 0.5 µl 10 mM dNTPs, 0.75 µl 10 µM 799F, 0.75 µl 10 µM 1192R, 1 µl of isolated DNA and adjusted to 25 µl with nuclease-free water. Samples were placed in a thermocycler set at the following program: 94 °C for 2 min, 25 cycles of 94 °C for 30 s, 55 °C for 30 s, 72 °C for 1 min, then a final extension at 72 °C for 10 min. Remaining primers and dNTPs were digested by Antarctic phosphatase and Exonuclease I. To each 25 µl PCR reaction, 1 µl of Antarctic phosphatase (New-England BioLabs), 1 µl of Exonuclease I (New-England BioLabs) and 3 µl of Antarctic phosphatase buffer (New-England BioLabs) were added; the resulting mixture was incubated at 37 °C for 30 min followed by heat inactivation of the enzymes at 85 °C for 15 min. The digested PCR I product was centrifuged at 3,000 rpm and 4 °C for 10 minutes. Then, 3 µl of the supernatant were used as a template in a second PCR, using a unique combination of uniquely barcoded 799F- and 1192-based primers containing Illumina adaptors for each sample (PCR II; **Table S4**). PCR II was performed with 0.4 µl DFS-Taq polymerase in 25-µl reactions containing 2.5 µl 10x incomplete buffer, 0.5 µl 10 mM $MgC1_2$, 2.5 µl 3% BSA, 0.5 µl 10 mM dNTPs, 0.75 µl 10 µM unique forward primer, 0.75 µl 10 µM unique reverse primer, 3 µl cleaned PCR I-product and adjusted to 25 µl with nuclease-free water. Samples were placed in a thermocycler set at the following program: 94 °C for 2 min, 10 cycles of 94 °C for 30 s, 55 °C for 30 s, 72 °C for 1 min, then a final extension at 72 °C for 10 min. Subsequently, 5 µl of the PCR product were combined with 1 ml Orange DNA Loading Dye, loaded on a 1% agarose gel containing 0.05% EtBr, and run at 110 mV. The expected PCR-product was an approx. 500 bp band containing the variable v5v7 regions, barcodes, and Illumina adaptors. After verification of successful amplification, samples were purified by AMPure XP (Beckman-Coulter) according to the manufacturer's protocol.

The DNA concentrations of each sample were quantified using the Quant-iT dsDNA Assay-Kit (Invitrogen) and pooled per full factorial replicate in equimolar values. All pools were purified twice using AMPure XP and fluorescently quantified using the Quant-iT dsDNA Assay-Kit. All pooled samples were combined into a single pool based on equimolarity and subsequently purified three times using AMPure XP and fluorescently quantified using the Qubit dsDNA HS Assay Kit (Invitrogen). The final concentration was set to 10 ng/µl. Paired-end Illumina sequencing was performed in-house using the MiSeq sequencer and custom sequencing primers (**Table S4**).

I.6.20 Analysis of *16S* profiling data

ASV table generation

Amplicon sequencing reads from *A. thaliana* roots and Flowpot soil were quality filtered and demultiplexed according to their barcode sequence using QIIME (Caporaso *et al.*, 2010) and unique amplicon sequencing variants (ASVs) were inferred from error-corrected reads, followed by chimera filtering. ASVs were mapped to the reference 16S rRNA sequences (downloaded from "www.at-sphere.com") to generate an ASV count table. All steps were carried out using the Rbec R package (Zhang *et al.*, 2021). Analysis was performed on samples with a sequencing depth of at least 500 high-quality reads.

Alpha- and beta-diversity

Analyses and visualization were performed in the R statistical environment (Version 4.1.2). Alpha and beta diversity were calculated on non-rarefied ASV count tables (McMurdie & Holmes, 2014). Alpha-diversity (Shannon index) was calculated with the "plot_richness" function in phyloseq package (McMurdie & Holmes, 2013).

Beta-diversity (Bray-Curtis dissimilarities) was calculated using the "ordinate" function in phyloseq package and used for unconstrained ordination by Principal Coordinate Analysis (PCoA). Statistical significances were assessed using permutational multi-variate analysis of variance (PERMANOVA) using the adonis function in the vegan package (Dixon, 2003).

I.6.21 Data analysis and statistics

All statistical analyses were conducted in R 4.1.2. Data visualisation was conducted using the ggplot2 package (as part of the Tidyverse) or the ggpubr package. Data normality was tested using the Shapiro-Wilk test. For normally distributed data, ANOVA and Tukey's HSD with correction for multiple comparisons were used. As nonparametric tests, Kruskal-Wallis followed by Dunn's post-hoc test and Benjamini-Hochberg (BH) adjustment for multiple comparisons were used. The respective statistical tests are indicated in each figure description. Significance was indicated by asterisks (∗, ∗∗, and ∗∗∗, indicate $p.adj \leq 0.05$, 0.01, and 0.001, respectively) or by significance group ($p \leq 0.05$). No statistical methods were used to pre-determine sample sizes. Phylogenetic trees were computed using Clustal Omega and subsequently visualised using iTol. Metabolomics and *16S* rRNA gene profiling data were analysed and visualized as described above. Halo size quantification in mBA experiments were performed blinded using the Fiji package of ImageJ. Colony counts of R401 were performed blinded. Figures were assembled in Adobe Illustrator.

I.7 Acknowledgements

This research was funded by the Deutsche Forschungsgemeinschaft (DFG, German Research Foundation) under Germany's Excellence Strategy – EXC-number 2048/1 – project 390686111, a European Research Council advanced grant (ROOTMICROBIOTA) to P.S.-L., as well as funds to P.S.-L. from the Max Planck Society. Furthermore, this work was supported by funds to S.H. from a European Research Council starting grant (MICRORULES 758003) and the Max Planck Society, as well as the Cluster of Excellence on Plant Sciences (CEPLAS) and the Priority Program: Deconstruction and Reconstruction of the Plant Microbiota (SPP DECRyPT 2125; project P.S.-L.: SCHU 799/8-1; project S.H.: HA 8169/2-2), both funded by the Deutsche Forschungsgemeinschaft. Work in the Schäberle lab was supported by the German Federal Ministry of Education and Research (BMBF). L.W. was funded by the China Scholarship Council (CSC NO. 201908080177). K.S. and Y.I. were funded through JP22H00364. We thank the Max Planck-Genome-Centre Cologne for advising and performing the resequencing of the R401 genome and Jose Flores-Uribe for his support in the genome assembly and annotation. We thank Daniel Machado for his constructive feedback on the analyses. We also thank Brigitte Pickel for her support in halo size quantifications and Flowpot harvest and Dieter Becker for his help in establishing the R401 Tn5 mutant library. Finally, thanks to Neysan Donnelly for editing this chapter and Saurabh Pophaly for support with ENA and NCBI data submission.

I.8 Supplementary figures

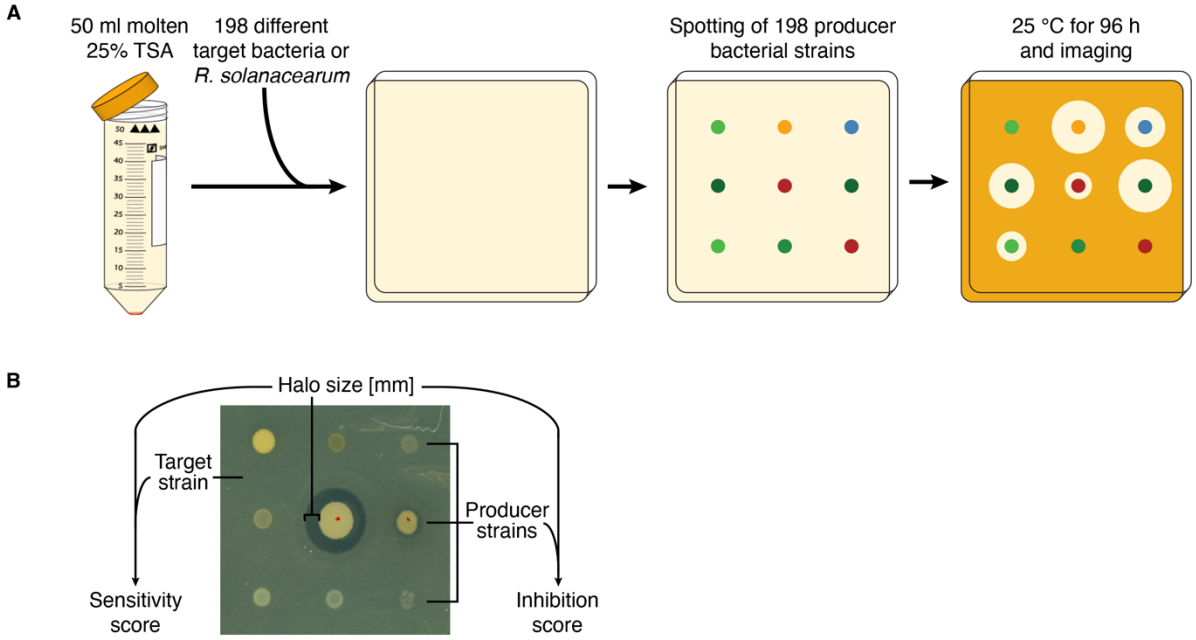

Figure S1, related to Figure 1. Flowchart and output example of the modified Burkholder assay (mBA) screen. (A) Schematic illustration of the screen for interbacterial interactions in a mBA. First, 100 µl of a bacterial solution from one strain are re-suspended in 50 ml of cooled, but molten 25% tryptic soy agar (25% TSA) and poured into a petri dish. Then, 24 bacterial strains are spotted on top of the solidified medium. The plates are incubated for 96 h at 25 °C. Pictures are taken and the size of the halo of inhibition is measured. **(B)** An example agar plate depicting a halo of inhibition produced by a producer strain on the bacterial lawn of a target strain, grown in 25% TSA. Explanation of nomenclature used in **Fig. 1**.

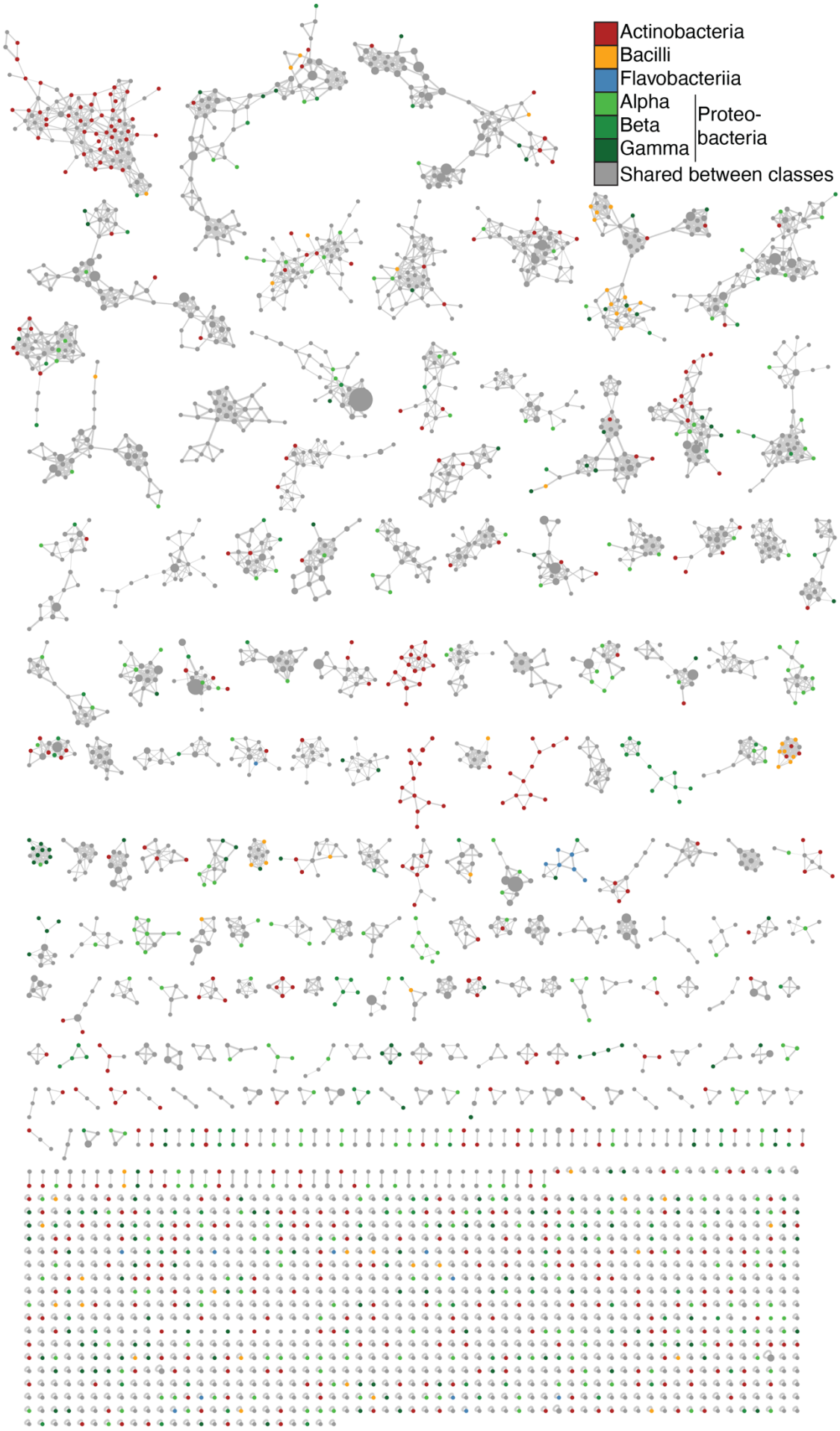
Actinobacteria
Bacilli
Flavobacteriia
Alpha
Beta
Gamma
Proteo-
bacteria
Shared between classes

Figure S2, related to Figure 2. Identification of class-specific exometabolites. The metabolomes of all 198 individual strains were assessed using liquid chromatography tandem mass spectrometry (UPLC-MS/MS). Molecular networking of bacterial metabolites obtained from organic extracts of the 198 strains, grown separately on 25% TSA for 96 h, was determined based on the Global Natural Products Social (GNPS) molecular networking workflow. The network consists of 3,314 nodes and 247 clusters (*i.e.*, molecular families) with at least two nodes and 1,046 singletons. Node sizes correspond to number of obtained spectra. Shared metabolites between at least two strains belonging to different classes are coloured in grey. Metabolites that are unique to one class are coloured according to the respective class colour code.

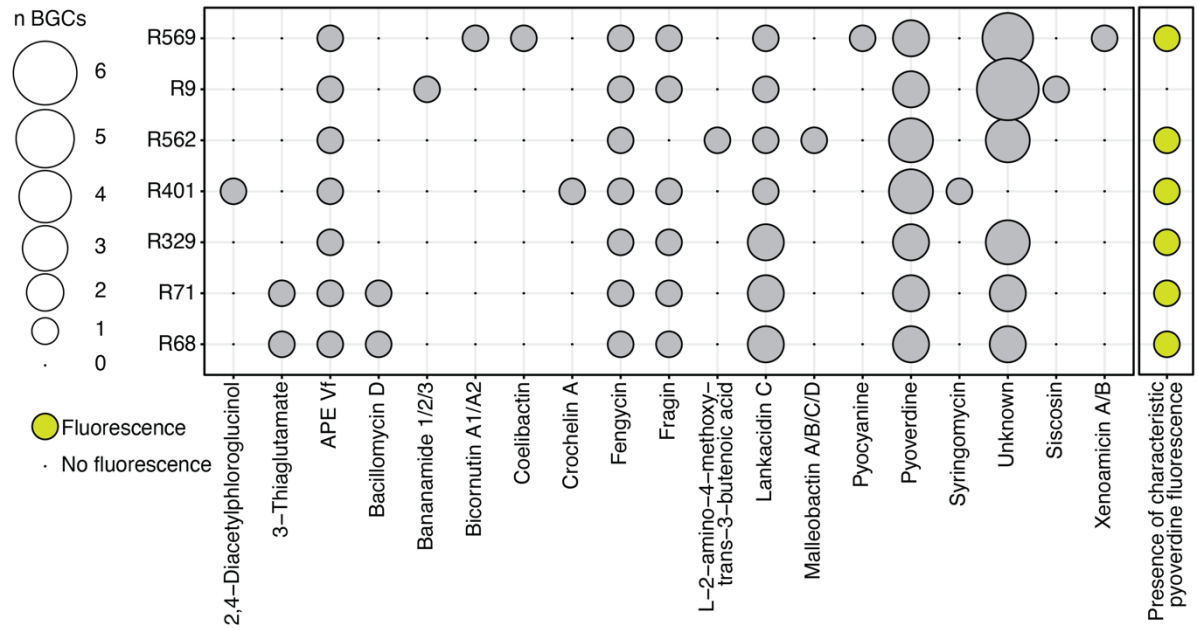

Figure S3, related to Figure 3 and 4. Genetic potential for the biosynthesis of specialized metabolites by all tested *Pseudomonas spp.* strains. Using antiSMASH, we predicted BGCs for all genomes of the herein-included bacteria. All predicted BGCs within the seven tested *Pseudomonas spp.* strains are depicted in grey and are named according to the putatively produced metabolite. In light green, the presence or absence of pyoverdine-specific fluorescence, which is indicative of pyoverdine production, is highlighted.

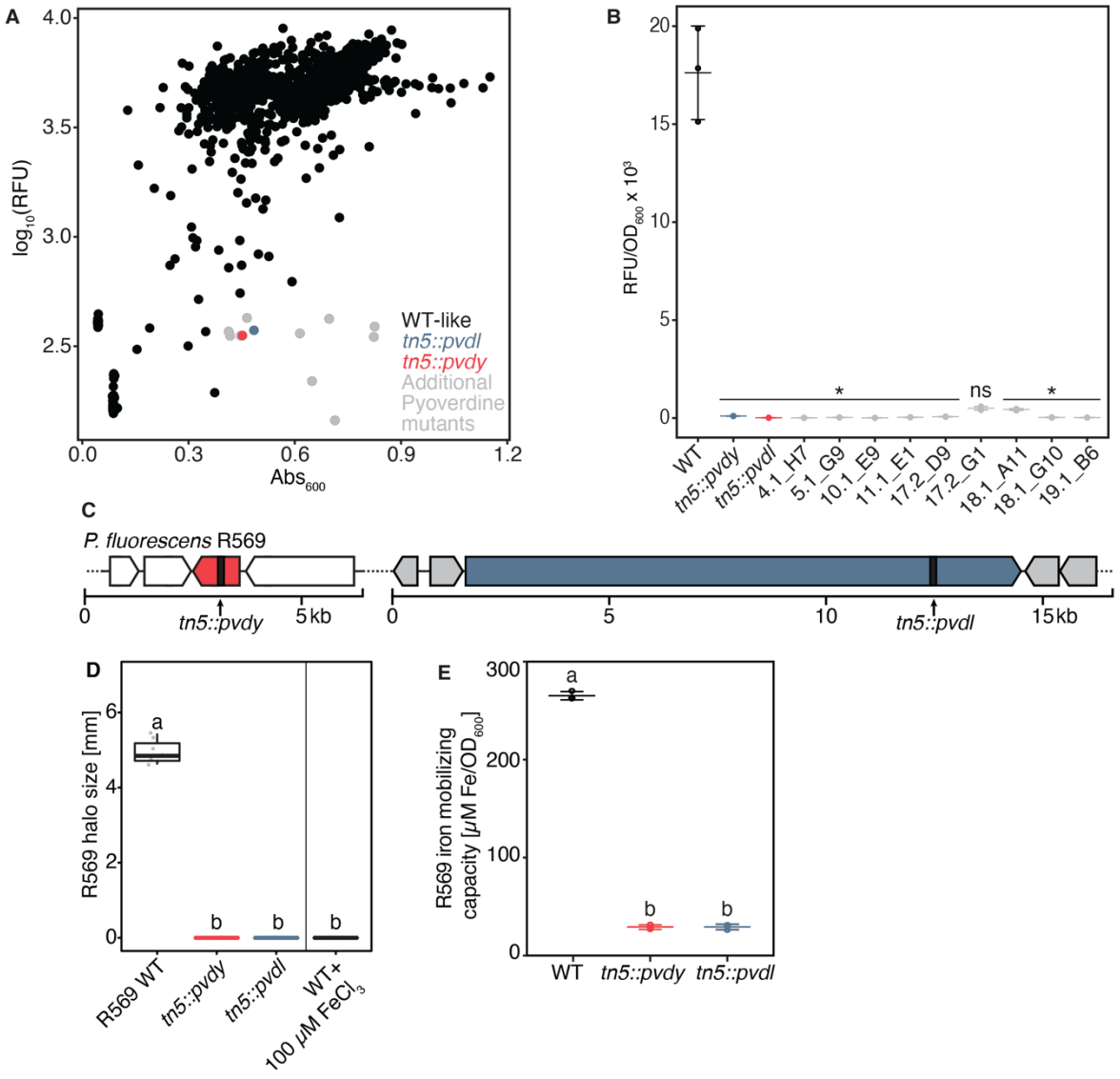

Figure S4, related to Figure 4. Pyoverdine produced by *Pseudomonas fluorescence* R569 acts as a sole inhibitory exometabolite. (A) Initial screen for the lack of pyoverdine-specific fluorescence of approx. 2,000 R569 mutants with single random mini-Tn5 integration sites in the genome. Using a plate reader, pyoverdine-specific fluorescence (excitation at 395 nm and emission at 470 nm) and OD_{600} of individual R569 mutants were quantified. Twelve mutants with WT-like growth (> -1x MAD) and reduced pyoverdine-specific fluorescence (< -6x MAD) are highlighted in blue, red or light grey. **(B)** Eleven out of the previously identified twelve putative pyoverdine mutants were independently confirmed for their lack of pyoverdine-specific fluorescence normalized to the mutants Abs_{600}. Statistical significance was determined by Kruskal-Wallis followed by Fisher's LSD post-hoc test and Benjamini-Hochberg adjustment. Significance compared to WT is indicated by black asterisks (∗ indicate $p < 0.05$; n=3). **(C)** Schematic overview of the genomic context of the fragmented *pvd*-operon which encodes a fraction of all pyoverdine biosynthetic genes of *P. fluorescence* R569. Genes within the BGC are coloured in grey, *pvdY* and *pvdL* are highlighted in red and blue, respectively. Transposon integration sites are highlighted by vertical black bars. **(D)** Halo production of R569 WT and two transposon-insertion mutants that are impaired in the production of pyoverdine (*tn5::pvdy, tn5::pvdl)*. Mutant names and colours are depicted as in **(C)**. *Rs* was used as a target strain. Halo size measurements were taken after three days of interaction. Letters indicate statistically significant differences as determined by Kruskal-Wallis followed by Dunn's post-hoc test and Benjamini-Hochberg adjustment with $p < 0.05$ (n=9). **(E)** Ferric iron mobilizing activity of R569 WT and mutants that

are impaired in the production of pyoverdine. Letters indicate statistically significant differences as determined by Kruskal-Wallis followed by Dunn's post-hoc test and Benjamini-Hochberg adjustment with $p < 0.05$ (n=3).

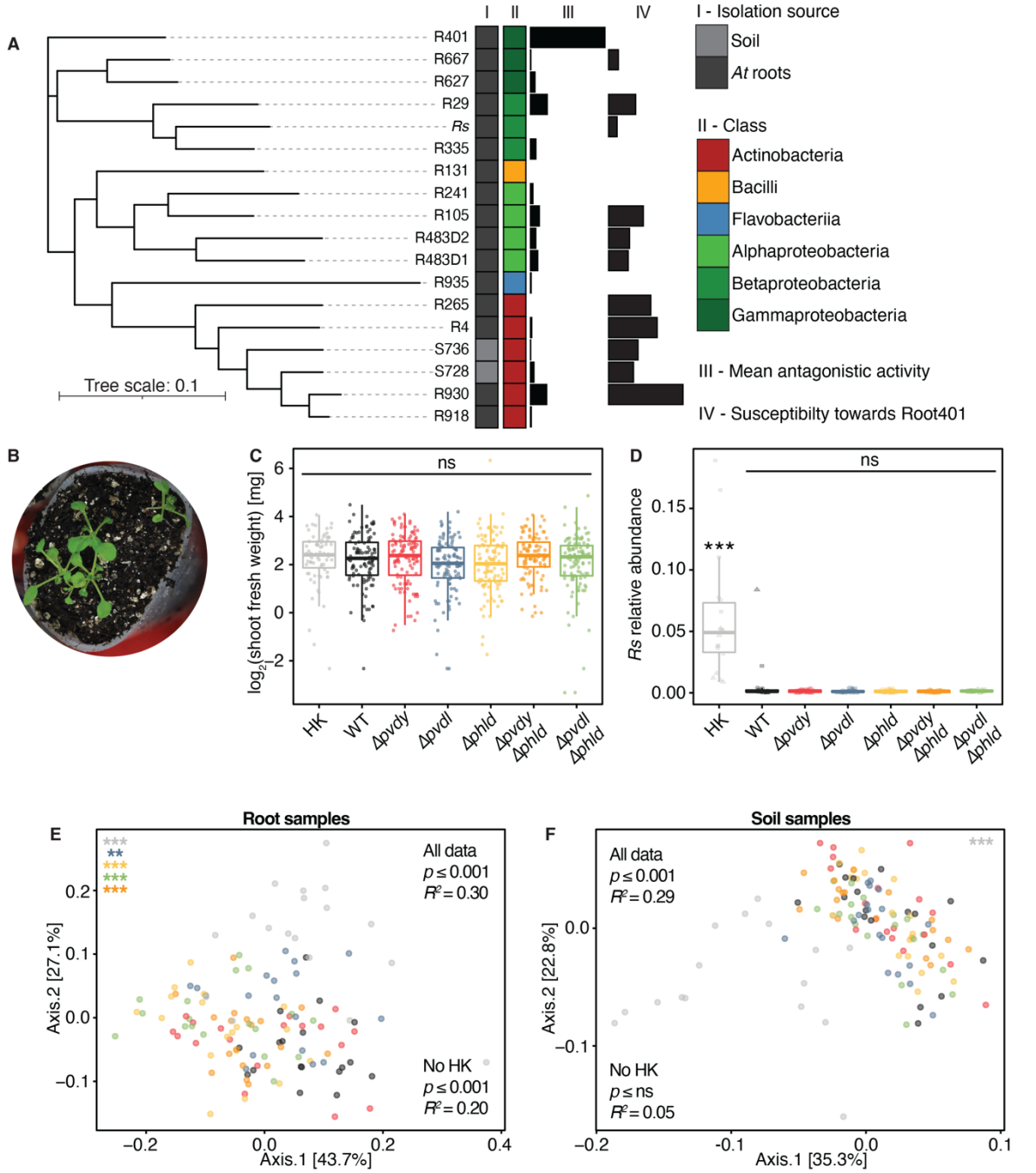

Figure S5, related to Figure 5. *R. solanacearum* does not cause disease symptoms in the tested conditions. (A) Phylogenetic tree of SynCom members based on v5v7 16S rRNA genes. The tree depicts the mean inhibitory activity **(III)** shown in **Fig. 1** as well as the mean sensitivity to R401 WT **(IV)** also derived from **Fig. 1**. For more precise taxonomic assignments of SynCom members please see **Table S1**. **(B)** Exemplary image of a Flowpot with HK treatment at 21 dpi. **(C)** log2-transformed shoot fresh weight of *A. thaliana* plants grown in the gnotobiotic Flowpot system for 21 dpi. No statistical difference ('ns') could be determined by Kruskal-Wallis followed by Dunn's post-hoc test and Benjamini-Hochberg adjustment (n=18). **(D)** Relative abundance of *R. solanacearum* on the *A. thaliana* roots at 21 dpi. Statistical significance

was determined by Kruskal-Wallis followed by Dunn's post-hoc test and Benjamini-Hochberg adjustment. Significance compared to WT is indicated by black asterisks (*** indicates $p < 0.001$; ns, not significant; n=18). **(E–F)** Unconstrained PCoA of bacterial beta diversity (Bray-Curtis dissimilarity) of root **(E)** and soil samples **(F)** in response to R401 or its mutants. Prior to computing relative abundances, R401 reads have been *in silico*-depleted to visualize solely the effect on the other SynCom members. PERMANOVA analysis-derived *p*-values are represented as asterisks (**, ***, indicate $p < 0.001$ or 0.001, respectively; n=18), coloured by the respective condition. PERMANOVA analysis on the full data set before (All data) or after (No HK) *in silico* depletion of HK samples are indicated in black; R^2 represents the variance explained by R401 genotype.

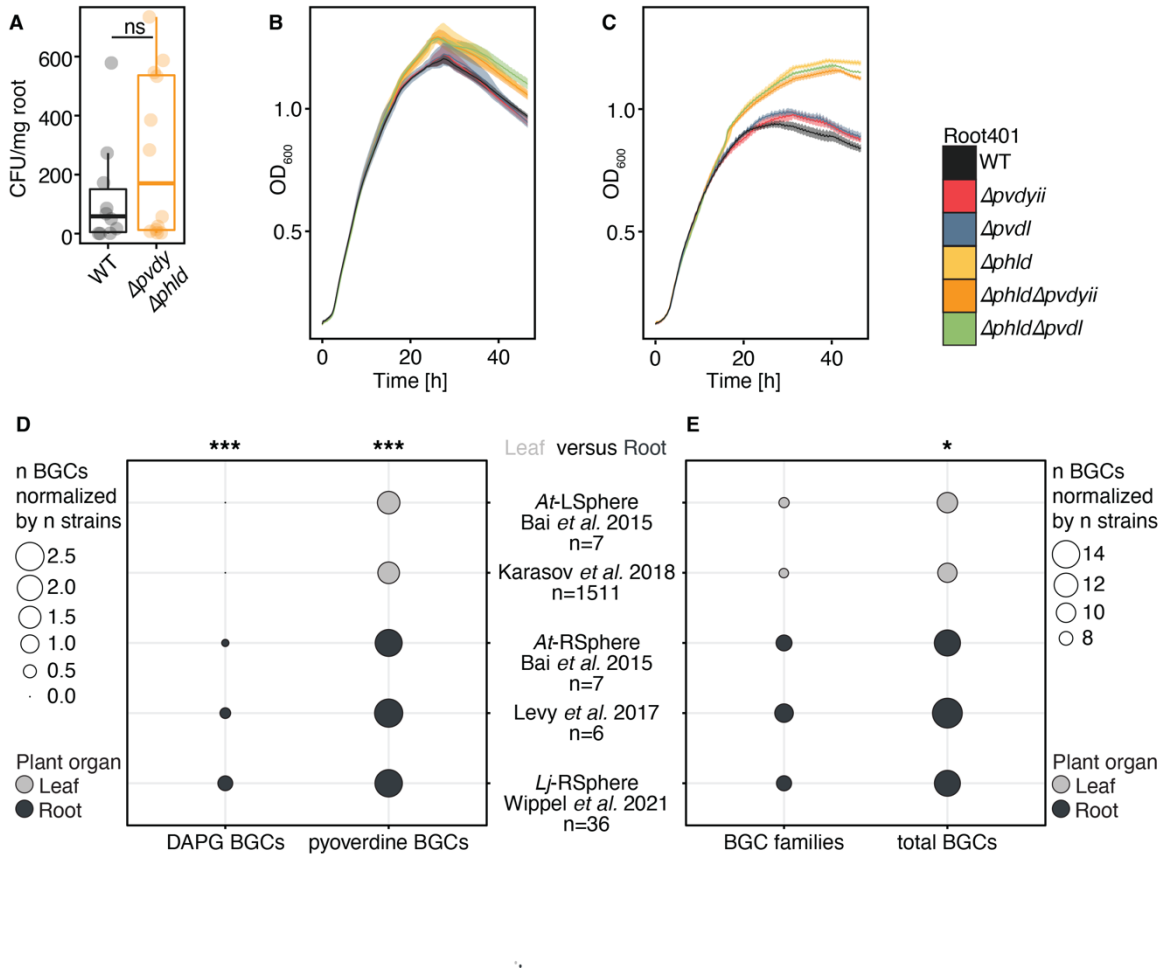

Figure S6, related to Figure 6. R401 DAPG and pyoverdine BGCs are predominantly detected in the genomes of root-derived *Pseudomonas sp.* isolates. (A) Colonization efficiency as measured by colony forming units of R401 WT and the Δ*pvdl*Δ*phld* double mutant on *A. thaliana* roots in mono-associations in the Flowpot system at 21 dpi. No statistical difference ('ns') could be determined by Kruskal-Wallis followed by Dunn's post-hoc test and Benjamini-Hochberg adjustment (n=12). **(B–C)** Growth curves of R401 WT and mutants in artificial root exudate (ARE) liquid medium **(B)** and ARE without any addition of iron **(C)**; n=6. Artificial root exudates are used to recapitulate the nutritional status in the vicinity of the root. **(D–E)** Using antiSMASH, we predicted BGCs for the genomes of *Pseudomonas sp.* isolates from different root and leaf derived culture collections. For each culture collection, the number of DAPG and pyoverdine BGCs **(D)** and the number of detected BGC families and total BGCs **(E)** is depicted. Dot size indicates number of detected BGCs normalized by the number of tested strains ('n'). Asterisks highlight statistical significance between

root and leaf culture collections as measured by Chi-Square test (∗, ∗∗∗, indicate $p < 0.05$, and 0.001, respectively).

I.9 Supplementary tables

Table S1, mBA binary interaction data and SynCom selection.

Table S2, antiSMASH-based BGC predictions.

Table S3, Generated R401 and R569 mutants.

Table S4, Primers used in this study for amplification of the bacterial v5v7 *16S* rRNA region and for generation and validation of bacterial mutants.

Table S5, Artificial root exudates and siderophore assay media.

All supplementary tables have been deposited at EDMOND and can be accessed *via* the following link: https://doi.org/10.17617/3.I1ABIM

Chapter II: Physicochemical interaction between osmotic stress and a bacterial secondary metabolite promotes plant disease

Authors

Felix Getzke[1,6], Lei Wang[2,6], Nienke Denissen[1], Fantin Mesny[1], Ka-Wai Ma[1], Hidde Wesseler[1], Alicia Jiménez Fernández[1], Paul Schulze-Lefert[1,2], Till F. Schäberle[3,4,5,*], Stéphane Hacquard[1,2,*]

Affiliations

1 Department of Plant Microbe Interactions, Max Planck Institute for Plant Breeding Research, 50829 Cologne, Germany

2 Cluster of Excellence on Plant Sciences (CEPLAS), Max Planck Institute for Plant Breeding Research, 50829 Cologne, Germany

3 Institute for Insect Biotechnology, Justus-Liebig-University Giessen, 35392 Giessen, Germany.

4 German Centre for Infection Research (DZIF), Partner Site Giessen-Marburg-Langen, 35392 Giessen, Germany

5 Fraunhofer Institute for Molecular Biology and Applied Ecology (IME), Branch for Bioresources, 35392 Giessen, Germany

6 These authors contributed equally

***Correspondence: Till F. Schäberle – Till.F.Schaeberle@agrar.uni-giessen.de; Stéphane Hacquard – hacquard@mpipz.mpg.de**

II.1 Summary

In nature, plants are colonized by diverse microbial communities that mainly comprise bacteria. Isolation of bacteria from roots and shoots of asymptomatic *Arabidopsis thaliana* plants has identified few isolates that can cause disease on *A. thaliana* under laboratory conditions, indicating the existence of molecular mechanisms that prevent disease in nature. Here, we demonstrate that the application of hyperosmotic NaCl concentrations is required for the virulence of the root-derived isolate *Pseudomonas brassicacearum* Root401 (R401) in a natural soil and for root-specific transcriptional reprogramming induced by R401. Our data suggests little involvement of root immunity to R401 disease emergence under salt stress. Instead, we identify the bacterial non-ribosomal peptide Brassicapeptin A as necessary and sufficient for the detrimental impact of R401 on salt-stressed *A. thaliana*. Brassicapeptin A increases host plasma membrane permeability, explaining its detrimental activity under hyperosmotic stress. Collectively, we delineate a salt stress-dependent mechanism that facilitates disease caused by an opportunistic root pathogen.

Keywords
plant disease, root microbiome, opportunistic pathogens, non-ribosomal peptide, abiotic stress, biotic stress, immunity, microbiota

II.2 Author contributions

F.G., S.H. and P.S.L. developed the project. F.G. designed the experiments. L.W. and T.F.S. isolated Brassicapeptin. F.G. and N.D. performed Flowpot experiments. N.D. determined R401 load on roots and shoots. F.G. and H.W. performed CAS and the initial agar plate experiment. F.M. performed initial RNA sequencing data analysis including DEG computation. F.G. performed all other RNA sequencing analysis. K.-W.M. performed the final agar plate experiment. F.G. performed all Brassicapeptin A experiments. S.H. supervised the project. F.G. and L.W. generated the figures. F.G. wrote this chapter, with L.W. providing the first draft on R401 structure elucidation.

II.3 Introduction

Subterranean and aerial plant tissues are colonized by microbial communities that primarily comprise bacteria but also filamentous eukaryotes such as fungi. Collectively, these microbial assemblages of subterranean and aerial plant tissues are referred to as the root and shoot microbiota, respectively (Agler *et al.*, 2016; Bai *et al.*, 2015; Durán *et al.*, 2018; Thiergart *et al.*, 2019). Recent efforts to systematically isolate and characterise the root and shoot microbiota of *A. thaliana* plants grown in natural soils has revealed that taxonomically diverse root- and leaf-associated microorganisms isolated from asymptomatic plants can cause disease under laboratory conditions (Durán *et al.*, 2018; Karasov *et al.*, 2018; Ma *et al.*, 2021; Pfeilmeier *et al.*, 2021). Namely, *Pseudomonas brassicacearum* Root401 (R401), *Streptomyces sp.* Root107 (R107) and *Xanthomonas sp.* Leaf131 (L131) were isolated from *A. thaliana* roots and leaves, respectively, and can cause disease in mono-associations (Bai *et al.*, 2015). The identification of these putatively dormant opportunistic pathogens suggests the existence of molecular mechanisms that suppress detrimental phenotypes in nature while facilitating virulence under laboratory conditions.

Stevens (1960) advanced the concept of the 'disease triangle', by which environmental factors contribute to the establishment of plant diseases. In this triangle, abiotic conditions can influence the host, the pathogen, or the interaction of the two, facilitating or inhibiting disease progression (Francl, 2001). Similar to pathogen perception, the sensing of salt stress for example results in signalling cascades involving cytoplasmic Ca^{2+} influx, reactive oxygen species (ROS) production *via* respiratory burst oxidases (RBOs), including RBO homologue D (RBOHD) and the systemic accumulation of plant hormones, primarily abscisic acid (ABA; Hua *et al.*, 2012; Zhang *et al.*, 2009; Zhu, 2002, 2016). ABA mediates rapid responses to salt stress such as the closure of stomata to restrict transpirational water loss. Furthermore, ABA elicits profound transcriptional reprogramming and induction of stress-related genes (J. K. Zhu, 2002, 2016). Hormonal pathways in plants are heavily interconnected and often antagonistic. For example, ABA inhibits the expression of the salicylic acid (SA) biosynthetic gene *ISOCHORISMATE SYNTHASE1* (*ICS1/SID2*) in *Arabidopsis thaliana*, thereby suppressing SA-dependent immunity (Pieterse *et al.*, 2012; Yasuda *et al.*, 2008). As a result, ABA facilitates disease caused by biotrophic plant pathogens, including the fungal pathogen *Magnaporthe grisea* and *Pseudomonas syringae* in *Oryza sativa* and *A. thaliana*, respectively (Fan *et al.*, 2009; Jiang *et al.*, 2010). The necrotrophic fungal pathogen *Botrytis cinerea* produces ABA resulting in increased virulence on *Solanum lycopersicum*, through immunity modulation *via*

the second messenger nitric oxide (NO; Sivakumaran *et al.*, 2016). Collectively, therefore, abiotic stress signalling can influence different sectors of the plant innate immune system resulting in increased susceptibility to both biotrophic and necrotrophic pathogens.

Here, we dissect the molecular and ecological mechanisms that explain R401 virulence. We demonstrate that NaCl treatment facilitates R401 virulence in non-sterile natural soils and in peat-based gnotobiotic growth systems, providing evidence for environmental factors that can facilitate R401 virulence under natural conditions. Sequencing of the *A. thaliana* shoot and root transcriptome reveals a root-specific response to combinatorial treatments of R401 and NaCl treatment, indicating a root-specific virulence phenotype. In R401, we identify a homologous BGC to the *syp-syr* BGC that is responsible for Syringopeptin biosynthesis in *P. syringae* B728a. Using targeted mutagenesis, we demonstrate that R401 Syringopeptin (termed Brassicapeptin) is required for virulence in salt-stressed plants. Subsequently, we isolate and structurally characterise R401 Brassicapeptin. Finally, we provide evidence that R401 Brassicapeptin directly interacts with high salt concentrations and is sufficient to explain the detrimental activity of R401 in an agar-based system. Collectively, our data proposes a disease mechanism through the interaction of a bacterial virulence factor and abiotic conditions.

II.4 Results

II.4.1 Detrimental activity of *Pseudomonas brassicacearum* R401 is facilitated by salt stress in soil

Inoculation of *Pseudomonas brassicearum* R401 on *Arabidopsis thaliana* plants grown on ½ Murashige-Skoog (½ MS) agar plates causes extensive root and shoot growth inhibition and anthocyanin accumulation in shoots (Ma *et al.*, 2021). We could reproduce similar phenotypes in ½ MS agar plates that also included partial leaf chlorosis (**Fig. 1A**). However, in the sterile peat matrix of the gnotobiotic Flowpot system (Kremer *et al.*, 2021) or natural, non-sterile Cologne agricultural soil (CAS), R401 inoculation did not result in any changes to pigmentation and shoot fresh weight (**Fig. 1B** & **C**). Salt stress has been shown to facilitate the detrimental effects of *Pseudomonas* strains on tomato (*Solanum lycopersicum*, Solanaceae) and cucumber (*Cucumis sativus*, Cucurbitaceae) plants (Chojak-Koźniewska *et al.*, 2017; Dimartino, 2011). We therefore speculated that salt stress may also facilitate the detrimental effects of *Pseudomonas brassicacearum* R401 on *A. thaliana* (Brassicaceae). In axenic conditions (**Fig. 1B**) and in the presence of a complex, natural microbiota (**Fig. 1C**), the application of 100 mM NaCl negatively affected plant growth (HK 0 mM NaCl vs. HK 100 mM NaCl; $p < 0.001$ for both **Fig. 1B** & **C**; Kruskal-Wallis followed by Dunn's post-hoc test). Co-inoculation of R401 and 100 mM NaCl further aggravated this effect, leading to highly stunted plants and leaf chlorosis in shoots of seedlings grown in either soil matrix, reminiscent of R401s effects in ½ MS agar plates (**Fig. 1A–C**). While root phenotypes cannot be robustly quantified from soil isolated roots, it is very likely that root growth was also severely altered under these conditions. Collectively, this indicates that in natural systems, the opportunistic pathogen R401 requires favourable environmental conditions to cause disease symptoms on *A. thaliana.*

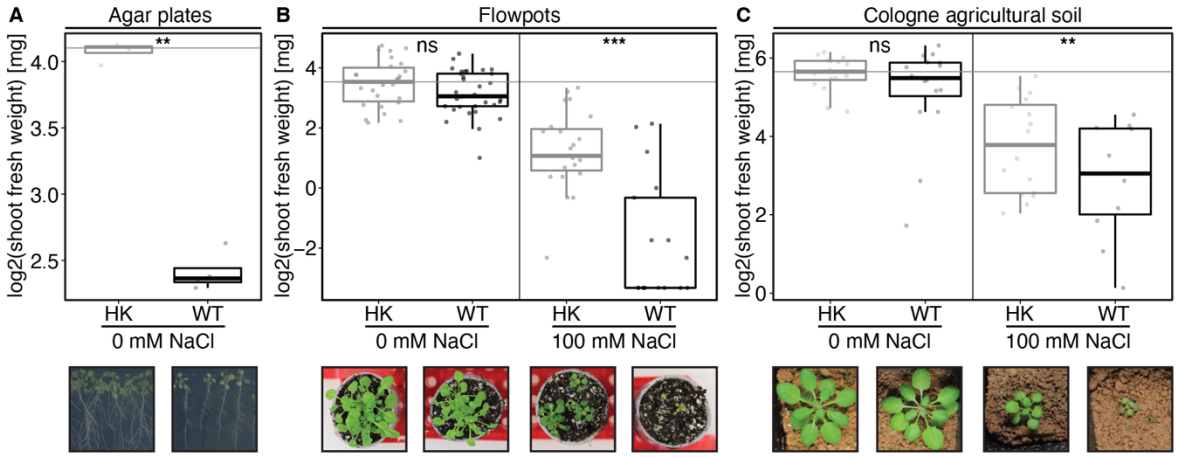

Figure 1, Detrimental activity of *Pseudomonas brassicacearum* R401 is facilitated by salt stress in soil. **(A)** log2-transformed shoot fresh weight of *A. thaliana* plants grown axenically on ½ MS agar plates for 19 dpi. At 14 dpi plants were flushed with either heat-killed (HK) or live wild-type (WT) R401 cells. Five minutes after flushing plants were transferred to new sterile plates and grown for five days (n=5). **(B)** log2-transformed shoot fresh weight of *A. thaliana* plants grown in the gnotobiotic Flowpot system for 28 dpi in the presence or absence of 100 mM NaCl and either heat-killed (HK) or live wild-type (WT) R401 cells (n=30). **(C)** log2-transformed shoot fresh weight of *A. thaliana* plants grown in the non-sterile Cologne agricultural soil (CAS) in the greenhouse for 28 dpi in the presence or absence of 100 mM NaCl and either heat-killed (HK) or live wild-type (WT) R401 cells (n=16). **(A – C)** Representative images illustrating the respective plant phenotypes are shown below each plot. Within each figure panel, all images are to scale. Statistical significance was determined by Kruskal-Wallis followed by Dunn's post-hoc test and Benjamini-Hochberg adjustment. Significance compared to HK is indicated by black asterisks (** and *** indicate $p < 0.01$, and 0.001, respectively; ns, not significant). Statistical comparisons were conducted between WT and HK samples for each NaCl treatment separately.

II.4.2 R401 inoculation results in root- and salt stress-specific transcriptional reprogramming

We hypothesized that the salt stress response of *A. thaliana* may come at the cost of dampening immunity sectors which may in turn facilitate R401 virulence. We therefore sequenced the shoot and root transcriptome of 28-day-old *A. thaliana* seedlings grown in the Flowpot system and inoculated with either heat-killed (HK) or live R401 wild-type (WT) cells and either 0 or 100 mM NaCl (plants from **Fig. 1B**). Inoculation of live R401 cells in the absence of salt stress exerted only minor effects on both root and shoot transcriptomes, with only 2 and 14 significantly differentially enriched genes (DEGs), respectively. Salt stress caused differential expression of 85 and 1,162 genes in roots and shoots, respectively, indicating only minor transcriptional reprogramming in roots (**Fig. 2A** and **Fig. S1A** & **B**). Based on PANTHER functional annotation analyses, all upregulated genes in roots can be categorized into the three GO-terms 'response to abscisic acid', 'response to osmotic stress', and 'response to water deprivation', while in shoots the among the most enriched GO-terms were 'anthocyanin-containing compound biosynthetic process', 'hyperosmotic salinity response' and 'abscisic

acid-activated signalling pathway' (Carbon *et al.*, 2017; Mi, Muruganujan, Ebert, *et al.*, 2019; Mi, Muruganujan, Huang, *et al.*, 2019). Furthermore, gene clusters 8 and 7 were primarily expressed in shoots and involved in photosynthesis and starch metabolism, respectively. Gene clusters 8 and 7 were severely down- and upregulated by salt stress, respectively (**Fig. 2A**). Collectively, these data confirm that salt stress as applied in our experimental setup indeed activates the salt stress response and interferes with plant photosynthesis as reported before (Chaves *et al.*, 2009; Eynard *et al.*, 2008; Geng *et al.*, 2013; Hanin *et al.*, 2016). Co-inoculating live R401 and 100 mM NaCl had the most severe effects on the transcriptomic response in shoots and roots with 2,611 and 2,069 DEGs in roots and shoots, respectively (**Fig. 2A** and **Fig. S1A** & **B**). However, only in roots did R401 cause major additive transcriptional reprogramming compared to NaCl alone, with 1,922 DEGs (**Fig. 2A)**. Here, gene clusters 3 and 5 were specifically downregulated in response to R401 in roots. The genes in these clusters are implicated in 'cellular response to hypoxia' and 'regulation of multicellular organismal development', indicating an activated response to oxidative stress and decreased root development, respectively (**Fig. 2A**). Surprisingly, R401 does not proliferate to higher bacterial titres in the presence of salt stress in either shoots or roots and does not show increased proliferation in roots (**Fig. S1C**). This indicates that bacterial abundance does not explain the striking difference in the salt stress-dependent, R401-induced transcriptional reprogramming between shoots and roots. Collectively, R401 only causes transcriptomic responses in *A. thaliana* roots in the presence of hyperosmotic NaCl concentrations, while shoot transcriptomes are barely affected by the combinatorial treatment, indicating a root-specific virulence phenotype of R401.

Functional annotation analysis of all genes that were significantly up- or down-regulated by salt stress or combinatorial treatment of salt stress and R401 revealed 14 GO-term clusters with involvement in primary metabolism (*e.g.*, 'photosynthesis' and 'response to carbohydrate') or biotic (*e.g.*, 'immune system process' and 'regulation of response to biotic stimulus') and abiotic stress (*e.g.*, 'response to abiotic stimulus' and 'cellular response to abscisic acid stimulus'; **Fig. 2B**). While primary metabolism and the response to abiotic stress was dynamically regulated, the biggest cluster, with involvement in the biotic stress response, was solely downregulated. Decreased expression of immunity genes, however, was shoot-specific. Namely, genes with involvement in the functional categories 'systemic acquired resistance', 'response to molecule of bacterial origin' and 'regulation of jasmonic acid mediated signalling pathway' were downregulated, indicating a shoot-specific suppression of the two major immunity sectors.

Next, we tested whether salt stress-mediated suppression of immune system functions in shoots may facilitate virulence of other opportunistic pathogens, such as *Streptomyces sp.* R107 and *Xanthomonas sp.* L131 (Ma *et al.*, 2021; Pfeilmeier *et al.*, 2021). L131 virulence on *A. thaliana* leaves depends on the NADPH-dependent respiratory burst oxidase homologue D (RBOHD), which was approx. 51-fold downregulated by salt stress in shoots (*p.adj* <0.05, **Table S6**); therefore, it is plausible that salt stress enhances L131 virulence (Pfeilmeier *et al.*, 2021). In the absence of salt stress, R401 and L131 did not show any effect on *A. thaliana* shoot fresh weight, while R107 already significantly impaired plant growth. As described above, R401 only became detrimental upon salt stress treatment. Similarly, however, to a lesser extent, R107 became more detrimental in salt-stressed plants. By contrast, L131 inoculation did not affect shoot fresh weight, even in salt stress conditions (**Fig. S2A**). In a *rbohD* mutant, however, L131 was able to cause disease, while the effect of R401 on shoot fresh weight in this mutant was the same as for the Col-0 wild type. Collectively, this does not provide evidence for immune system-dependent virulence facilitation of opportunistic pathogens by salt stress *per se*.

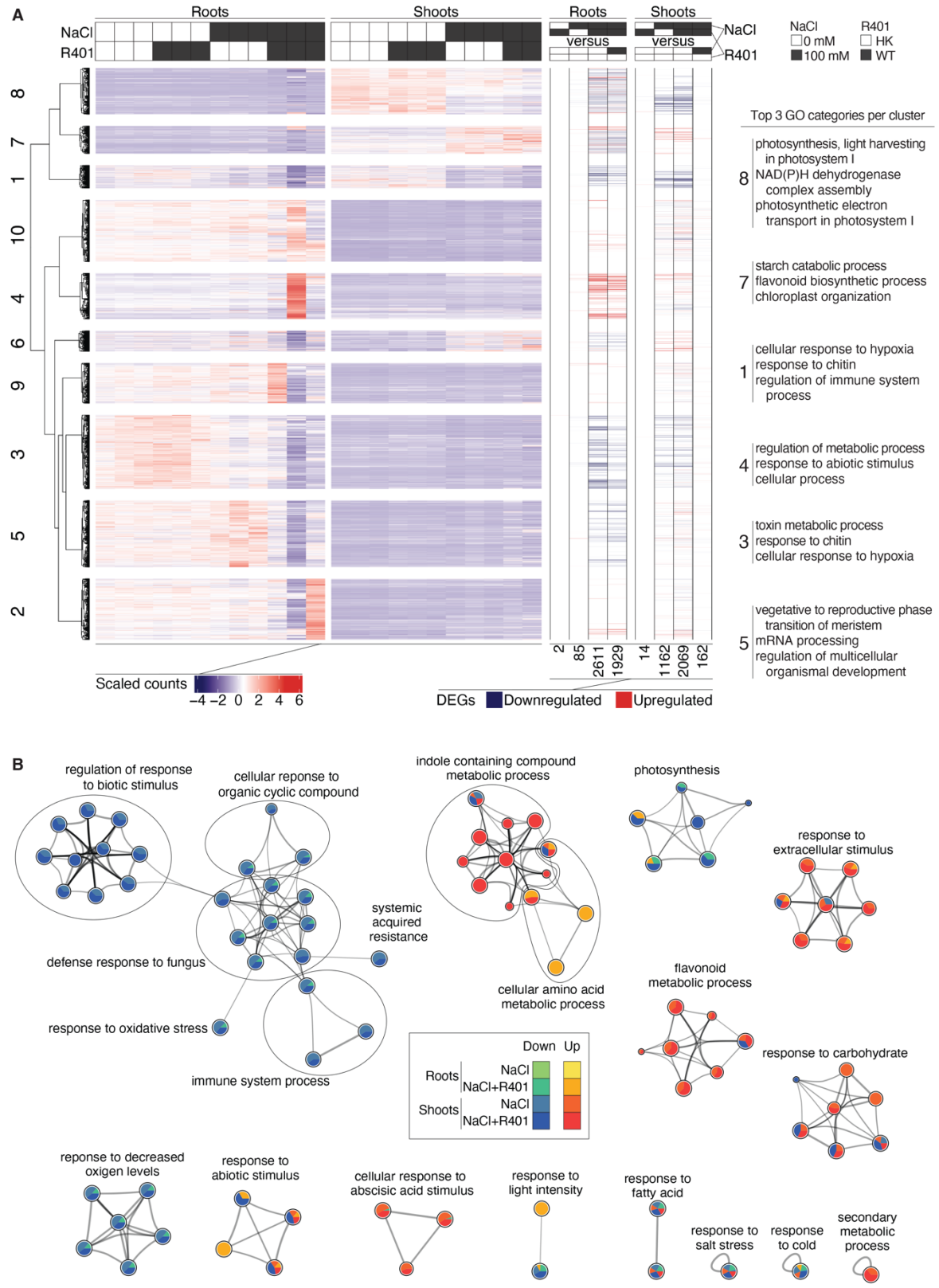

Figure 2, R401 inoculation results in root- and salt stress-specific transcriptional reprogramming. (A) Transcriptomic analysis of *A. thaliana* shoots and roots grown in the gnotobiotic Flowpot system for 28 dpi in the presence or absence of 100 mM NaCl and either heat-killed (HK) or live wild-type (WT) R401 cells (n=3; one sample was removed from the analysis due to extensive contamination with *Salmo trutta*). Heat map (centre) of scaled normalized read counts, clustered by k-means (k=10, left) and differentially enriched genes (DEGs, right) obtained by pairwise comparison. The three most significantly enriched GO terms, as computed by PANTHER

GO term enrichment analysis (Mi, Muruganujan, Ebert, *et al.*, 2019), are depicted for selected clusters (right) that showed R401- and/or NaCl-specific patterns. DEGs were considered significantly up- or downregulated if *p.adj* < 0.05 and $\log_2$(foldchange) > 1 or < -1, respectively. **(B)** Network of significantly enriched GO terms with NaCl or NaCl + R401-treated shoots and roots. All significantly up- and downregulated genes as compared to control conditions (0 mM NaCl + HK R401) were selected for the analysis. GO term enrichment analysis and clustering was performed by Metascape (Zhou *et al.*, 2019). Unfilled circles indicate subclusters.

II.4.3 Brassicapeptin production is required for detrimental activity of R401

Pseudomonas strains employ diverse effector proteins that are often directly injected into plant cells *via* the bacterial type III secretion system (T3SS), thereby promoting bacterial infection through suppression of immune signalling and defence responses (Cunnac *et al.*, 2009; Guo *et al.*, 2009; Wagner *et al.*, 2018). Using nucleotide BLAST, we aimed to determine whether the R401 genome encodes a T3SS that could explain the virulence mechanism of R401. However, we did not identify a single T3SS component (Altschul *et al.*, 1990). Therefore, we hypothesized that R401 might use secondary metabolites as virulence factors. antiSMASH-based prediction of BGCs revealed a >140 kb BGC with high similarity to the *syp-syr* BGC of *Pseudomonas syringae* B728a involved in Syringopeptin and Syringomycin biosynthesis (**Fig. 3A**; Blin *et al.*, 2021; Feil *et al.*, 2005). Syringopeptin and Syringomycin have been demonstrated to be required for virulence of *syp-syr*-encoding *Pseudomonas syringae* strains (Scholz-Schroeder *et al.*, 2001). R401 has been phylogenetically assigned to the *Pseudomonas brassicacearum* species (**Chapter I**); therefore, we termed the putatively produced secondary metabolites 'Brassicapeptin' and 'Brassicamycin'. To test whether the *syp-syr* BGC contributes to R401 virulence on *A. thaliana* under salt stress, we generated a marker-free knockout mutant (Δ*sypc*) lacking *sypC*, one of the core biosynthetic genes putatively involved in Brassicapeptin biosynthesis. We then tested whether this mutant retained its detrimental activity in the context of salt stress and assessed whether salt stress quantitively facilitates R401 virulence. Therefore, we inoculated heat-killed (HK) or live R401 wild type (WT) or Δ*sypc* mutant cells into the gnotobiotic Flowpot system across a gradient of NaCl concentrations (0–150 mM NaCl). R401 WT was again able to cause disease on NaCl-treated plants and the effect was NaCl-concentration dependent (**Fig. 3B**). Indeed, the detrimental effect of R401 WT was exacerbated by increasing NaCl concentrations, indicating a dose-dependent relationship between NaCl concentrations and R401 virulence (**Fig. 3C**). Remarkably, the detrimental effect of R401 on salt-treated plants was fully abolished in the Δ*sypc* mutant, which was even able to partly rescue the salt stress-induced negative effects on plant growth (**Fig. 3B**). Therefore, mutation of a single bacterial gene involved in the production of a secondary metabolite was sufficient to turn

a pathogen into a beneficial plant growth promoting isolate under salt stress. This also confirms that Brassicapeptin is a key virulence factor of R401.

These results prompted us to test whether the detrimental activity of R401 may also be observable with other abiotic stresses, such as drought stress or low photosynthetically active radiation (low PAR; Hou *et al.*, 2021). While low PAR treatment, as induced by shading, had more severe effects on shoot fresh weight compared to drought treatment, this treatment was not observed to facilitate R401-induced detrimental activity. In contrast, drought stress mimicked by the application of 5% polyethylene glycol (PEG8000) promotes R401 virulence, demonstrating that the detrimental activity of R401 is potentiated by hyperosmotic stress (**Fig. S3A**). Next, we assessed whether R401 salt stress-dependent virulence is limited to *A. thaliana*. R401 and salt stress treatment of *Solanum lycopersicum cv.* Micro-Tom (Micro-Tom) revealed virulence of R401 WT only in salt-stressed seedlings, which was also abolished in the Δ*sypc* mutant. For *Lotus japonicus* Gifu (Gifu), no detrimental activity of R401 WT could be observed either in the presence or absence of NaCl treatment; however, Gifu also showed no sensitivity to the salt stress *per se* (**Fig. S3B** and **C**). We harvested shoots and roots from both Micro-Tom and Gifu seedlings to quantify the colonisation capability of R401 WT and the Δ*sypc* mutant in the presence or absence of salt treatment. While colonisation of the WT was in general comparable between all tested conditions, Δ*sypc* colonized Micro-Tom roots significantly less efficiently only upon salt stress treatment, which was not observed in salt-resistant Gifu plants (**Fig. S3D** and **E**). In axenic liquid medium, growth of R401 WT and Δ*sypc* was identical irrespective of the NaCl concentration (**Fig. 3D**), demonstrating that R401 *per se* is not sensitive to 100 mM NaCl, that mutation of sypc does not affect bacterial growth *in vitro*, and that the reduced proliferation of Δ*sypc* on tomato roots is root specific.

Collectively, these data demonstrate the requirement of Brassicapeptin for R401 virulence on both *Arabidopsis* and Micro-Tom, irrespective of the 112 million years of reproductive isolation between these plants and suggests a compartment- and environment-specific functioning of Brassicapeptin in R401 root competence in salt-stressed plants.

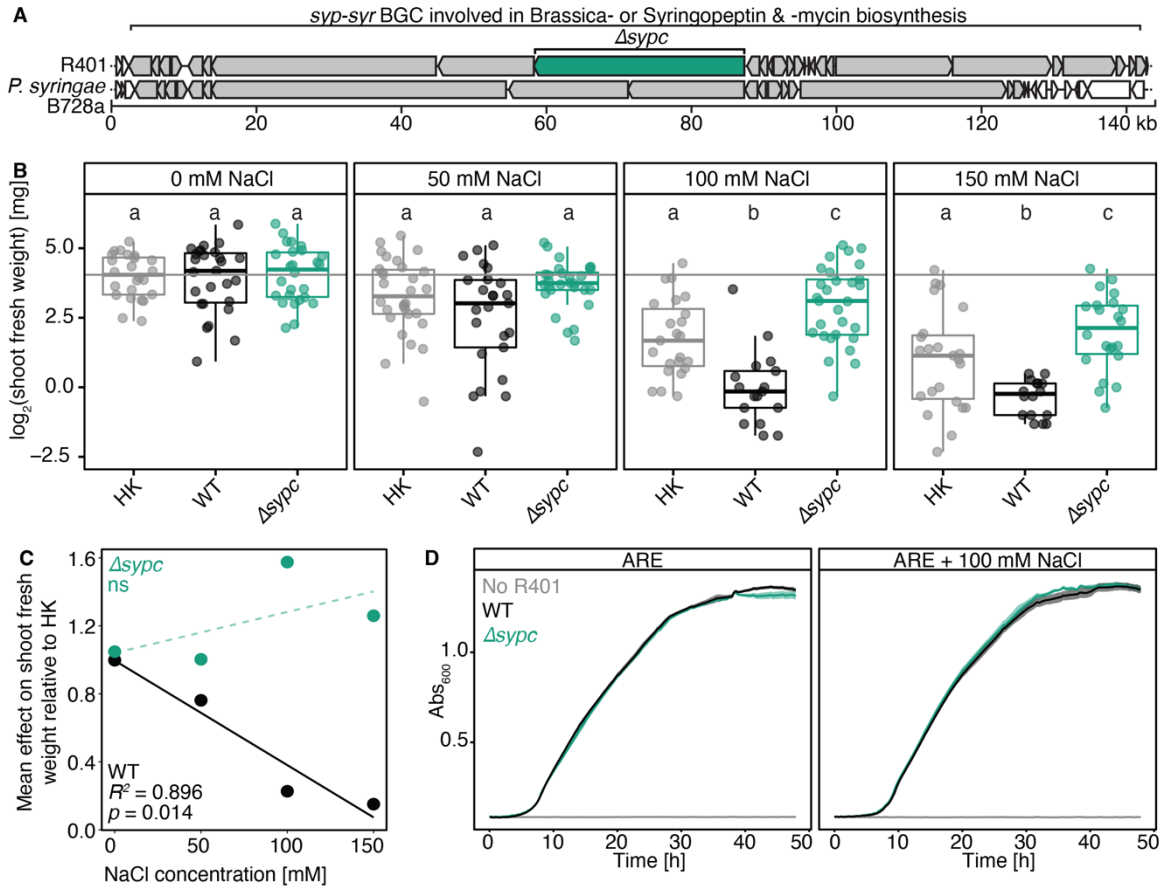

Figure 3, Brassicapeptin production is required for R401 detrimental activity. (A) Schematic overview of the genomic context of the *syp-syr*-operon which encodes genes for Syringopeptin and Syringomycin biosynthesis in *Pseudomonas syringae* B728a and likely for related secondary metabolites in *Pseudomonas brassicacearum* R401, thereby termed 'Brassicapeptin' and 'Brassicamycin'. Genes within the biosynthetic gene cluster (BGC) are coloured in grey, R401 *sypc* is highlighted in green. *sypc* is likely involved in Brassicapeptin biosynthesis in R401. A Δ*sypc* knockout mutant has been generated in R401, lacking the full-length *sypc* coding region. **(B)** log2-transformed shoot fresh weight of *A. thaliana* plants grown in the gnotobiotic Flowpot system for 28 dpi in the presence of increasing concentrations of NaCl (0, 50, 100, or 150 mM NaCl) and either heat-killed (HK), live wild-type (WT) or live Δ*sypc* R401 cells. Letters indicate statistically significant differences as determined by Kruskal-Wallis followed by Dunn's post-hoc test and Benjamini-Hochberg adjustment with $p < 0.05$ (n=30). Statistical comparisons were conducted for each salt treatment separately. **(C)** Correlation analysis of the mean effect of either R401 WT or Δ*sypc* on *A. thaliana* shoot fresh weight, normalized by the respective HK control and the applied salt concentrations. Data derives from **(B)**. *p*-values and R^2 derive from a linear model; ns, not significant. **(D)** Growth curves of R401 WT and Δ*sypc* mutant in artificial root exudate (ARE) liquid medium or ARE medium supplemented with 100 mM NaCl; n=10.

II.4.4 Isolation and structural characterization of R401 Brassicapeptin

Next, we aimed at isolating and structurally characterising R401 Brassicapeptin and cultivated 70 l of axenically grown R401, which yielded 16.24 g of crude extract after EtOAc extraction. The crude extract was subjected to chromatographic purification, using reversed phase flash, followed by semipreparative high-performance liquid chromatography (HPLC) to yield Brassicapeptin A and B. Both molecules were obtained as white amorphous powders and

subjected to mass spectrometric (MS) analysis. Using HR-ESI-MS we characterised the partial amino acid sequences for Brassicapeptin A and B. The HR-ESI-MS spectrum of Brassicapeptin A showed a double-charged base peak ion $[M+2H]^{2+}$ at m/z 1027.1080, in agreement with the molecular weight of 2052.2004, which was supported by the tribble-charged base peak ion $[M+3H]^{3+}$ at m/z 685.0747, suggesting a molecular formula of $C_{96}H_{161}N_{23}O_{26}$ (**Fig. 4A**). For Brassicapeptin B, the HR-ESI-MS spectrum showed a double-charged base peak ion $[M+2H]^{2+}$ at m/z 1005.1033 together with a tribble-charged base peak ion $[M+3H]^{3+}$ at m/z 683.0612, suggesting a molecular formula of $C_{94}H_{157}N_{23}O_{26}$ (**Fig. 4B**). Comparison of the HR-ESI-MS/MS fragments of Brassicapeptin A and B revealed the high similarity from b_1 to b_7 and from y_1-y_{10} except for the differences from b_7 to b_{10} and from y_{11}-y_{13}. The partial sequences of Brassicapeptin A and B were identified from the HR-ESI-MS/MS fragments as -Ala-Leu/Ile-Ala-Val-Leu/Ile-Dhb-Hse-Val-Leu/Ile-Dha-Ala-Ala-Ala-Thr-Dhb- and -Ala-Leu/Ile-Ala-Val-Leu/Ile-Dhb-Gly-Val-Leu/Ile-Dha-Ala-Ala-Ala-Thr-Dhb-, respectively. Next, we performed nuclear magnetic resonance (NMR)-based analysis of the purified compounds to resolve the stereochemistry of Leu/Ile in Brassicapeptin A and B and fully resolve their structure. The ^{1}H NMR and HSQC spectrum displayed 24 amide protons resonated from δ_H 7.38 to δ_H 9.37 and 18 α protons resonated from δ_H 7.38 to δ_H 9.37. A correlation from a methylene group at δ_H 2.85 and 2.77 to amide protons at δ_H 7.68 (4H, overlapped) from the ^{1}H-^{1}H Correlated Spectroscopy (COSY) spectrum indicated a terminal amide group (Dab-γ) belongs to a diaminobutyric acid (Dab) residue, which can also be confirmed by Total Correlation Spectroscopy (TOCSY) correlation from Dab-NH (δ_H 9.19) to Dab-α (δ_H 3.82), Dab-β (δ_H 2.32 and 2.02), Dab-γ, and Dab-NH_2. A dehydroalanine (Dha) residue was assigned based on the Heteronuclear Multiple Bond Correlation (HMBC) correlations from Dha-β (δ_H 5.97 and 5.52) to Dha-α (δ_C 135.32) and Dha carbonyl (δ_C 163.75). Three 2,3-dehydroaminobutyric acid (Dhb) residues were assigned based on COSY correlations between Dhb-β (δ_H 6.35)/Dhb-γ (δ_H 1.61), Dhb-β (δ_H 6.25)/Dhb-γ (δ_H 1.67), and Dhb-β (δ_H 6.07)/Dhb-γ (δ_H 1.66), as well as HMBC correlations from Dhb-β (δ_H 6.35) to Dhb-α (δ_C 130.47) and Dhb carbonyl (δ_C 164.11), from Dhb-γ (δ_H 1.61) to Dhb-β (δ_C 127.82) and Dhb-α (δ_C 130.47), from Dhb-β (δ_H 6.25) to Dhb-α (δ_C 130.89) and Dhb carbonyl (δ_C 164.15), from Dhb-γ (δ_H 1.67) to Dhb-β (δ_C 127.02) and Dhb-α (δ_C 130.89), from Dhb-β (δ_H 6.07) to Dhb-α (δ_C 131.51) and Dhb carbonyl (δ_C 165.193), and from Dhb-γ (δ_H 1.66) to Dhb-β (δ_C 124.14) and Dhb-α (δ_C 131.51; **Fig. S4**). These spectroscopic features suggested that Brassicapeptin A contains 22 amino acid residues. The structure of a fatty acid chain was determined by COSY, Heteronuclear Single Quantum Coherence (HSQC) and HMBC NMR correlations, which is six carbons in length including a carbonyl group, it

was assigned to be linked with a Dhb residue (Dhb_1) based on COSY and TOCSY, HMBC and Rotating-frame Nuclear Overhauser Effect Spectroscopy (ROESY) correlations (**Fig. S4**). Dhb_1 residue was further supported to be linked with an Ala residue (Ala_2) from the 2D NMR data. Thus, a FA-Dhb_1-Ala_2- part was elucidated, which can also be supported by the MS/MS fragment b_1 ($[C_{13}H_{21}N_2O_3]^+$ detected at *m/z* 253.1547, calculated 253.1552). The four Leu or Ile residues were assigned to be one Leu residue (Leu_4) and three Ile residues (Ile_7, Ile_{11} and Ile_{22}) from the 2D NMR data. Another partial amino acid sequence (Thr_{18}-Ala_{19}-Dab_{20}-Ser_{21}-Ile_{22}) was also determined based on 2D NMR data. The above data indicated that the amino acid sequence of Brassicapeptin A was Dhb_1-Ala_2-Ala_3-Leu_4-Ala_5-Val_6-Ile_7-Dhb_8-Hse_9-Val_{10}-Ile_{11}-Dha_{12}-Ala_{13}-Ala_{14}-Ala_{15}-Thr_{16}-Dhb_{17}-Thr_{18}-Ala_{19}-Dab_{20}-Ser_{21}-Ile_{22}. The cyclization between Thr_{17} and Ile_{22} was determined based on HMBC and ROESY data (**Fig. S4**). Brassicapeptin A and B differ only based on a substitution of Hse_9 to Gly_9, in Brassicapeptin A and B, respectively. Collectively, the complete planar structure of R401 Brassicapeptin was elucidated using a combinatorial approach of MS and NMR (**Fig. 4C**).

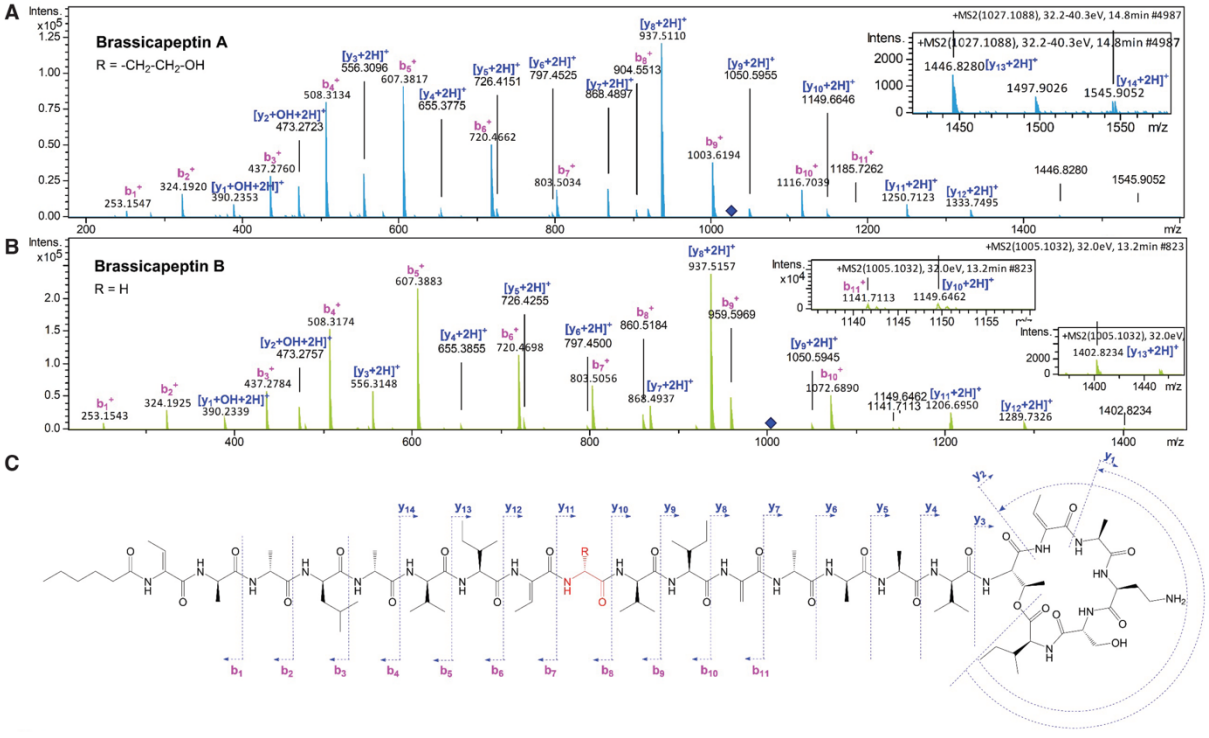

Figure 4, Structure elucidation of R401 Brassicapeptin A and B. (A, B) HR-ESI-MS/MS fragments of Brassicapeptin A **(A)** and B **(B)**. **(C)** Chemical structures of Brassicapeptin A and B detected from ESI-MS/MS fragmentations and nuclear magnetic resonance (NMR) analysis. The sidechain at position 9 of Brassicapeptin A and B is indicated in red in **(A)** and **(B)**, respectively.

II.4.5 Interaction of Brassicapeptin A with NaCl is sufficient for R401 detrimental activity

Syringopeptins have been demonstrated to have antagonistic activity against species in different kingdoms of life, and R401 has previously been described to be highly antagonistic towards bacteria (**Chapter I**). Therefore, we first tested whether Brassicapeptin also contributes to the antibacterial activity of R401. We generated higher-order mutants lacking pyoverdine and 2,4-Diacetylphlorogucinol (DAPG) BGCs, as these have been described to contribute most to R401 inhibitory activity (**Chapter I**, **Fig. S5A**). We tested a taxonomically diverse set of bacteria, including Actinobacteria, Flavobacteriia, Bacilli and Alpha-, Beta-, and Gammaproteobacteria. We furthermore included plant-pathogenic *Fusarium oxysporum* F212 to assess putative antifungal activity of Brassicapeptin (Bai *et al.*, 2015; Durán *et al.*, 2018). While most of the R401 inhibitory activity towards bacteria was explained by pyoverdine and DAPG production, Brassicapeptin showed activity against *Streptomyces venezuelae* R431. Furthermore, R401 DAPG, pyoverdine and Brassicapeptin also act additively to inhibit *F. oxysporum* F212 (**Fig. S5B).** We could further confirm the antibacterial activity of Brassicapeptin A in a minimum inhibitory concentration assay. Here, of all tested strains, only *Listeria monocytogenes* DSM20600 (class: Bacilli) was inhibited by R401 Brassicapeptin (**Table S7**). Collectively, these data demonstrate direct inhibitory activity of R401 Brassicapeptin against taxonomically unrelated Gram-positive bacteria and *F. oxysporum* F212.

Next, we assessed the putative phytotoxic activity of Brassicapeptin on *Arabidopsis* plants. Brassicapeptin A was approx. 10x more abundant compared to Brassicapeptin B, therefore, we focused on Brassicapeptin A for all subsequent experiments. We transplanted seven-day-old Arabidopsis seedlings to ½ MS agar plates containing increasing concentrations of purified Brassicapeptin A solubilized in dimethyl sulfoxide (DMSO), in the presence or absence of 100 mM NaCl. After 14 days, Brassicapeptin A showed a dosage-dependent effect on root and shoot growth, demonstrating that Brassicapeptin A is sufficient to reproduce phenotypes on both plant organs that are reminiscent of the effect of R401 WT in agar plates (**Fig. 5 A–C**). The addition of 100 mM NaCl further aggravated this phenotype. Plants grown in the presence of 1 µg/ml Brassicapeptin A and 100 mM NaCl died immediately as seen by bleaching of the leaves and severely inhibited root growth (**Fig. 5B**–**D**). This indicates a direct interaction of Brassicapeptin A and NaCl. Furthermore, Brassicapeptin A was sufficient to induce ion leakage in *A. thaliana* leaf discs after 16 h of incubation. At this timepoint, no cell death was observable, suggesting that Brassicapeptin A might insert into plasma membranes, thereby resulting in uncontrolled ion fluxes (**Fig. 5E**).

Collectively, this indicates that Brassicapeptin A-induced disruption of ion homeostasis, in combination with osmotic pressure in the root environment, are sufficient to explain the detrimental activity of R401 in salt-stressed plants. Given that R401 WT is detrimental on Arabidopsis in an ½ MS agar-based system in the absence of salt stress, we hypothesized that Brassicapeptin A-induced disruption of ion homeostasis would be reduced in a diluted MS medium. Consistent with this hypothesis, inoculation of R401 WT onto 1/10 MS agar plates completely abolished the detrimental effect of R401 that was observed in ½ MS (**Fig. S5C**–**E**). Taken together, our data support the idea that disruption of host membrane integrity is key for R401 proliferation at roots.

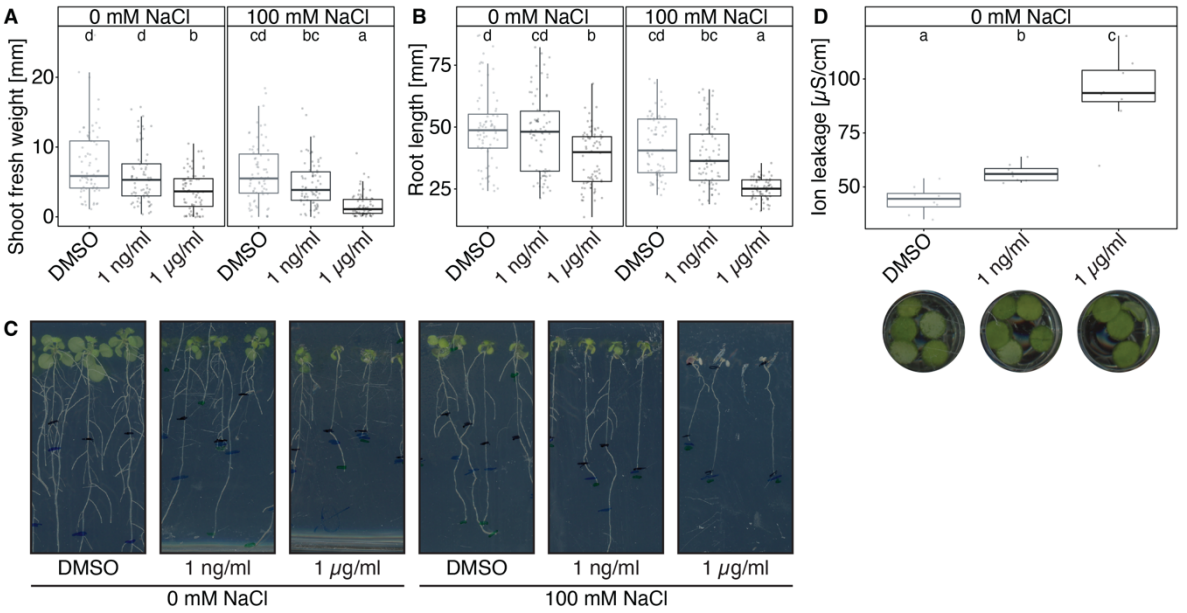

Figure 5, Brassicapeptin A interaction with NaCl is sufficient for R401 detrimental activity. (A–C) Shoot fresh weight **(A)**, root length **(B)** and images of representative phenotypes **(C)** of *A. thaliana* plants grown axenically on ½ MS agar plates supplemented with increasing concentration of Brassicapeptin A and either 0 or 100 mM NaCl (n=72). Sterile *A. thaliana* seeds were pre-germinated on ½ MS agar plates for seven days and then transferred to new plates containing NaCl and/or Brassicapeptin A for another 14 days; black, blue, and green markings in **(C)** indicate root length after seedling transfer or 7 and 14 days of growth, respectively. **(D)** Ion leakage assay of *A. thaliana* leaf discs, 16 h after treatment with increasing concentrations of Brassicapeptin A. Circular images depict exemplary phenotypes, indicating the lack of cell death (n=8). DMSO or Brassicapeptin A was taken up in sterile Milli-Q water. All solutions were measured before the experiment resulting in measurements of 2 µS/cm. **(A–D)** Brassicapeptin was solubilized in DMSO. Concentrations in red indicate final Brassicapeptin A concentrations in the agar or Milli-Q water. **(A, B, D)** Letters indicate statistically significant differences as determined by Kruskal-Wallis followed by Dunn's post-hoc test and Benjamini-Hochberg adjustment with $p < 0.05$. Statistical comparisons were conducted for each salt treatment separately.

II.5 Discussion

After 28 days of chronic salt treatment, the response of *A. thaliana* to salt stress was largely shoot-specific with photosynthesis-related genes being heavily downregulated, likely due to accumulation of Cl^- and Na^+ ions in leaves, causing imbalances in ion homeostasis and disruption of the photosynthetic machinery (Acosta-Motos *et al.*, 2017; Ashraf & Harris, 2004; Chaves *et al.*, 2009). The induction of genes involved in starch catabolism is likely to be a mechanism employed by plants to compensate for the disruptions to photosynthesis (**Fig. 2A**). In roots, transcriptomic responses are activated immediately after salt stress sensing before gradually declining in intensity, explaining the only minor transcriptomic differences after 28 days of continuous salt stress (**Fig. 2A** and **Fig. S1A;** Geng *et al.*, 2013). The effect of R401 in the absence of salt stress was minor in both shoots and roots, while in the presence of hyperosmotic NaCl concentrations live R401 cells induced highly plastic root-specific transcriptional changes (**Fig. 2A**), indicating that R401s detrimental effect occurs primarily *via* roots. However, only in shoots, genes involved in different sectors of the plant innate immune system were significantly down regulated due to NaCl treatment (**Fig. 2A** and **B**). Low PAR treatment dampens salicylic- and jasmonic acid-dependent immunity sectors in *A. thaliana* roots and shoots and has been shown to facilitate virulence of *Botrytis cinerea* and *Pseudomonas syringae pv. tomato* DC3000 (Hou *et al.*, 2021). However, R401 did not cause disease under such conditions (**Fig. S3A**). Collectively, this indicates a minor involvement of plant immunity in potentiating R401 virulence, which is corroborated by the absence of disease symptoms of R401 in an immunocompromised *rbohD* mutant (**Fig. S2B**). To fully rule out a contribution of NaCl-mediated suppression of immunity in facilitating R401 virulence, we propose testing R401 virulence in mutants impaired in root-specific immunity sectors, such as mutants lacking the transcription factor MYB15, which has been shown before to facilitate R401 virulence in agar-based systems (Ma *et al.*, 2021). Furthermore, the application of ABA should mimic salt stress-induced transcriptional reprogramming, without inducing NaCl or osmotic stress directly. This could further help to characterize the contribution of immune functions in R401-mediated disease under salt stress.

R401 encodes a 140 kb BGC that is responsible for the production of the non-ribosomal peptides Brassicapeptin A and B (**Fig. 3A** and **4**). A R401 mutant lacking *sypC*, one of the core biosynthetic genes, lost its ability to cause disease *in planta*, demonstrating a requirement of Brassicapeptin production for the detrimental activity of R401s in salt-stressed plants (**Fig. 3B**). Various structurally related compounds have been previously demonstrated to possess toxic

activity against various forms of life including bacteria, fungi, and plants (Bensaci & Takemoto, 2007; Grgurina *et al.*, 2005; Hutchison & Gross, 1997; Melnyk *et al.*, 2019; Scholz-Schroeder *et al.*, 2001; Weeraratne *et al.*, 2020). R401 Brassicapeptin seems to fulfil dual functions in plant disease and competitive microbe-microbe interactions (**Fig. 3B, Fig. 5B**–**D** and **Fig. S5B**). Structurally related compounds have been demonstrated to intercalate plasma membranes thereby destabilizing them and causing pore formation that disrupts cell integrity, eventually leading to uncontrolled diffusion of cell solutes and the surrounding medium (Dalla Serra *et al.*, 1999; Grgurina *et al.*, 2005; Hutchison & Gross, 1997). We observed leakage of cellular solutes from *A. thaliana* leaf discs that have been treated with Brassicapeptin A (**Fig. 5E**), corroborating the assumption that Brassicapeptin inserts into plant plasma membranes. R401 showed *sypC*-dependent virulence only under salt and drought stress, confirming that hyperosmotic conditions and Brassicapeptin are required for R401 virulence (**Fig. 3B** and **Fig. S3A**). This is supported by a linear dose-response relationship between applied NaCl concentrations and the virulence of R401 (**Fig. 3C**). In ½ MS agar plates, R401 Brassicapeptin A was sufficient to negatively impact shoot and root phenotypes in the absence of salt stress, while this was aggravated by the addition of 100 mM NaCl to the culture medium (**Fig. 5B**–**D**). This suggests that the nutrient concentrations in ½ MS agar medium are sufficient to impose hyperosmotic stress on plants. A 5-fold reduction in MS medium concentrations was likewise able to abolish the detrimental activity of R401 (**Fig. S5C–E**). Collectively, this demonstrates that the direct interaction of a bacterial secondary metabolite with pore-forming capabilities and favourable environmental conditions is sufficient to explain R401 detrimental activity on *A. thaliana* and likely other salt- and osmotic stress-sensitive plants. The lack of a plant transcriptomic response in the presence of Brassicapeptin A-producing R401 wild type in control conditions further supports the conditional bioactivity of Brassicapeptin in the rhizosphere. Root-specific transcriptional reprogramming to R401 and NaCl treatment and root (**Fig. 2A**) and NaCl-specific benefits of Brassicapeptin production on R401 proliferation, likely *via* nutrient leaching from the root endosphere due to hyperosmotic pressure (**Fig. S3D**), further indicate a root-specific interaction of NaCl and Brassicapeptin. While R401 likely fulfils extensive biocontrol activities due to its diverse repertoire of antibacterial and antifungal secondary exometabolites (**Chapter I** and **Fig. S5B**), favourable abiotic conditions allow for disease development by Brassicapeptin-producing R401.

R401, R131 and R107 have been isolated from healthy *A. thaliana* plants; however, under favourable conditions they can become detrimental to plant health – in the case of R401 even in the context of natural microbial communities (**Fig. 1C**; Bai *et al.*, 2015). Groundwater-

derived *Pseudomonas sp.* N2C3 (N2C3) also contains the *syp-syr* BGC and has been demonstrated to cause *syp*-dependent stunting of *A. thaliana* root and shoot growth in ½ MS agar medium (Melnyk *et al.*, 2019). In natural soil, N2C3 does not cause any detrimental phenotypes, even after inoculation of high bacterial titres (1 x 10^6 cells per gram soil; Song *et al.*, 2021), a phenotype that is reminiscent of the herein described effects of R401. Using computational analyses, convergent gain, and loss of the *syp-syr* BGC has been demonstrated for the *Pseudomonas fluorescence*-clade, which comprises *P. brassicacearum* (Melnyk *et al.*, 2019). Loss of *sypC* in R401 was sufficient to turn the detrimental strain into a growth-promoting strain (**Fig. 3B**), while the mechanisms of growth promotion of Δ*sypc* R401 remain elusive. Collectively, this corroborates regular transfer of genomic elements and suggests that the acquisition of the *syp-syr* BGC can overwrite the growth-promoting activities of R401 Δ*sypc* under salt stress.

High soil salinity is one of the main constraints for agricultural performance worldwide and arises through frequent irrigation and fertilisation, which results in the accumulation of nutrient salts in agricultural soils. This accumulation will become more problematic due to an increasing demand for field irrigation owing to climate change (Corwin, 2021; Eswar *et al.*, 2021; Eynard *et al.*, 2008; Hanin *et al.*, 2016; Mukhopadhyay *et al.*, 2021). Our data show disease susceptibility in the model plant *A. thaliana* and the crop plant *Solanum lycopersicum*; however, salt-insensitive *Lotus japonicus* was unaffected by Brassicapeptin. This demonstrates the necessity for salt-resistant cultivars to not only overcome salt stress *per se* but also facilitation of opportunistic pathogens, as demonstrated herein. It is plausible that membrane-intercalating exometabolites outside of the genus *Pseudomonas*, such as Surfractin produced by *Bacillus spp.* may cause similar detrimental activity to R401 Brassicapeptin A (Bionda *et al.*, 2013; Kuiper *et al.*, 2004; Neu *et al.*, 1990; Nielsen *et al.*, 2000; Peypoux *et al.*, 1999; Raaijmakers *et al.*, 2010). Taken together, our data provides a mechanistic explanation for the emergence of bacterial plant disease under abiotic conditions and define an ecological framework for the detrimental activity of R401 and likely other *Pseudomonas spp.* isolates.

II.6 Material and methods

II.6.1 Data and script availability

All data and code generated for this study will be deposited on public databases upon publication of this chapter in a scientific journal. All primers used in this study can be found in **Table S8**.

II.6.2 Biological material and culture conditions

Microorganisms

The bacterial and fungal strains used in this study have been initially isolated from unplanted soil, *A. thaliana* roots or shoots (Bai *et al.*, 2015; Durán *et al.*, 2018) and are summarized in **Table S9.** The R401 Δ*sypc* mutant has been deposited in the bacterial culture collection of the Department of Plant Microbe Interactions at the Max Planck Institute for Plant Breeding Research in Cologne, Germany, and are available upon request from Stéphane Hacquard (hacquard@mpipz.mpg.de).

Plant species

Arabidopsis thaliana ecotype Columbia-0 (Col-0), *Lotus japonicus* ecotype Gifu B-129, and *Solanum lycopersicum cv.* Micro-Tom were used as wild-types. *A. thaliana rbohd* contains a *dSpm* transposon in the fifth exon of *AtrbohD* (AT5G47910; Torres *et al.*, 2002).

Microbial culture conditions

Bacteria were streaked from glycerol stocks (25% glycerol) on TSA plates (15 g/l Tryptic Soy Broth, Sigma Aldrich; with 10g/l Bacto Agar, Duchefa Biochemie) and grown at 25 °C. Single colonies were inoculated into liquid 50% TSB (15 g/l Tryptic Soy broth, Sigma Aldrich) and grown until dense at 25 °C with 180 rpm agitation. Dense cultures were then stored at 4 °C and diluted 1 to 10 in TSB the day before the experiment and cultured at 25 °C with 180 rpm agitation overnight to ensure sufficient cell densities for slow- and rapidly growing bacteria. Glycerol stocks were stored at -80 °C and kept on dry ice when transported. Individual pieces of fungal mycelium were transferred to potato dextrose agar (PDA; Sigma-Aldrich) Petri dishes

from glycerol stocks (approx. 30 pieces of fungal mycelium in 25% sterile glycerol, stored at -80 °C). *F. oxysporum* F212 was grown at 25 °C in the dark for 14 days.

II.6.3 Seed sterilisation

Arabidopsis thaliana and *S. lycopersicum* Micro-Tom seeds were sterilized using 70% ethanol and bleach. Seeds were submerged in 70% ethanol and left shaking at 40 rpm for 14 minutes. Ethanol was removed before the seeds were submerged in 8.3% sodium hypochlorite (Roth) containing 1 µl of Tween 20 (Sigma-Aldrich) and left shaking at 40 rpm for 4 minutes. Under sterile conditions, the seeds were washed 7x times and finally taken up with sterile 10 mM $MgC1_2$. Seeds were left for stratification at 4 °C for 3 days. Seed sterility was confirmed by plating approx. 100 seeds on a 50% TSA plate. The seed coat of *L. japonicus* Gifu seeds was first abraded using sanding paper, then seeds were incubated for 20 min in diluted bleach, followed by five-times washing in sterile water. Sterilized Gifu seeds were pregerminated on sterile, water-soaked whatman paper for 7 days.

II.6.4 Gnotobiotic Flowpot experiments

Peat sterilisation and Flowpot assembly were performed as described before (Chapter I). For Micro-Tom and Gifu, big Flowpots fitting 50 ml soil were used, as described before (Wippel *et al.*, 2021). Microbes were grown and inocula were prepared as described above. Each Flowpot was inoculated with 50 ml half strength Murashige and Skoog medium with vitamins (½ MS; 2.2 g/l, Duchefa Biochemie, 0.5 g/l MES, pH 5.7). For bacteria, a final OD_{600} of 0.0025 in 50 ml ½ MS were inoculated per Flowpot. For salt stress treatment ½ MS contained 50, 100 or 150 mM NaCl. For drought treatment, ½ MS contained 5% polyethylene glycol (PEG8000; Sigma-Aldrich). Per Flowpot, five or three surface-sterilized and stratified *A. thaliana* or Micro-Tom seeds were inoculated, respectively. For Gifu, 7 days old, pregerminated seedlings with similar developmental stages were carefully transferred to the Flowpots. Microboxes were then incubated in a light cabinet under short day conditions (10 h light at 21 °C, 14 h dark at 19 °C) for 14 days and randomized every 2–3 days. For low PAR treatments, microboxes were partly covered in cardboard boxes, as described in (Hou *et al.*, 2021).

II.6.5 Natural soil experiments

Cologne agricultural soil (CAS) was obtained from the Max Planck Institute for Plant Breeding Research in Cologne, Germany. R401 WT was cultured as described above. CAS was placed in squared pots with an edge length of 9 cm and flush inoculated with 100 ml sterile water or 100 mM NaCl containing either live or heat-killed R401 WT cells at an OD_{600} of 0.0025. Four surface-sterilized and stratified Col-0 seeds were placed per pot. Pots where then placed in trays in the greenhouse for 28 days. The temperature was set at 22 °C during day and 18 °C during night, with a relative humidity at 65% and 16 h of light.

II.6.6 Agar plate experiments

For the experiment depicted in **Fig. 1A**, 24 surface-sterilized and stratified *A. thaliana* seeds were placed in two rows per 12 cm square plate containing ½ MS medium with 10 g/l Bacto-Agar (Duchefa Biochemie). Plants were grown for 14 days and then flushed with 15 ml 10 mM $MgCl_2$ containing either live or heat-killed R401 WT cells at an OD_{600} of 0.0005 for 5 mins. Plants were transferred to new plates and grown for another 5 days. For the experiment depicted in **Fig. S5C–E**, 24 surface-sterilized and stratified *A. thaliana* seeds were placed in two rows per 12 cm square plate containing ½ MS or 1/10 MS plates with or without live R401 WT cells at an OD_{600} of 0.0005. Agar plates were sealed and incubated in a light cabinet under short day conditions (10 h light at 21 °C, 14 h dark at 19 °C) for 14 days and randomized every 2–3 days.

II.6.7 RNA sequencing experiments

Total RNA was extracted from A. thaliana roots and shoots by RNeasy Plant Mini Kit (Qiagen). RNA-Seq libraries were prepared by the Max Planck Genome-centre Cologne with NEBNext® Ultra™ II Directional RNA Library Prep Kit for Illumina® and then sequenced on a NextSeq 2000 in 2 x 150 paired-end read mode. RNA-Seq read quality was observed with FastQC v0.11.9, then reads were trimmed with Trimmomatic PE v0.38 (Bolger *et al.*, 2014) using parameters TRAILING:20 AVGQUAL:20 MINLEN:100. Trimmed reads were then mapped on the reference *A. thaliana* genome TAIR10 using Hisat2 v2.2.1 (Kim *et al.*, 2019), taking into consideration exon and splicing sites locations (according to annotation file TAIR10_GFF3_genes.gff downloaded from arabidopsis.org in October 2022). The number of fragments (pair of reads) mapped on each gene was then quantified using featureCounts v2.0.0 (parameter -p, default settings; (Liao *et al.*, 2014). Resulting data were used to calculate

FPKM (fragments per kilobase of transcript per million fragments mapped) values for each gene in each sample: (1) Scaling factor: SF=Total number of mapped reads / 1e6; (2) Fragments per million: FPM=Number of reads mapped on one gene / SF ; (3) FPKM= FPM / (Gene length / 1000). Numbers of mapped reads on each gene were also used to perform differential gene expression analysis with DESeq2 v1.24.0 (Love *et al.*, 2014) and functions estimateSizeFactor, estimateDispersions and nbinomWaldTest. log2FoldChanges values were then corrected with shrinkage algorithm apeglm v1.6.0 (A. Zhu *et al.*, 2019). One R401 WT and 100 mM NaCl-treated shoot sample (sample ID: 5642.W) was highly contaminated with brown trout (*Salmo trutta*) reads, likely arising during library preparation. This sample was therefore excluded from the analysis.

II.6.8 BGC prediction using antiSMASH

antiSMASH (Blin *et al.*, 2021) predictions and data from modified Burkholder assay experiments are derived from **Chapter I**.

II.6.9 Δ*sypc* mutant generation

R401 Δ*sypc* mutant generation was conducted as described in **Chapter I**. All utilized primers can be found in **Table S8**.

II.6.10 Quantification of R401 load on plant roots and shoots

Col-0, Gifu and Micro-Tom roots and shoots were carefully cleaned, dried, and collected in pre-weighed, sterile 2 ml tubes containing 1 steel bead (3 mm diameter). Tubes were weighed again to assess the root or shoot fresh weight. Subsequently, samples were ground in a Precellys 24 TissueLyser (Bertin Technologies) for 2 x 30 s at 6,200 rpm with 15 s intervals. Then, 150 µl of sterile 10 mM $MgCl_2$ were added to each tube and roots were ground again under the same conditions. Each sample was subsequently dilute five times 1:10 in sterile 10 mM $MgCl_2$. Undiluted samples and each dilution were plated on 50% TSA square plates, dried and left to grow at 25 °C until single colonies appeared. Pictures were taken and single colonies were counted blinded.

II.6.11 Microbial growth rate validation

Assessment of microbial growth rates was conducted as described before (**Chapter I**). Either artificial root exudates (ARE) or ARE supplemented with 100 mM NaCl were inoculated with R401 WT or Δ*sypc* cells to a final OD_{600} 0.01.

II.6.12 Isolation of R401 Brassicapeptin

R401 was precultured in 300 ml flasks containing 100 ml TSB medium for 2 days at 30 °C and 160 rpm. 80 ml preculture were added to 1 l M19 medium (casein peptone 20 g/l, D-mannitol 20 g/l) in 5 l flasks. This procedure was carried out 70-times. All flasks were incubated at 30 °C and 160 rpm for 24 hours, followed by an extraction using EtOAc (volume ratio 1:1) for three times, yielding 16.24 g crude extract. Twenty-one fractions were collected from reversed phase flash chromatography (Interchim Puriflash 4125 chromatography system with Puriflash C18-AQ30 µm F0120 column) with an elution gradient starting from 10% MeOH/H2O to 100% MeOH over 4 h. Fraction 19 (143.8 mg) was further subjected to semi-preparative HPLC (semipreparative purification column: VP 250/10 Nucleodur C18 Gravity-SB, 5 µm; Macherey-Nagel, Flow: 3 ml/min; Gradient: 0–20 min, gradient increased from 40% to 100% MeOH; 20–32 min, 100% MeOH) to give two subfractions (fractions 19.1 and 19.2). Fraction 20 (96.7 mg) was also subjected to semi-preparative HPLC (semipreparative purification column: VP 250/10 Nucleodur C18 Gravity-SB, 5 µm; Macherey-Nagel; Flow: 3 ml/min; Gradient: 0–20 min, gradient increased from 40% to 100% MeOH; 20–32 min, 100% MeOH) to give two subfractions (fractions 20.1 and 20.2). Subfraction 19.2 (6.7 mg) and 20.2 (6.7 mg) were further purified by semi-preparative HPLC (analysis column: EC 250/4.6 Nucleodur C18 Gravity-SB, 5 µm; Macherey-Nagel; Flow: 1 ml/min; Gradient: 0 – 40 min, gradient increased from 40% to 100% MeOH; 40–50 min, 100% MeOH) to yield Brassicapeptin A (6.1 mg, t_R = 38.4 min). Fraction 18 (108.6 mg) was subjected to semi-preparative HPLC (semipreparative purification column: VP 250/10 Nucleodur C18 Gravity-SB, 5 µm; Macherey-Nagel; Flow: 3 ml/min; Gradient: 0–20 min, gradient increased from 40% to 100% MeOH; 20–32 min, 100% MeOH) to give three subfractions (fractions 18.1–18.3). Subfraction 18.3 (8 mg) was further purified by semi-preparative HPLC (analysis column: EC 250/4.6 Nucleodur C18 Gravity-SB, 5 µm; Macherey-Nagel; Flow: 1 ml/min; Gradient: 0 – 3 min, 10% MeCN; 3–58 min, gradient increased from 10% to 92.5% MeCN; 58–65 min, 100% MeCN) to yield Brassicapeptin A (3 mg, t_R = 56.4 min) and B (0.9 mg, t_R = 52.3 min).

II.6.13 Structure elucidation of R401 Brassicapeptin

The planar structure of the isolated compounds was elucidated by analysis of NMR data, LC-HR-MS, and LC-HR-MS/MS data. The 1D and 2D NMR spectra were recorded in CD_3OD or DMSO-d_6 using Bruker Avance II 600 MHz spectrometers equipped with a Prodigy cryoprobe (Bruker, Ettlingen, Germany) and Bruker Avance Neo 700 MHz spectrometer equipped with a 5 mm CryoProbe Prodigy TCI (^{1}H,^{15}N,^{13}C Z-GRD) (Bruker). The LC-HR-MS and MS/MS data were recorded on a quadrupole time-of-flight spectrometer (LC-QTOF maXis II, Bruker Daltonik) equipped with an electrospray ionization source in line with an Agilent 1290 infinity LC system (Agilent). C18 RP-UHPLC (ACQUITY UPLC BEH C18 column; 130 Å, 1.7 µm, 2.1 × 100 mm) was performed at 45°C with the following linear gradient: 0 min: 95% A; 0.30 min: 95% A; 18.00 min: 4.75% A; 18.10 min: 0% A; 22.50 min: 0% A; 22.60 min: 95% A; 25.00 min: 95% A (A: H2O, 0.1% HCOOH; B: CH3CN, 0.1% HCOOH; flow rate: 0.6 ml/min). Mass spectral data were acquired using a 50 to 2,000 m/z scan range at 1 Hz scan rate. MS/MS experiments were performed with 6 Hz and the top five most intense ions in each full MS spectrum were targeted for fragmentation by higher-energy collisional dissociation at 25 eV or 55 eV using N2 at 10–2 mbar. Precursors were excluded after two spectra, released after 0.5 min, and reconsidered if the intensity of an excluded precursor increased by factor 1.5 or more. The absolute configuration of isolated compounds was elucidated by Marfey assay. A 5 mM stock solution in H_2O was prepared from the reference amino acids. 20 µl 1 M $NaHCO_3$ and 50 µl 7 mM L FDVA (Sigma Aldrich) in acetone was added to 50 µl stock solution of the reference amino acids. The mixture was stirred at 40 °C for 3 h and then quenched by adding 20 µl of 1 M HCl. After evaporation, the residue was dissolved in 40 µl DMSO and analysed by UPLC HRMS (maXis II). Brassicapeptin A (0.5 mg) and B (0.3 mg) were dissolved in 200 µl of 6 M DCl in D_2O and stirred at 160 °C for 7 h. After concentrating the solution under reduced pressure, the residue was dissolved in 200 µl H_2O and 100 µl of 1 M $NaHCO_3$ and 200 µl of 7 mM L FDVA in acetone were added. After stirring for 3 h at 40 °C, the solution was quenched by adding 100 µl of 1 M HCl. After evaporation to dryness, the residue was dissolved in 50 µl DMSO and analysed by UPLC HRMS (maXis II).

II.6.14 In planta activity test of R401 Brassicapeptin A

Surface sterilized and stratified *A. thaliana* seeds were pregerminated on ½ MS agar plates. After seven days, seedlings were transferred to ½ MS agar plates supplemented with either 1 ng/µl, 1 µg/µl Brassicapeptin A solubilized in DMSO or DMSO as negative control and either

0 mM or 100 mM NaCl. After 14 days agar plates for seven days and then transferred to new plates containing NaCl and/or Brassicapeptin A. Agar plates were incubated in a light cabinet under short day conditions (10 h light at 21 °C, 14 h dark at 19 °C) for additional 14 days and randomized every 2–3 days.

II.6.15 Ion leakage assay

Five discs with 3 mm diameter of approx. 28 days old *A. thaliana* Col-0 leaves were transferred to wells of a 24-well plate, filled with sterile Milli-Q water supplemented with either 1 ng/µl, 1 µg/µl Brassicapeptin A solubilized in DMSO or DMSO as negative control. Before the transfer of leaf discs and after 16 h, ion leakage measurements were taken using the Twin Cond conductivity meter B-173 (HORIBA).

II.6.16 Modified Burkholder assays (mBA)

Modified Burkholder assays to determine the antagonistic potential of R401 and its mutants was carried out as described in **Chapter I**. For *F. oxysporum* F212, pieces of 14 days old mycelium were transferred to pre-weighed sterile 2 ml screw cap tubes containing one and approx. 15 steel beads of 3 mm and 1 mm diameter, respectively. Per 50 mg harvested fungal mycelium, 500 µl of sterile 10 mM $MgCl_2$ were added. The mycelium was subsequently grinded in a paint shaker at approx. 600 rpm for at least 10 min until homogeneous. The resulting slurry was used to inoculate 25% TSA medium to a final concentration of 100 µg/ml.

II.6.17 Minimal inhibitory concentration assay

Determination of the minimum inhibitory concentration (MIC) of Brassicapeptin A was carried out by micro broth dilution assays in 96 well plates as literature (Wang *et al.*, 2022). Brassicapeptin A was dissolved in dimethyl sulfoxide (DMSO, Carl Roth GmbH + Co.) with a concentration of 6.4 mg/ml and tested in triplicate. Dilution series (64−0.03 µg/ml) of rifampicin, tetracycline, and gentamicin (all Sigma -Aldrich) were prepared as positive controls for *Escherichia coli* ATCC25922, *Staphylococcus aureus* ATCC25923 and *Listeria monocytogenes* DSM20600. Same dilution series of rifampicin, tetracycline, and isoniazid for *Mycobacterium smegmatis* ATCC607. For *Zymoseptoria tritici* MUCL08, *Botrytis cinerea* HAG001286 and *Colletotrichum coccodes* DSM62126, tebuconazole (Cayman Chemical

Company), amphotericin B (Sigma-Aldrich) and nystatin (Sigma Aldrich) were used as the positive control with same dilution series.

II.6.18 Statistical analyses

All statistical analyses were conducted in R 4.1.2. Data visualisation was conducted using the ggplot2 package (as part of the Tidyverse) or the ComplexHeatmap package. As nonparametric tests, Kruskal-Wallis followed by Dunn's post-hoc test and Benjamini-Hochberg (BH) adjustment for multiple comparisons from the PMCMRplus package (Pohlert, 2022) were used. The respective statistical tests are indicated in each figure description. Significance was indicated by significance group ($p \leq 0.05$). No statistical methods were used to pre-determine sample sizes. Halo size quantification in modified Burkholder experiments, and root length measurements were performed blinded using the Fiji package of ImageJ. Colony counts of R401 were performed blinded. RNA sequencing data processed as described above and further analysed and visualized as described in (Ma *et al.*, 2021). GO Term enrichment was conducted as indicted in the respective figure description or results section. Figures were assembled in Adobe Illustrator.

II.7 Acknowledgements

This work was supported by funds to S.H. from a European Research Council starting grant (MICRORULES 758003) and the Max Planck Society, as well as the Cluster of Excellence on Plant Sciences (CEPLAS) and the Priority Program: Deconstruction and Reconstruction of the Plant Microbiota (SPP DECRyPT 2125; project P.S.-L.: SCHU 799/8-1; project S.H.: HA 8169/2-2), both funded by the Deutsche Forschungsgemeinschaft, as well as funds to P.S.-L. from the Max Planck Society. Furthermore, Work in the Schäberle lab was supported by the German Federal Ministry of Education and Research (BMBF). L.W. was funded by the China Scholarship Council (CSC NO. 201908080177). We thank the Max Planck-Genome-Centre Cologne for advising and performing the RNA sequencing. We also thank Brigitte Pickel for her support in halo size quantifications and Flowpot harvest. Finally, thanks to Neysan Donnelly for editing this chapter and Saurabh Pophaly for support with ENA and NCBI data submission.

II.8 Supplementary figures

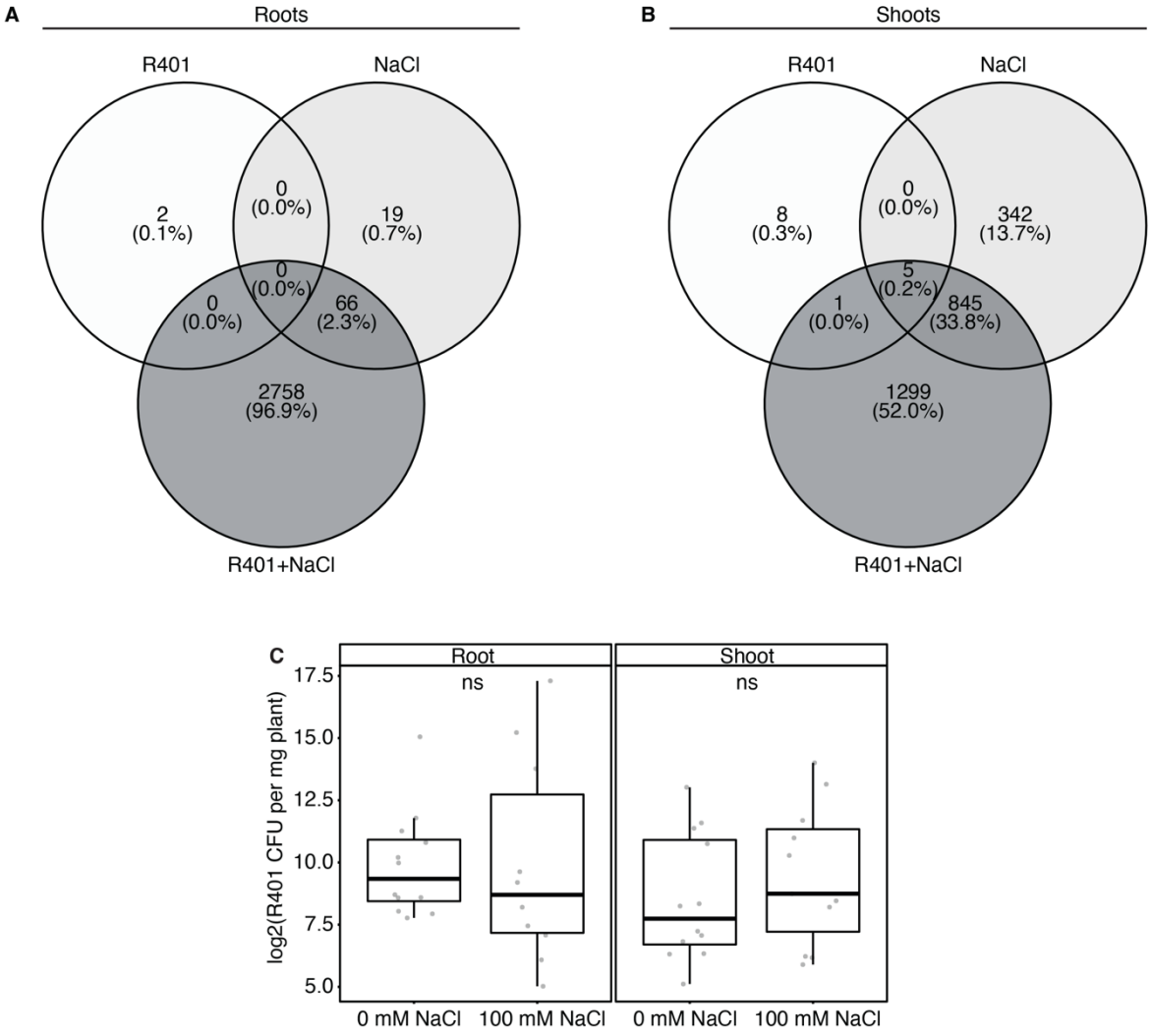

Figure S1 related to Figure 2, R401 colonisation and transcriptome modulation are not linked. (A, B) Venn diagrams of DEGs (from **Figure 2A**) in roots **(A)** and shoots **(B)** of *A. thaliana* plants co-inoculated with R401, 100 mM NaCl or both in the gnotobiotic Flowpot system. DEGs derive from a pairwise comparison to control (HK and 0 mM NaCl)-treated plants. Percentages indicate the total number of DEGs of all three comparisons. **(C)** Colonization capability of R401 WT on roots and shoots of *A. thaliana* seedlings grown in the gnotobiotic Flowpot system for 28 dpi in the presence or absence of 100 mM NaCl. Colony forming units have been normalized to tissue fresh weight; n=12. No statistically significant differences were determined by Kruskal-Wallis followed by Dunn's post-hoc test and Benjamini-Hochberg adjustment as indicated by 'ns', not significant.

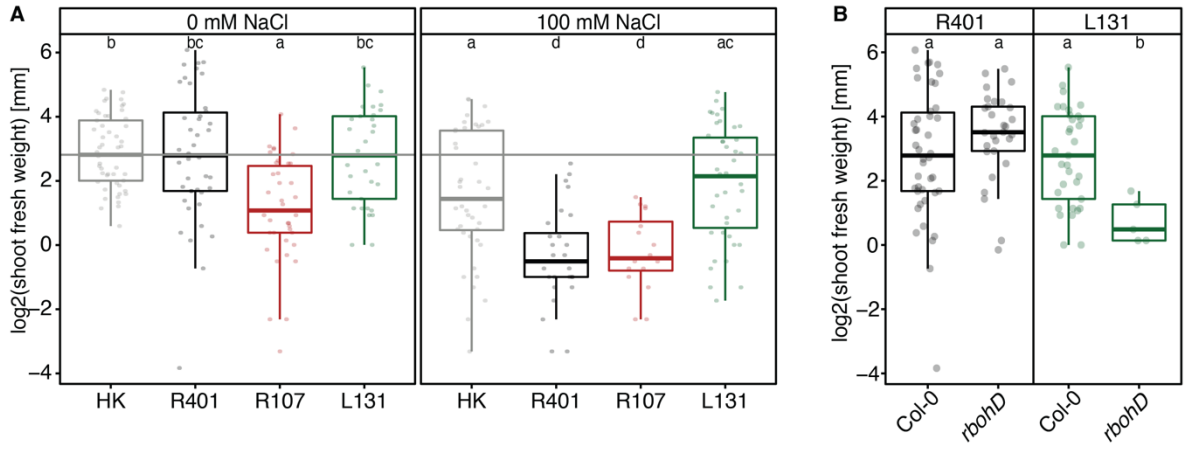

Figure S2 related to Figure 2, R401 does not become detrimental in an immunocompromised *rbohD* mutant. **(A)** log2-transformed shoot fresh weight of *A. thaliana* plants grown in the gnotobiotic Flowpot system for 28 dpi in the presence or absence of 100 mM NaCl and either heat-killed (HK) R401 cells or live R401, *Streptomyces sp.* R107 or *Xanthomonas sp.* L131 cells. **(B)** log2-transformed shoot fresh weight of *A. thaliana* wild type (Col-0) or *rbohD* mutant plants grown in the gnotobiotic Flowpot system for 28 dpi in the presence of either live R401 or *Xanthomonas sp.* L131 cells. Col-0 data are identical with **(A)**. **(A, B)** Letters indicate statistically significant differences as determined by Kruskal-Wallis followed by Dunn's post-hoc test and Benjamini-Hochberg adjustment with $p < 0.05$ (n=30).

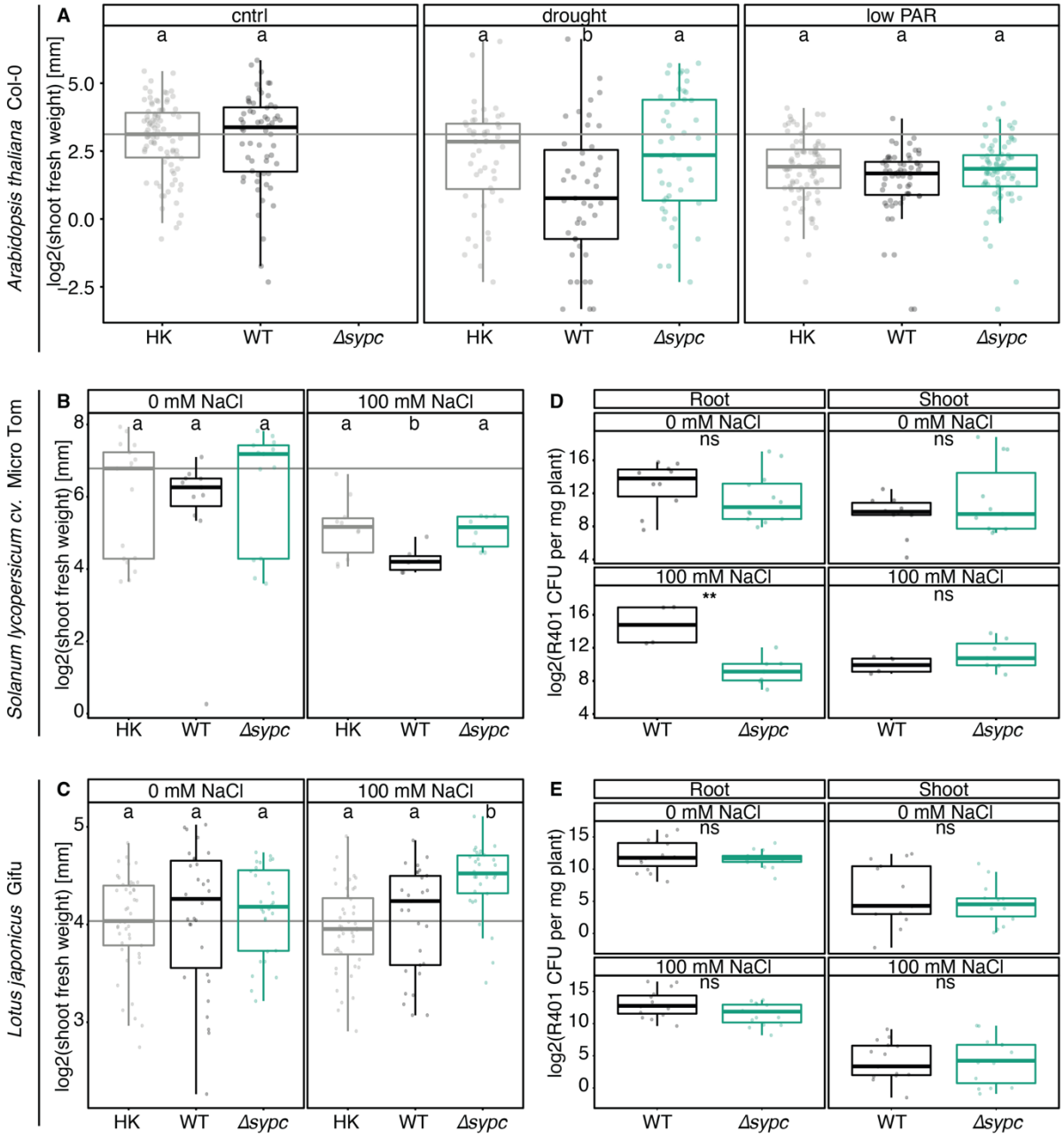

Figure S3 related to Figure 3, Brassicapeptin A production is a salt stress-specific root competence determinant. (A) log2-transformed shoot fresh weight of *A. thaliana* plants grown in the gnotobiotic Flowpot system for 28 dpi in the presence or absence of drought stress (5% PEG8000) or low photosynthetically active radiation (low PAR, induced by shading; Hou *et al.*, 2021) and either heat-killed (HK), live wild-type (WT) or live Δ*sypc* R401 cells (n=30). **(B, C)** log2-transformed shoot fresh weight of *Solanum lycopersicum cv.* Micro-Tom (**A**; n=15) and *Lotus japonicus* Gifu (**B**; n=45) plants grown in the gnotobiotic Flowpot system for 28 dpi in the presence or absence of 100 mM NaCl and either heat-killed (HK), live wild-type (WT) or live Δ*sypc* R401 cells. **(A–C)** Letters indicate statistically significant differences as determined by Kruskal-Wallis followed by Dunn's post-hoc test and Benjamini-Hochberg adjustment with $p < 0.05$. Statistical comparisons were conducted for each abiotic stress treatment separately. **(D, E)** Colonization capability of R401 on roots and shoots of *Solanum lycopersicum cv.* Micro-Tom **(D)** and *Lotus japonicus* Gifu **(E)** plants grown in the gnotobiotic Flowpot system for 28 dpi in the presence or absence of 100 mM NaCl. Colony forming units (CFU) have been normalized to tissue fresh weight; n=15. Statistical significance was determined by Kruskal-Wallis followed by Dunn's post-hoc test and Benjamini-Hochberg adjustment. Significance between WT and Δ*sypc* is indicated by black asterisks

(∗∗ indicates $p < 0.01$; ns, not significant). Statistical comparisons were conducted for each NaCl treatment and compartment separately.

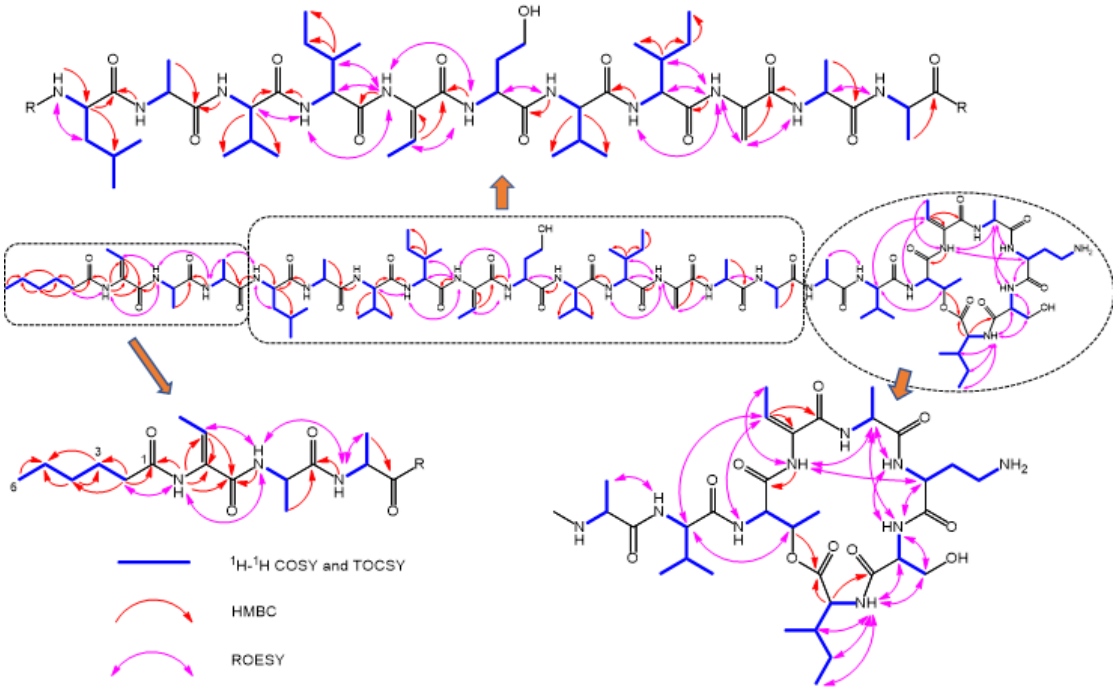

Figure S4, related to Figure 4, 2D-NMR-based structure elucidation of R401 Brassicapeptin. ^{1}H-^{1}H Correlated Spectroscopy (COSY; blue), Total Correlation Spectroscopy (TOCSY; blue), Heteronuclear Multiple Bond Correlation (HMBC; red) and Rotating-frame Nuclear Overhauser Effect Spectroscopy (ROESY; pink) revealed the complete structure of Brassicapeptin.

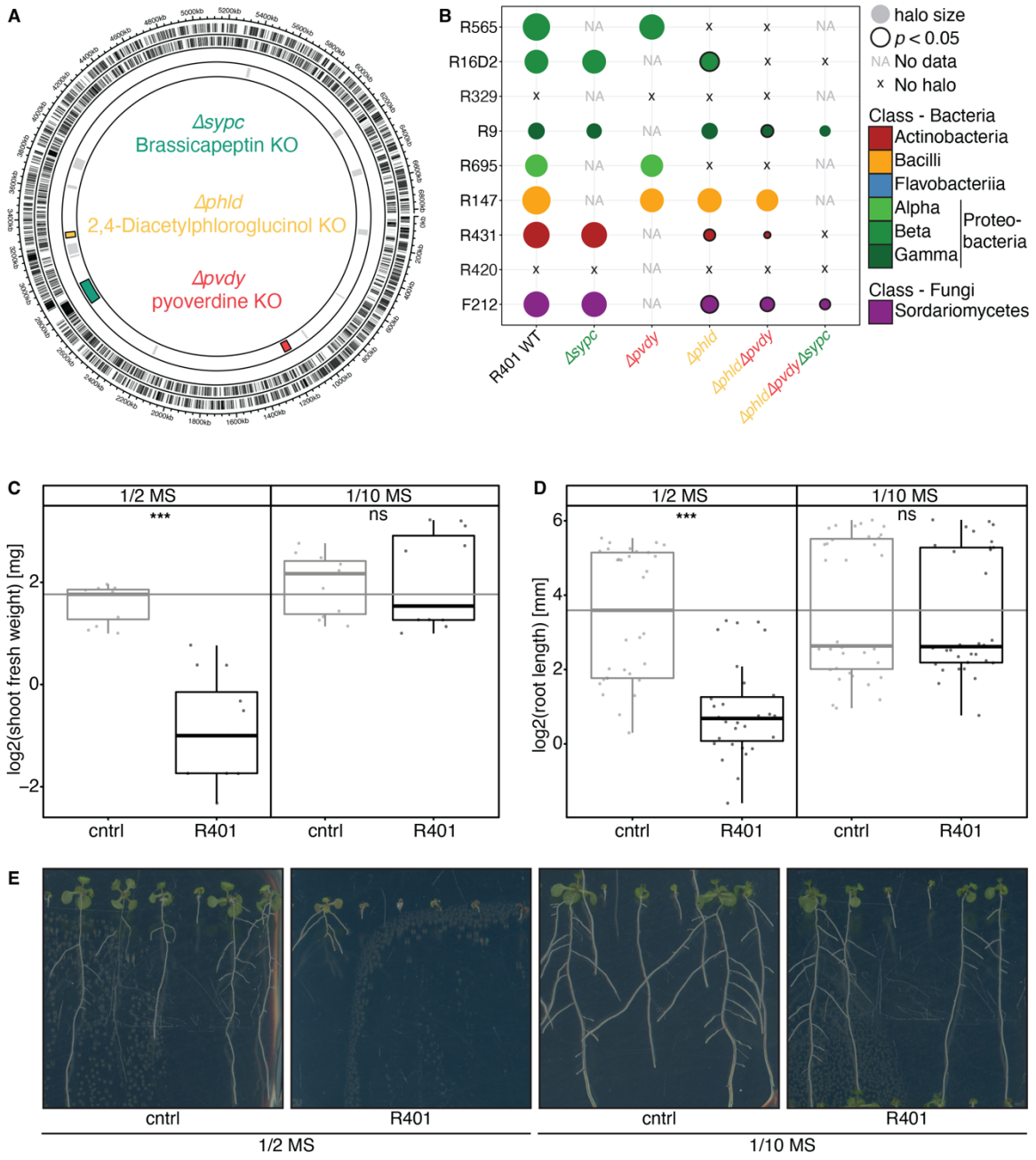

Figure S5 related to Figure 5, R401 detrimental activity in agar plates depends on nutrient salt concentrations. (A) Genomic map of the main chromosome of R401, illustrating the locations of three biosynthetic gene clusters (BGC) involved in Brassicapeptin A (green), 2,4-Diacetylphloroglucinol (DAPG, yellow) and pyoverdine (red) production in R401. Further indicated are respective mutants for each BGC *(*Δ*sypc*, Δ*phld*, Δ*pvdy*, respectively). R401 Δ*phld* and Δ*pvdy* have been characterized previously (**Chapter I**). **(B)** Balloon plot depicting the inhibitory activity of R401 WT and single, double, or triple mutants, with targeted mutations in one of the three BGCs depicted in **(A)** against a taxonomically diverse set of bacteria and one fungus. Inhibitory activity was measured as halo of inhibition size by a modified Burkholder assay as described before (**Chapter I**). Statistical significance was determined by Kruskal-Wallis followed by Dunn's post-hoc test and Benjamini-Hochberg adjustment in comparison to the respective lower-order mutant or the wild-type in the case of single mutants. Black circles indicate $p < 0.05$ (n=5). 'x' indicates no detectable halo formation while 'NA' shows that no data was acquired for the respective comparison. Target strains are coloured based on the bacterial or fungal classes. **(C–E)** Shoot fresh weight **(C)** and root length **(D)** and images of representative phenotypes **(E)** of *A. thaliana* plants grown on ½ MS or 1/10 MS agar plates in the presence (R401) or absence (cntrl) of R401 wild type for 14 dpi. Statistical significance was determined by Kruskal-Wallis followed by Dunn's post-hoc test and

Benjamini-Hochberg adjustment. Significance compared to ctrl conditions is indicated by black asterisks (∗∗∗ indicate $p < 0.001$; ns, not significant). Statistical comparisons were conducted for each MS separately.

II.9 Supplementary tables

Table S6, *A. thaliana* DEGs in roots and shoots in response to R401 and/or NaCl stress

Table S7, Minimal inhibitory concentrations of R401 Brassicapeptin A

Table S8, Primers used in this study

Table S9, Microorganisms used in this study

All supplementary tables have been deposited at EDMOND and can be accessed *via* the following link: https://doi.org/10.17617/3.I1ABIM

Chapter III: Design and validation of a minimal synthetic community for dissecting competitive and cooperative interactions in the root microbiota

Authors
Felix Getzke[1], Victor Mataigne[2], Philippe Vandenkoornhuyse[2], Thorsten Thiergart[1], Dennis Mahr[1], Stéphane Hacquard[1,3,*]

Affiliations
1 Department of Plant Microbe Interactions, Max Planck Institute for Plant Breeding Research, 50829 Cologne, Germany

2 Université de Rennes 1, Rennes 35042, France

3 Cluster of Excellence on Plant Sciences (CEPLAS), Max Planck Institute for Plant Breeding Research, 50829 Cologne, Germany

III.1 Summary

In nature, plant roots are colonized by diverse soil-derived bacterial and fungal communities, collectively termed the root microbiota. Studying the functions and rules driving the establishment of these communities is hindered by their complexity. Here, we describe a minimal synthetic community (MiniSynCom) comprised of eleven bacteria and four fungi, representing highly prevalent strains of each core microbial class stably associating with *Arabidopsis thaliana* roots across a European transect. This MiniSynCom recapitulates functions of highly complex microbial consortia, suggesting that a low diversity core microbiota is largely sufficient for fulfilling key microbiota functions. By assessing 225 pairwise microbe-microbe interaction phenotypes in sterile peat and artificial root exudates, we observed that the growth media extensively modulates inter- but not intra-kingdom interactions. In particular, antagonistic interactions prevailed in root exudate-mimicking growth media, whereas cooperative interactions dominated in a soil-like peat matrix, suggesting a key role of the host in driving microbial antagonism.

Keywords
Root microbiota, SynCom, bacteria, fungi, soil, root, rhizosphere, binary interactions, microbiota, competition

III.2 Author contributions

S.H., and F.G. developed the project and designed experiments. V.M. performed phylogenomic analyses and metabolomic modelling. F.G. and D.M. performed Flowpot experiments and microbiota profiling. F.G. performed all other experiments. T.T. generated all ASV tables. S.H. supervised the project. F.G. and V.M. generated the figures. F.G. wrote this chapter.

III.3 Introduction

Natural soils represent an important reservoir of biological diversity at microscopic ranges, primarily in the form of bacteria and fungi that constitute the primary inoculum for microbial communities associating with subterranean plant organs (Bahram *et al.*, 2018; Bulgarelli *et al.*, 2012; Tringe *et al.*, 2005). While the soil biota is heavily influenced by edaphic and climatic factors, resulting in soil type-specific microbiota structures, bacterial and fungal communities structurally converge towards plant roots along the soil-root continuum (Fierer & Jackson, 2006; Getzke *et al.*, 2019; Tedersoo *et al.*, 2014; Thiergart *et al.*, 2019). This process is accompanied by a gradual reduction in microbial alpha-diversity across the soil-root continuum (Bulgarelli *et al.*, 2012; Edwards *et al.*, 2015; Lundberg *et al.*, 2012), indicating that selective forces restrict root colonisation to highly adapted and competitive microbial strains.

Bacterial and fungal marker gene amplicon sequencing approaches have allowed for a descriptive assessment of microbial community structures in natural settings and cataloguing of root-enriched microorganisms. Subsequent efforts to isolate bacterial and fungal strains from plant roots of the model plant *Arabidopsis thaliana* demonstrated that significant fractions of bacterial and fungal communities (54–64% and 37–50%, respectively) were cultivatable (Bai *et al.*, 2015; Durán *et al.*, 2018). Microorganisms belonging to the bacterial Phyla Proteobacteria, Actinobacteria, Bacteroidetes and Firmicutes and the fungal Phylum Ascomycota, respectively, constitute >92% and >63% of the amplicon sequence variants (ASVs) found associated with *Arabidopsis* roots in nature and are widely culturable in laboratory conditions (Bai *et al.*, 2015; Durán *et al.*, 2018; Thiergart *et al.*, 2019). This cultivability and conservation of species allows for microbiota reconstruction approaches using synthetic communities (SynComs) of reduced complexity. SynComs approximate microbial communities in nature and can allow for strain-specific monitoring of, *e.g.*, microbial abundances. Furthermore, they enable manipulation of properties of ecological communities or genetics of individual strains (*e.g.*, Carlström *et al.*, 2019 and **Chapter I**) and, thereby, allow for the identification of causal links in highly complex multipartite systems.

Characterizing microbiota functions (*i.e.*, host immunomodulation, promotion of abiotic stress tolerance or inorganic nutrient uptake) with beneficial impacts on the host are also greatly facilitated by the use of SynComs and germ-free plants in microbiota reconstitution experiments (Harbort *et al.*, 2020; Ma *et al.*, 2021; Wippel *et al.*, 2021). However, most studies are solely centred on the bacterial fraction of the root microbiota, meaning that the vast fungal diversity associating with plant roots remains understudied and underappreciated (Marín *et al.*, 2021).

By reconstituting multikingdom synthetic communities, Durán *et al.* (2018) were able to establish a direct link between community-level interkingdom interactions and plant health, as co-inoculation of bacteria and filamentous eukaryotes results in enhanced survival rate and shoot fresh weight compared to the germ-free control plants. These data provided first evidence for the relevance of co-assessing bacterial and fungal fractions of the root microbiota. The complexity of the utilized SynCom, however, which comprises 148 bacteria and 34 fungi, results in high genetic redundancy between isolates, rendering mechanistic assessment of microbial genetic determinants underlying the observed phenotypes difficult.

Here, we utilize bacterial and fungal amplicon sequencing data from microbial communities sampled across a European transect and stably associating with *Arabidopsis* roots over three consecutive years to design a minimal 15-member multikingdom synthetic community comprising highly prevalent strains from all core bacterial and fungal classes. Further, we provide ecological and physiological evidence that this SynCom recapitulates the main functions of the core root microbiota and characterise pairwise intra- and interkingdom interactions between all strain combinations under two nutrient regimes, resembling the transition at the soil-root continuum. We establish an *ex planta* quantitative abundance protocol, and score interaction outcomes of 225 strain combinations by profiling 3,072 samples using bacterial *16S* rRNA v5v7 and fungal internal transcribed spacer 1 (ITS1) region-specific primers in two growth systems. This reveals high plasticity of in inter- but not intrakingdom interactions due to the availability of easily accessible carbon.

III.4 Results

III.4.1 Rational design of a minimal synthetic community resembling the naturally occurring core microbiota of *Arabidopsis* roots

Mechanistic understanding of microbiota functions is often limited by genetic and functional redundancy within complex microbial communities. To overcome these limitations for the *A. thaliana* root microbiota, we established a minimal synthetic community (MiniSynCom, MSC) composed of bacterial and fungal isolates that represent the most prevalent amplicon sequence variants (ASVs) stably associating with *Arabidopsis* roots across a European transect over three consecutive years (Thiergart *et al.*, 2019). With reference to previous design of highly complex synthetic communities (Durán *et al.*, 2018), we selected bacteria and fungi that, at higher taxonomic ranks (class-level), collectively represent the intra- and inter-kingdom community partitioning found in nature (**Fig1. A**–**B**). A total community size of 15 members (11 bacteria and 4 fungi) was defined as the minimal size that allowed incorporation of all major microbial classes without causing over- or underrepresentation of microbial classes (**Fig1. A**–**B**). For community selection, we could capitalize on established bacterial and fungal culture collections (*At*-RSphere; Bai *et al.*, 2015 and Durán *et al.*, 2018, respectively). We focused on isolates that were originally isolated from *A. thaliana* roots grown in Cologne agricultural soil (CAS) and for which whole-genome sequences are available (**Fig. 1C–F**). Furthermore, the isolates *16S* rRNA v5v7 or ITS1 regions should show 100% sequence identity with the respective ASV sequence, while, as a community, all strains must be distinguishable by the respective marker gene regions, based on a minimum of four mismatches. The identity of each microbial isolate was re-validated using *16S* rRNA v5v7 or ITS1 region amplicon sequencing and all draft genomes are currently being finalized using long-read sequencing approaches (**Table S10**). Our SynCom of minimal size recapitulates the phylogenetic diversity and likely core genomic functions of more complex communities. To validate genome-encoded functions of the MSC, we randomly selected 11-member bacterial communities from the *At*-RSphere culture collection *in silico* and retrieved their genomes for comparative genomic analyses of the randomly selected SynComs in comparison to the MSC. Computing the mean whole genome phylogenetic distance within each community corroborated the exceptionally high phylogenetic distance for the MSC members, which was our aim during SynCom selection (**Fig. S1A**). Using a computational approach, we assessed genomic capacities for the production of microbial metabolites, such as vitamins, amino-acids, and phytohormones – metabolites that likely fulfil important functions in microbial interactions with the host (Duca & Glick, 2020;

Eichmann *et al.*, 2021; Moormann *et al.*, 2022; Ramírez-puebla *et al.*, 2013). The comparison of the bacterial MSC with randomly selected 11-member communities showed below-average overlap in metabolic pathways (Intersect of interactions, **Fig. S1B**), confirming low genetic redundancy within the MSC. Thus, the MSC possesses an above-average collective potential for metabolite production (Union of interactions, **Fig. S1C**), indicating a high potential for metabolic exchange and cross-feeding between SynCom members.

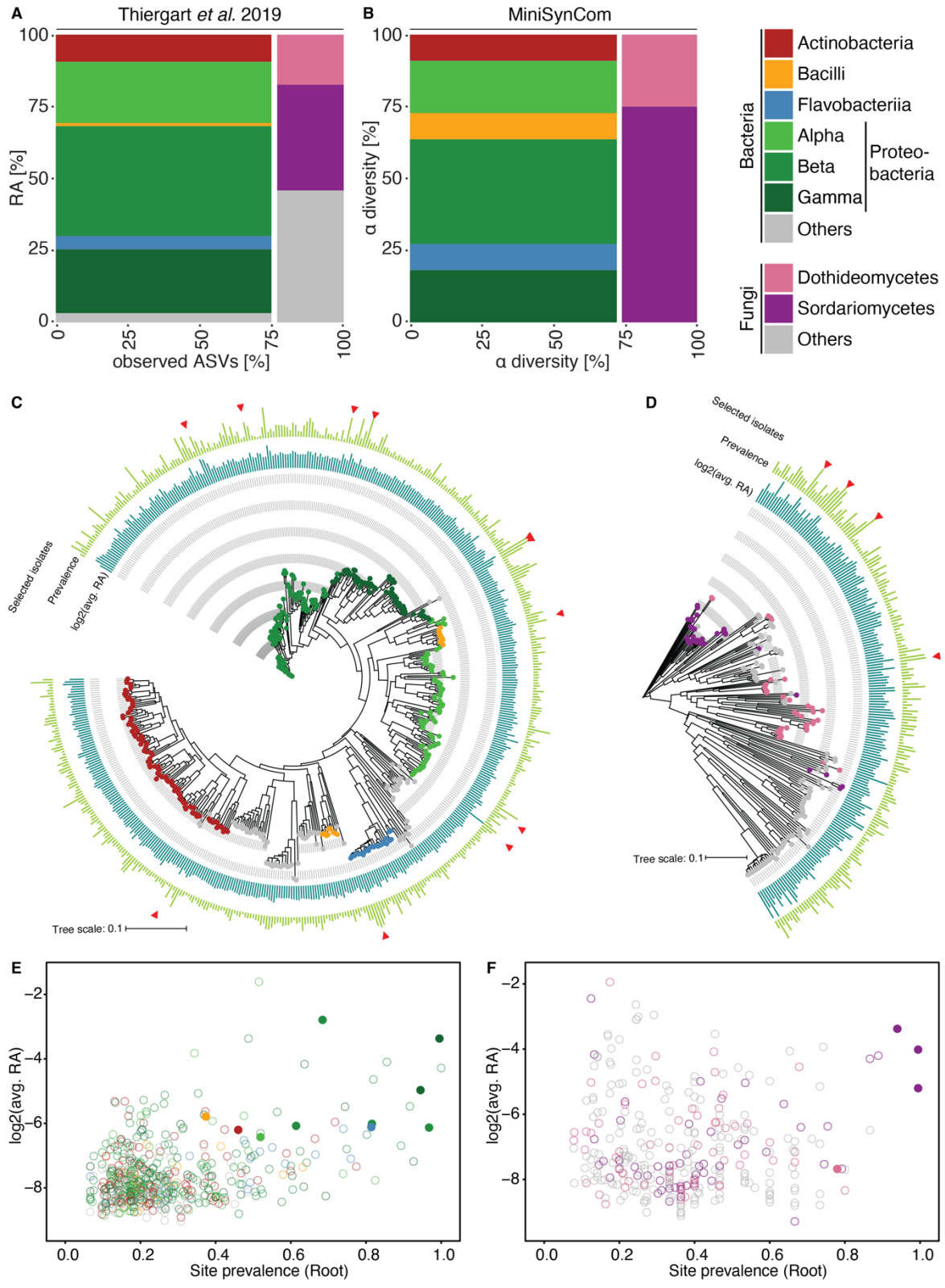

Figure 1, Ecology-inferred design of a minimal synthetic community (MiniSynCom). (A) *Arabidopsis* root-associated bacterial and fungal community profiles across a European transect in a two-dimensional stacked bar plot based on Thiergart *et al.*, (2019). **(B)** Taxonomic distribution at class-level of bacteria and fungi within the MiniSynCom as inferred from **(A)**. **(C–D)**, Clustal Omega-computed (Madeira *et al.*, 2022) phylogenetic trees of all bacterial **(C)** and fungal **(D)** ASVs that were detected across a European transect (Thiergart *et al.*, 2019) based

on *16S* rRNA v5v7 and fungal internally transcribed spacer 1 (ITS1) regions, respectively. Blue bars represent log_2-transformed relative abundances averaged across all samples, green bars represent the corresponding prevalence and red triangles mark isolates that constitute the MiniSynCom. **(E)** and **(F)**, log_2-transformed average relative abundance plotted against the respective site prevalence with each dot representing one bacterial **(E)** or fungal **(F)** ASV from **(C)** and **(D)**, respectively. Filled dots, represent ASVs within the MiniSynCom. **(A–E)**, ASVs are coloured based on their taxonomy and clustered based on either bacterial rRNA *16S* v5v7 or fungal ITS1 sequences.

III.4.2 MSC recapitulates the community functions of complex synthetic communities

To assess the functional capabilities of the MSC, we assessed whether inoculation with this SynCom could recapitulate plant phenotypes that have so far only been described for highly complex synthetic communities (*approx*. 190 members, Durán *et al.*, 2018; Hou *et al.*, 2021; Wolinska *et al.*, 2021). First, we assessed community-scale interkingdom interactions and their effect on the host. Using the gnotobiotic Flowpot system (Kremer *et al.*, 2021), we co-inoculated sterile *A. thaliana* seeds and either the bacterial (B), the fungal (F) or the full MSC (BF); inoculation of axenic medium served as microbe-free control (MF). As for complex synthetic communities (Durán *et al.*, 2018; Wolinska *et al.*, 2021), fungi had detrimental effects on the host. Bacteria alone did not show any effect on the host phenotypes but were able to rescue plant growth when co-inoculated with the fungal MSC (**Fig. 2A**). Previously, it was demonstrated that individual bacteria – including *Pseudomonas aeruginosa* R9, as member of the MSC – are sufficient to rescue plant growth upon co-inoculation with a fungal community (Durán *et al.*, 2018). To test whether the rescuing activity observed for the MSC depends solely on R9, we performed microbial dropouts (*i.e.*, sequential removal of every strain from the MSC in order to generate 15 SynComs each composed of 14 strains; *see* Carlström *et al.*, 2019). This revealed functional redundancy in the detrimental and protective activity of the fungal and bacterial MSC, respectively (**Fig. 2B**). Coupled with the high genetic diversity of MSC members, this suggests that multiple independent and functionally redundant mechanisms contribute to robust protective activities. Next, we assessed the MSC's capacity for abiotic stress alleviation. Namely, we tested whether the MSC is sufficient to rescue plant growth under low photosynthetically active radiation (low PAR) or salt stress (100 mM NaCl). Again, no significant effects of MSC inoculation under unstressed conditions were observed. Consistent with previous work, both low PAR and salt stress significantly reduced plant shoot fresh weight (Hou *et al.*, 2021), while MSC inoculation partially rescued plant growth under these same stress conditions (**Fig. 2C**). Collectively, these data confirm that a minimal synthetic

community can recapitulate community functions of highly complex root-associated microbial communities.

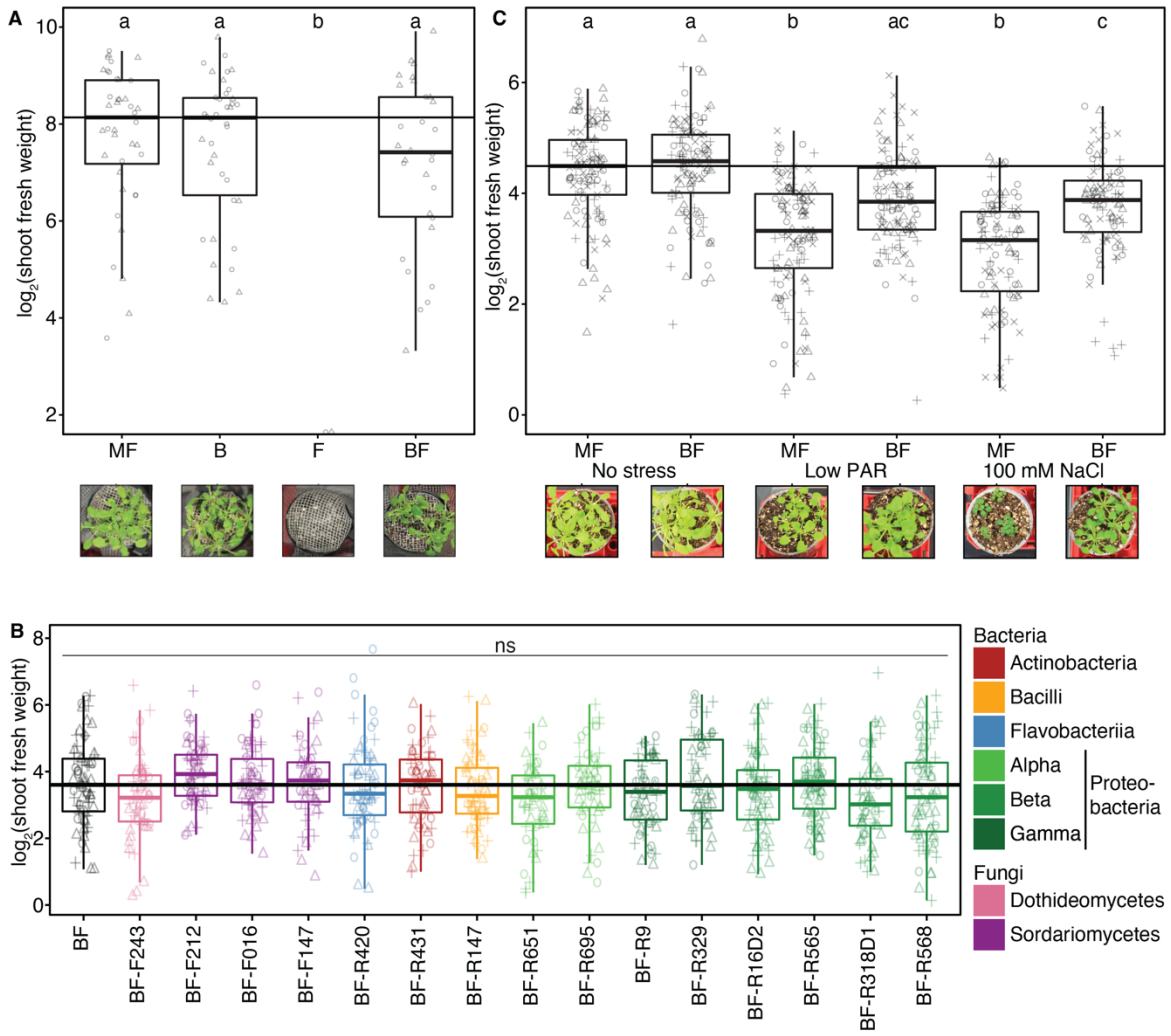

Figure 2, MiniSynCom recapitulates community functions of complex synthetic communities. **(A–C)** log_2-transformed shoot fresh weights of 28-day-old *A. thaliana* seedlings grown in the gnotobiotic Flowpot system. Images depict representative phenotypes. **(A)** *A. thaliana* was grown axenically ('MF') or in the presence of bacterial ('B'), fungal ('F') or combined ('BF') communities derived from the MiniSynCom; n=30. **(B)** Plants were grown with the full, 15-member MiniSynCom ('BF') or in different 14-member SynComs, lacking the respective strain as indicated on the x-axis; n=90. **(C)** Plants were grown axenically ('MF') or with the full MiniSynCom ('BF') in low photosynthetically active radiation- ('Low PAR') and salt- ('100 mM NaCl') stressed or unstressed ('No stress') conditions; n=90. **(A–C)** Letters indicate statistically significant differences as determined by the Kruskal-Wallis followed by Dunn's post-hoc test and Benjamini-Hochberg adjustment with $p < 0.05$; ns, not significant.

III.4.3 Binary interactions in artificial root exudates predict microbial prevalence at the root

Our results demonstrate that while bacterial protection against detrimental fungal activity is functionally redundant, the mechanisms at play are unlikely to be conserved at the genetic level (**Fig. 2B**). To gain more information on the specific inter- and intrakingdom interactions that putatively occur in the root vicinity we performed a binary interaction assay between all MSC members. To this end, we established an *in vitro* assay that allows for high-throughput assessment of hundreds of different pairwise microbial combinations by monitoring microbial abundances of both interaction partners. In brief, we inoculated individual microbes or microbial pairs in a 96-well plate system into artificial root exudates (ARE), a liquid medium that recapitulates the nutritional conditions in the root vicinity (Baudoin *et al.*, 2003). Subsequently, we isolated DNA and performed *16S* rRNA v5v7 and ITS1 amplicon sequencing to assess bacterial and fungal abundances, respectively. In conditions where only one or two microbes are present, relative abundances are not informative. Therefore, we established a spike-in plasmid (hereafter referred to as spike)-based method to assess spike-normalized quantitative abundances (QA) for bacteria and fungi in the absence of the host plant, as such protocols have only been used to assess QA of root-associated microbes (Guo *et al.*, 2020). To assess the feasibility of the proposed spike-based normalisation, we profiled MSC-inoculated soil samples from Flowpot experiments after adding increasing concentrations of spike. The utilized spike (BI-124, Guo *et al.*, 2020) comprises both *16S* rRNA v5v7 and ITS1 region-specific primer binding sites, resulting in co-amplification with bacterial and fungal marker gene amplicons. For both bacterial and fungal marker gene regions, we find a linear association of spike input concentration and resulting spike abundances (**Fig. S2A** and **B**), indicating that this method is suitable for assessing bacterial and fungal quantitative abundances irrespective of the ratio of spike to microbial reads. To validate that changes in microbial load do not skew quantitative abundance community profiles, we furthermore added DNA of one axenically grown bacterium and one fungus, whose marker gene sequences can be differentiated from all MSC strains, to half of the samples prior to marker gene amplification. When computing spike-normalized QA, it becomes evident that an increase in total quantitative abundance by artificially adding microbial DNA does not alter the community composition, further validating the robustness of this method and confirming the feasibility of the spike-based marker gene read count normalisation in the absence of a plant (**Fig. S2 C** and **D**).

We then applied this normalisation method to all 1,536 samples from the binary interaction screen in ARE (*see* **Fig. S2E** for a schematic representation of the conducted normalisation steps). For each sample, amplicon sequencing libraries for bacterial and fungal marker genes were constructed, out of which only 34 samples (~1%) were contaminated and excluded from the subsequent analyses. Computation of interaction scores for effector and target microbes (*i.e.*, target and effector scores, respectively) revealed strain-specific interaction profiles. Here, antagonistic interactions prevail over binary interactions in the presence of easily accessible carbon (**Fig. 3A**). We then calculated a cumulative effector and target score for each MSC member, which revealed quantitative differences in sensitivity and antagonistic capacity for all tested strains; however, this analysis also highlighted a few highly susceptible (R16D2, R695 and F243) and one highly antagonistic strain (R9; **Fig. 3B**), making the latter a potentially interesting strain for subsequent assessment of the underlying mechanisms. We previously demonstrated that interbacterial inhibition functions as a root competence determinant (**Chapter I**). Therefore, we assessed whether microbial prevalence across a European transect can be explained by microbial effector or target scores. While target scores (*i.e.*, sensitivity) were not significantly predictive of microbial prevalence, effector scores (*i.e.*, antagonism) could explain prevalence based on regression analysis (**Fig. 3 D** and **E**). This became even more apparent when performing the same analysis for bacterial and fungal effector scores separately (bacteria: p=0.013, R^2=0.46; fungi: p=0.005, R^2=0.99). This data corroborates the previously described (**Chapter I**) relevance of microbe-microbe interactions for root microbiota establishment. To gain insights into potential mechanisms that explain the observed phenotypes, we first tested whether exometabolites may be of relevance, as observed before (**Chapter I**). When comparing the number of predicted biosynthetic gene clusters, a proxy for inhibitory activity and the mean capacity for halo production, a proxy for exometabolite-mediated antagonism, with the observed effector scores, no association of the data was to be observed, indicating that, while exometabolites are likely involved in the outcome of some binary interactions, they are not the key driver thereof (**Fig. S3A** and **B**). Microbial interactions involve competition for resources; we therefore hypothesized that rapid microbial growth could be advantageous in direct competition. We assessed microbial growth rates by continuously measuring Abs_{600} of axenically grown bacteria and fungi grown in ARE. Indeed, microbial growth rate was a good predictor of interaction outcome and could significantly explain differences in effector and target scores (**Fig. S3C** and **D**). Taken together, our data suggests that microbial competitiveness involves direct competition for nutrients through microbial

outgrowth, which is likely also involved in root competence, as our data can explain microbial prevalence at *A. thaliana* roots in nature.

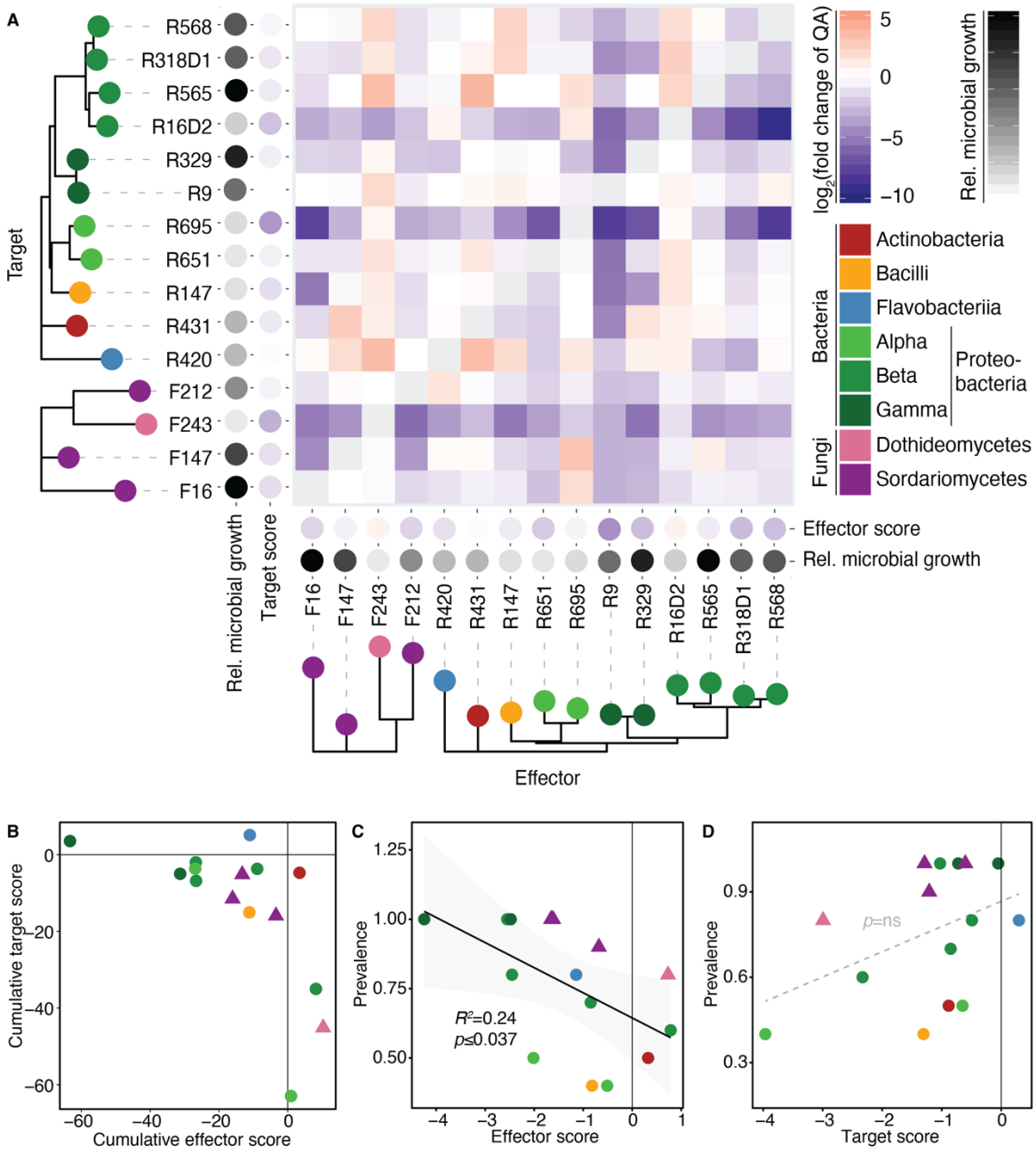

Figure 3, Binary interactions in artificial root exudates predict microbial prevalence at the root. (A–C) Individual bacteria or fungi were either co-inoculated in pairs or grown axenically in liquid artificial root exudates medium for 24 h. Based on spike-normalized community profiling of the bacterial *16S* rRNA v5v7 and fungal ITS1 regions, microbe-microbe interaction (MMI) profiles were computed for all tested binary combinations of strains. Further details can be found in **Fig. S1E** and the Method section. **(A)** Heatmap of all binary MMI within the MiniSynCom in ARE, with each tile reflecting the $\log_2$-transformed fold change of the respective target's quantitative abundance in the presence of an effector microbe normalized by the microbe's quantitative abundance in axenic conditions. Averages thereof are represented as effector and target scores, while the relative microbial load refers to a microbe's relative load in axenic conditions. Microbes are coloured at class-level and clustered by Clustal Omega-computed (Madeira *et al.*, 2022) phylogeny of the bacterial *16S* rRNA v5v7 or the fungal ITS1 regions. **(B)** Cumulative effector and target scores for each tested bacterium (circle) and fungus

(triangle). **(C–D)** Regression analysis of microbial effector **(C)** and target **(D)** scores with microbial prevalence at *Arabidopsis* roots across a European transect (Thiergart *et al.*, 2019). *p*-values and R^2 derive from linear models; ns, not significant.

III.4.4 Interkingdom interactions modulate bacterial proliferation in peat

In ARE, we primarily identified antagonistic interactions between all tested microbes. We hypothesized that microbial interactions are modulated by the nutritional status – as occurs along the soil-root continuum in nature. To mimic these contrasting nutritional regimes *in vitro*, we repeated the binary interaction assay in peat, using a comparable spike- and marker gene amplicon sequencing-based approach. Alteration of the nutritional regime quantitatively altered the interaction profiles of most binary combinations. Nonetheless, antagonistic interactions prevailed over cooperativity, while the magnitude of antagonistic interactions was generally reduced (**Fig. 4A**). A comparison of effector and target scores for each binary interaction in ARE and peat confirms that, qualitatively, 63% of all binary combinations remain unchanged in both systems (**Fig. S3A** and **B**, quadrants **II** and **III**). This suggests that while interaction amplitude might be altered by the nutritional regime, the general type of interaction remains stable even in strongly differing systems. Next, we computed interaction networks, depicting all substantial binary interactions (**Fig. 4B** and **D**) and aggregated the outgoing and incoming nodes by microbial kingdom (**Fig. 4C** and **E**) for binary interaction data from ARE and peat. While intrakingdom interactions remained antagonistic irrespective of nutritional regime, interkingdom interactions are bidirectionally modulated. *i.e.*, in peat, the presence of bacteria negatively affects fungal abundance to a lesser extent compared to ARE. Reciprocally, the presence of fungal isolates is more beneficial for bacterial performance in peat (**Fig. 4B**–**E**). This suggests that in environments comprising primarily complex carbon as nutritional sources, bacteria rely on the presence of fungi for improved growth.

Taken together, we established an ecologically and functionally relevant minimal synthetic community with reduced genetic redundancy for the assessment of microbiota functions in a community context. As proof of principle, we assessed binary interactions between all SynCom members and could reveal nutrient regime-driven modulation of microbial interkingdom interactions, pointing towards bacterial growth facilitation by fungal isolates in the absence of easily accessible carbon.

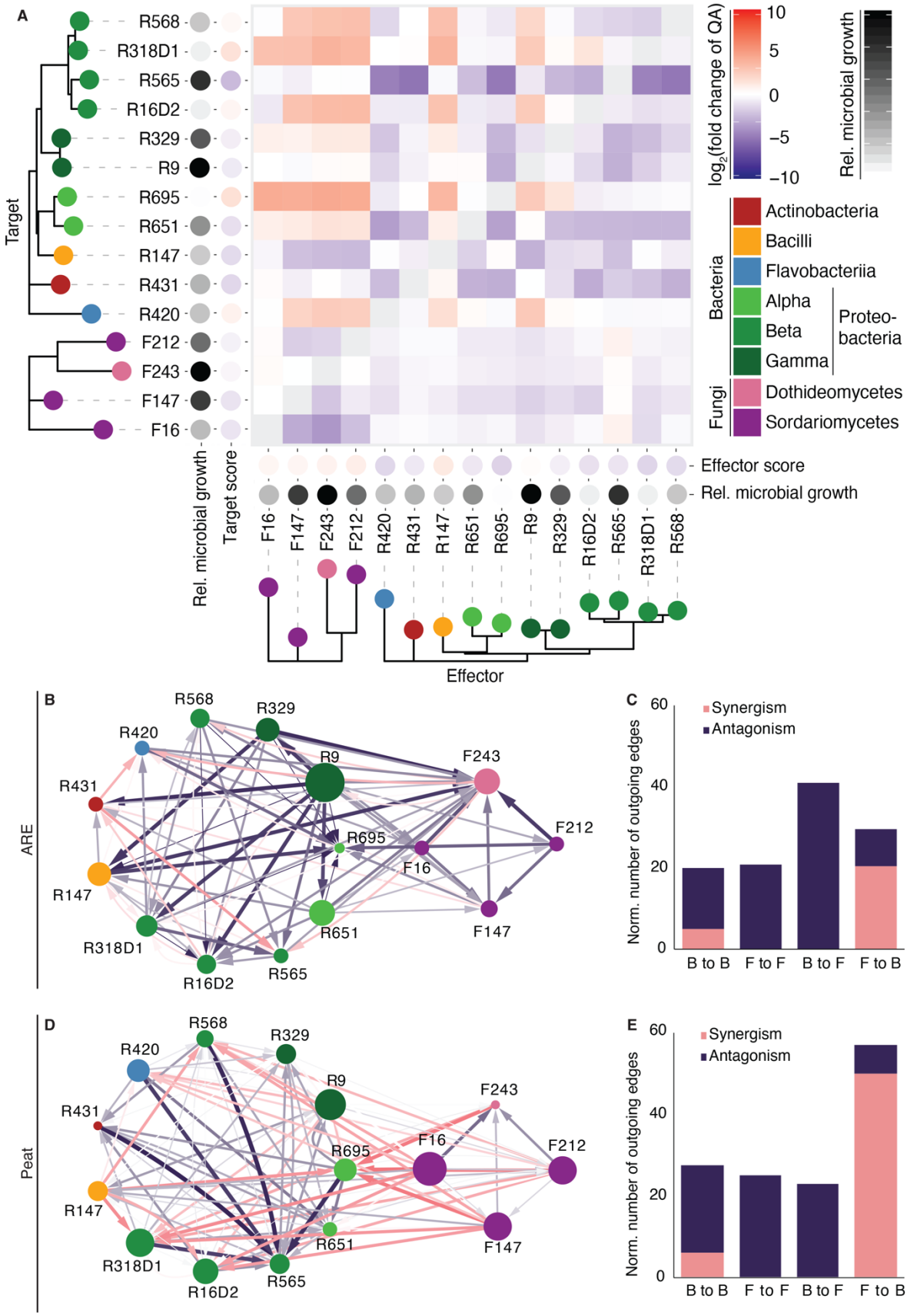

Figure 4, Interkingdom interactions modulate bacterial proliferation in soil. (A) Heatmap of all binary MMI within the MiniSynCom in peat, with each tile reflecting the log_2-transformed fold change of the respective target's quantitative abundance in the presence of an effector microbe normalized by the microbe's quantitative abundance

in axenic conditions. Averages thereof are represented as effector and target scores, while the relative microbial load refers to a microbe's relative load in axenic cultures. Microbes are coloured by class and clustered by Clustal Omega-computed (Madeira *et al.*, 2022) phylogeny based on either the bacterial *16S* rRNA v5v7 region of the fungal ITS1 region, similarly to **Fig. 3A**. **(B and D)** Interaction networks of all members of the MiniSynCom, based on **Fig. 3A** and **(A)** for **(B)** and **(D)**, respectively. Node colours represent microbial phylogeny and edge colour represents $\log_2$ transformed fold changes. While node size represents a nodes outdegree (*i.e.,* a measure for connectedness), node position does not reflect biological data. **(C and E)** represents the number of outgoing edges of **(B)** and **(D)**, respectively, aggregated by microbial kingdom and type of interaction outcome.

III.5 Discussion

Synthetic microbial communities constitute an important tool for dissecting microbiota functions (*e.g.*, Castrillo *et al.*, 2017; Finkel *et al.*, 2019; Harbort *et al.*, 2020; Hou *et al.*, 2021; Wolinska *et al.*, 2021) and allow bridging of the gap between descriptive observations made in natural microbial communities and simplistic mono-association experiments of individual microbial isolates and their hosts in laboratory conditions (Marín *et al.*, 2021). For the *A. thaliana* root microbiota, prior studies incorporating both bacteria and fungi primarily relied on complex SynComs constituting approx. 190 members, thereby incorporating a vast diversity of strains with high genetic and thereby functional redundancy (Durán *et al.*, 2018; Hou *et al.*, 2021; Wolinska *et al.*, 2021). Here, we used ecological data from natural communities to establish a MiniSynCom composed of some of the most prevalent bacterial and fungal strains associated with *Arabidopsis* roots across a European transect (Thiergart *et al.*, 2019), that partly constitutes a core microbiota. Genomics-based metabolic modelling suggested little functional overlap between selected strains (**Fig. S3B**). Inoculation of the MSC on axenic *A. thaliana* reconstituted functions of complex SynComs (**Fig. 2**; Durán *et al.*, 2018; Hou *et al.*, 2021; Wolinska *et al.*, 2021). Microbial diversity has been considered a key predictor of a functional microbiome that provides benefits to the plant (Hu *et al.*, 2016; Wei *et al.*, 2015, 2019). Our data indicates that beneficial microbiota functions may primarily be driven by the core microbiota, while the accessory microbiota appears to be potentially dispensable for the amelioration of the herein-tested abiotic stresses.

With our MiniSynCom, we have established an ecologically relevant toolbox that allows for mechanistic assessment of bacterial and fungal microbiota functions in a community context. As a proof of principle, we characterized binary interactions between all SynCom members in two differing nutrient regimes, an experimental approach that would not be feasible with more complex SynComs. This approach revealed extensive antagonistic interactions between microbial kingdoms under nutrient-rich, *i.e.*, root exudate-mimicking conditions, thereby confirming co-occurrence network analyses of the bacterial and fungal root microbiota, which revealed strong negative associations between the kingdoms on *Arabidopsis* roots (Durán *et al.*, 2018). In our data, every tested bacterial isolate was able to strongly antagonise at least one fungus, namely, *Dendryphion nanum* F243, in ARE. This fungus belongs to the Dothideomycetes, a fungal class that, in contrast to the other herein-tested fungi was especially negatively correlated with many bacterial operational taxonomic units at natural sites (Durán *et al.*, 2018), indicating a high overall sensitivity towards bacteria. Similarly, a marked overlap

between highly antagonistic bacterial taxa identified here and in prior experiments can be observed. Namely, *Pseudomonas aeruginosa* R9 was exceptionally antagonistic towards all tested fungi in our experiments and could, alone, protect *A. thaliana* seedlings from a 34-member fungal community in a gnotobiotic system (Durán *et al.*, 2018), suggesting that it either uses multiple mechanisms to antagonise phylogenetically diverse fungi or a single mechanism that targets highly conserved fungal structures or pathways. Based on field studies of disease-suppressive soils, bacterial exometabolites could constitute a likely explanation for the observed antagonistic phenotype of pseudomonads and R9 in particular (Cartwright *et al.*, 1995; Chin-A-Woeng *et al.*, 2003; Raaijmakers & Weller, 2007). However, among all *At*-RSphere *Pseudomonas spp.* isolates, exometabolite-mediated antagonism is least pronounced in R9 (**Chapter I**), indicating that this strain used alternative modes of action to supress fungi *in vitro* and *in planta*. Taken together, our binary interaction data corroborated prior findings from complex SynCom-inoculated *A. thaliana* seedlings and identified R9 as a highly antagonistic strain, making it an attractive target for identification of putatively novel phytoprotective mechanisms.

In natural soils, diverse bacteria, mainly belonging to the Phylum of Proteobacteria, associate with fungal mycelia (*i.e.*, the hyphosphere), forming bacterial communities that are structurally distinct from bulk soil (Emmett *et al.*, 2021; Hervé *et al.*, 2014; Warmink *et al.*, 2009). For example, the hyphosphere of the basidiomycete *Laccaria proxima* enriches for Proteobacteria that proliferate to higher bacterial titres than in the bulk soil (Nazir *et al.*, 2010). Similarly, our data demonstrates higher bacterial proliferation – mainly of Proteobacteria – in soil, when co-inoculated with either of the four tested fungal species. Collectively, this suggests that taxonomically diverse fungi can sustain and support bacterial growth in soils, where easily accessible carbon is limited. Whether or how this interaction benefits the fungi remains unclear. Our data shows that the presence of individual bacterial taxa has neutral-to-negative effects on fungal proliferation in soil, indicating a unidirectionally beneficial relationship. This suggests a multi-layered trophic network involving a primary layer of saprophytic fungi as degraders of complex soil detritus and mycoparasitic bacteria as a secondary layer proliferating on either fungal exudates or hyphal components in unplanted soil. At the soil-root interface, microbes are facing altered nutritional regimes as plants invest significant amounts of the photosynthetically acquired carbon into the rhizosphere (Eilers *et al.*, 2010; Ling *et al.*, 2022; Wippel *et al.*, 2021). While such exudates have microbiota-independent functions in, *e.g.*, nutrient mobilisation (Chen *et al.*, 2017; Dakora & Phillips, 2002; McKay Fletcher *et al.*, 2020), our data suggests that root exudates modulate intra- and interkingdom competition,

putatively resulting in reducing diversity and suppressing bacterial and fungal pathogens at roots (as for *Ralstonia solanacearum*, **Chapter I**). In this way, root exudates likely constitute a metabolic currency that fosters root microbiota-mediated host protection in the rhizosphere.

In conclusion, we have generated a framework for future mechanistic studies on the *Arabidopsis* core microbiome by establishing an ecologically relevant and functional minimal synthetic community. We validated correlative microbial interaction networks by establishing a comprehensive binary interaction assay that allows simultaneous quantification of both interaction partners. We could demonstrate that cooperative and competitive interactions between bacteria and fungi are highly modulated by the nutritional status, thereby suggesting that carbon-rich conditions encountered at the root vicinity likely promote competitive interactions, which were not observed in the soil-like peat matrix.

III.6 Material and methods

III.6.1 Data and script availability

All data and code generated for this study will be deposited on public databases upon publication of this chapter in a scientific journal. All primers used in this study can be found in **Table S11**.

III.6.2 Selection of minimal synthetic community (MiniSynCom)

MiniSynCom establishment followed predefined criteria. First, we aimed to establish a SynCom that recapitulates the taxonomic distribution at class-level as found associated with *Arabidopsis* roots across a European transect (Thiergart *et al.*, 2019). For each bacterial or fungal class, we identified the most prevalent ASV that has a representative isolate present in the respective bacterial or fungal culture collections (Bai *et al.*, 2015; Durán *et al.*, 2018) matching at a 100% *16S* v5v7 or ITS1 region sequence identity, respectively. We only selected isolates that were initially isolated from *Arabidopsis thaliana* roots grown in Cologne agricultural soil and had been whole genome sequenced. We ensured that all strains of the MiniSynCom can be differentiated based on their *16S* v5v7 or ITS1 regions by at least four mismatches. To increase taxonomic and presumably functional diversity, we selected only one isolate per microbial family, except for Pseudomonadaceae, due to their high prevalence at *Arabidopsis* roots.

III.6.3 PacBio sequencing and assembly of bacterial genomes

Long-read sequencing and assembly of bacterial genomes was conducted as described in **Chapter I** of this thesis.

III.6.4 In silico assessment of phylogenetic and genomic SynCom traits

All bacterial genomes were retrieved from the *At*-Sphere "www.at-sphere.com" (Bai *et al.*, 2015). Genomes from random 11-member SynComs and from the MiniSynCom were compiled. These SynComs were compared regarding phylogenetic distance and overlap in predicted metabolic pathways, as described in (Mataigne *et al.*, 2022). In brief, phylogenetic

distances were computed using the ete toolkit based on the species tree on the *At*-Sphere website (Huerta-Cepas *et al.*, 2016). Union and intersect of interactions were computed based on the genomes for predicting capabilities for producing defined vitamins, amino-acids, and phytohormones (Mataigne *et al.*, 2022).

III.6.5 Microbial culture conditions

The bacterial and fungal strains used in this study were initially isolated from *A. thaliana* roots grown in Cologne agricultural soil (Bai *et al.*, 2015; Durán *et al.*, 2018, respectively) and are summarized in **Table S10**. Bacteria were cultured as described before (**Chapter I**). Individual pieces of fungal mycelium were transferred to potato dextrose agar (PDA; Sigma-Aldrich) Petri dishes from glycerol stocks (approx. 30 pieces of fungal mycelium in 25% sterile glycerol, stored at -80 °C). Fungi were grown at 25 °C in the dark for 14 days. For the inoculation of any experimental system, fungal mycelium was carefully harvested from PDA Petri dishes using sterile scalpels and the agar was fully removed. Pieces of mycelium were transferred to pre-weighed sterile 2 ml screw cap tubes containing one and approx. 15 steel beads of 3 mm and 1 mm diameter, respectively. Per 50 mg harvested fungal mycelium, 500 µl of sterile 10 mM $MgCl_2$ were added. The mycelium was subsequently grinded in a paint shaker at approx. 600 rpm for at least 10 min until homogeneous. The resulting slurry was diluted and used as fungal inoculum. Viability of ground mycelium was assessed by plating a few microlitres on PDA plates.

III.6.6 Gnotobiotic Flowpot experiments

Peat sterilisation and Flowpot assembly were performed as described before (**Chapter I**). Arabidopsis thaliana Col-0 (N60000, the Nottingham Arabidopsis Stock Centre) seeds were sterilized using 70% ethanol and bleach. Seeds were submerged in 70% ethanol and left shaking at 40 rpm for 14 minutes. Ethanol was removed before the seeds were submerged in 8.3% sodium hypochlorite (Roth) containing 1 µl of Tween 20 (Sigma-Aldrich) and left shaking at 40 rpm for 4 minutes. Under sterile conditions, the seeds were washed 7x times and finally taken up with sterile 10 mM $MgC1_2$. Seeds were left for stratification at 4 °C for 3 days. Seed sterility was confirmed by plating approx. 100 seeds on a 50% TSA plate. Microbes were grown and inocula were prepared as described above. Each Flowpot was inoculated with 50 ml half strength Murashige and Skoog medium with vitamins (½ MS; 2.2 g/l, Duchefa Biochemie,

0.5 g/l MES, pH 5.7). For bacteria, a final OD_{600} of 0.0025 and for fungi 0.16 mg/ml in 50 ml ½ MS were inoculated per Flowpot. For salt stress treatment, ½ MS contained 100 mM NaCl. Per Flowpot, five surface-sterilized and stratified *A. thaliana* Col-0 seeds were pipetted. Microboxes were then incubated in a light cabinet under short day conditions (10 h light at 21 °C, 14 h dark at 19 °C) for 14 days and randomized every 2–3 days. For low PAR treatments, microboxes were partly covered in cardboard boxes, as described in Hou *et al.*, (2021).

III.6.7 Ex planta quantitative abundance workflow establishment

Full MSC (bacteria and fungi) inoculated peat was harvested from 4-week-old Flowpots, followed by DNA isolation, as described below. All utilized samples stem from the same condition. Prior to DNA isolation, increasing concentrations of spike (BI-124, Guo *et al.*, 2020) were added to the samples. We applied five different concentrations of spike, $2x10^2$, $2x10^3$, $2x10^4$, $2x10^5$, $2x10^6$ copies of spike per 3.5 ng/µl sample DNA, to the DNA samples. For the lowest two spike concentrations, barely any spike reads were detectable after amplicon sequencing; these were therefore excluded from further analyses. Additionally, we added 0.35 ng of Root401 (Bai *et al.*, 2015) and 0.175 ng of F100 (Durán *et al.*, 2018) genomic DNA per µl of sample DNA to some of the samples.

III.6.8 Preparation of 96-well plates containing peat

Peat (Profi Substrat, Einheitserde) was dried at 80 °C for 5 d and sieved until a final particle size of 400 µm was obtained. Then, 100 mg of peat were distributed to each well of a riplate low profile 0.6 ml 96-deep well microtiterplate (Ritter). The peat was moistened using 100 µl of Milli-Q water per well. After centrifuging the plate for 1 min at 1500 rpm, excessive soil particles were removed from the top of the plate using compressed air. The lid of a pipette tip box (200 µl tips, TipOne) was placed on top of the plate and the construction was sealed in a sun bag (Sigma-Aldrich). Subsequently, the plate was autoclaved in a liquid autoclaving program for 20 min, left at room temperature for 24 h to ensure germination of surviving microbial spores (Kremer *et al.*, 2021) and autoclaved again in a dry autoclaving program. Subsequently, the plates were dried at 80 °C for approx. 5 d. Dried plates were stored at room temperature until further use.

III.6.9 Binary interaction screen in ARE and peat

ARE medium and peat plates were prepared as described before (**Chapter I** and see above, respectively). Bacteria and fungi were cultured, washed, and harvested as described above. Subsequently, bacteria and fungi were taken up in both ARE and ½ MS, as ARE and peat plates were inoculated in parallel. For both media, pairs of microbes were distributed into a predefined, randomized setup into 96-well plates with a final OD_{600} of 0.02 per bacterium or 0.001 mg/µl per of fungus with a total final volume of 100 µl per well. Either two microbes or a single microbe, as reference condition, were inoculated per well. After the inoculation, all plates were spun down in a swingout centrifuge at 1,500 rpm for 1 min and sealed with breath-easy foil that ensures gas exchange during the experimental duration. All plates were cultured at 25 °C for 2 or 14 days, for ARE and peat plates, respectively. The experimental duration for each medium was predetermined in preliminary experiments. At the end of the experiment, plates were frozen at -80 °C until further processing.

III.6.10 DNA isolation from ARE and peat

Bacterial and fungal DNA was isolated from Flowpot peat as described before (**Chapter I**). Similarly, DNA from 96-well plates containing peat was isolated; however, the initial lysis step was not conducted in individual tubes. In brief, four and one steel beads of a diameter of 1 mm or 3 mm, respectively, and 200 µl extraction buffer (176 µl sodium-phosphate buffer and 22 µl MT buffer; MP Biomedicals and 0.3 ng of BI-124 spike; Guo *et al.*, 2020) were added to each well. Then, the plate was sealed and crushed at 1800 rpm for 10 min in a bead beater (Retsch). The soil debris was pelleted by centrifugation at 4000 rpm for 10 min. 150 µl of the supernatant were taken into a 96-well filter plate (Acroprep Advance, 0.2 µm Supor filter, Pall) to filter the SN from remaining soil particles. The remaining protocol was carried out as described in **Chapter I**. For ARE, four steel-beads of 1 mm diameter were added to each well, the plate was sealed and crushed at 1800 rpm for 10 min in a bead beater (Retsch). Then, DNA was isolated two times per plate with two 0.22 pg or 0.05 pg circular BI-124 spike (Guo *et al.*, 2020) per well for subsequent amplification of bacterial and fungal amplicons, respectively. The spike was directly added to extraction buffer I (containing 25 mM NaOH, 0.2 mM EDTA; pH 12). For DNA extraction, 15 µl buffer I containing the spike were added to 9 µl bacterial and fungal lysate and heated at 95 °C for 30 min, before the pH was readjusted using 30 µl of buffer II (pH 7.5) containing 40 mM Tris-HCl. This crude DNA extract served as PCR template for amplification of bacterial and fungal marker gene regions.

III.6.11 Amplicon sequencing library preparation

Bacterial *16S* v5v7 and fungal ITS1 regions were amplified as described before (**Chapter I**) using 1 µl of DNA as template. All utilized primers can be found in **Table S11**. Amplicons were purified using AMPure XP (Beckman-Coulter) magnetic beads and then equimolarly and sequentially pooled by PCR plate, marker gene and library. Paired-end Illumina sequencing was performed in-house using the MiSeq sequencer and custom sequencing primers (**Table S11**).

III.6.12 Amplicon sequencing - data analysis

Paired rRNA amplicon sequencing reads were analysed as described before (Hou *et al.*, 2021). In brief, paired amplicon sequencing reads were joined, demultiplexed and quality-filtered using Qiime (Caporaso *et al.*, 2010) and subsequently trimmed to equal length. Reference sequences for all used strains were retrieved and trimmed from the respective genomes. Mapping of trimmed sequencing reads to the trimmed reference sequences was conducted using usearch (Edgar & Bateman, 2010), allowing for two mismatches. Unmapped reads were discarded. Count tables were generated from these mapping results. BI-124 spike (Guo *et al.*, 2020) read counts were initially used to normalize microbial read counts and then depleted from any further analyses. To obtain foldchanges of microbial abundances (*i.e.*, effector and target scores), abundances of strains grown in strain pairs were normalized by the abundance of the respective strain growing in axenic, reference conditions (see **Fig. S2E**). These fold changes were subsequently $\log_2$-transformed.

III.6.13 antiSMASH predictions and modified Burkholder assay data

antiSMASH (Blin *et al.*, 2021) predictions and data from modified Burkholder assay experiments are derived from **Chapter I**.

III.6.14 Microbial growth rate validation

Assessment of microbial growth rates was conducted as described before (**Chapter I**). For bacteria and fungi, the starting inocula were OD_{600} 0.02 and 0.001 mg/µl ARE, respectively.

Growth rates were determined using the Growthcurver R package (Sprouffske & Wagner, 2016).

III.6.15 Statistical analyses

All statistical analyses were conducted in R 4.1.2. Data visualisation was conducted using the ggplot2 package (as part of the Tidyverse). Data normality was tested using the Shapiro-Wilk test. As nonparametric tests, Kruskal-Wallis followed by Dunn's post-hoc test and Benjamini-Hochberg (BH) adjustment for multiple comparisons from the PMCMRplus package (Pohlert, 2022) were used. The respective statistical tests are indicated in each figure description. Significance was indicated by significance group ($p \leq 0.05$). No statistical methods were used to pre-determine sample sizes. Phylogenetic trees were computed using Clustal Omega (Madeira *et al.*, 2022) and subsequently visualised using iTol (Letunic & Bork, 2021). *16S* rRNA gene profiling data were analysed and visualized as described above. Networks were generated using Cytoscape (Shannon *et al.*, 2003). Figures were assembled in Adobe Illustrator.

III.7 Acknowledgements

This work was supported by funds to S.H. from a European Research Council starting grant (MICRORULES 758003) and the Max Planck Society, as well as the Cluster of Excellence on Plant Sciences (CEPLAS) and the Priority Program: Deconstruction and Reconstruction of the Plant Microbiota (SPP DECRyPT 2125; project HA 8169/2-2), both funded by the Deutsche Forschungsgemeinschaft. We thank the Max Planck-Genome-Centre Cologne for advising and performing the genome resequencing. We also thank Brigitte Pickel for her support in Flowpot harvest. Finally, thanks to Neysan Donnelly for editing this chapter and Saurabh Pophaly for support with ENA and NCBI data submission.

III.8 Supplementary figures

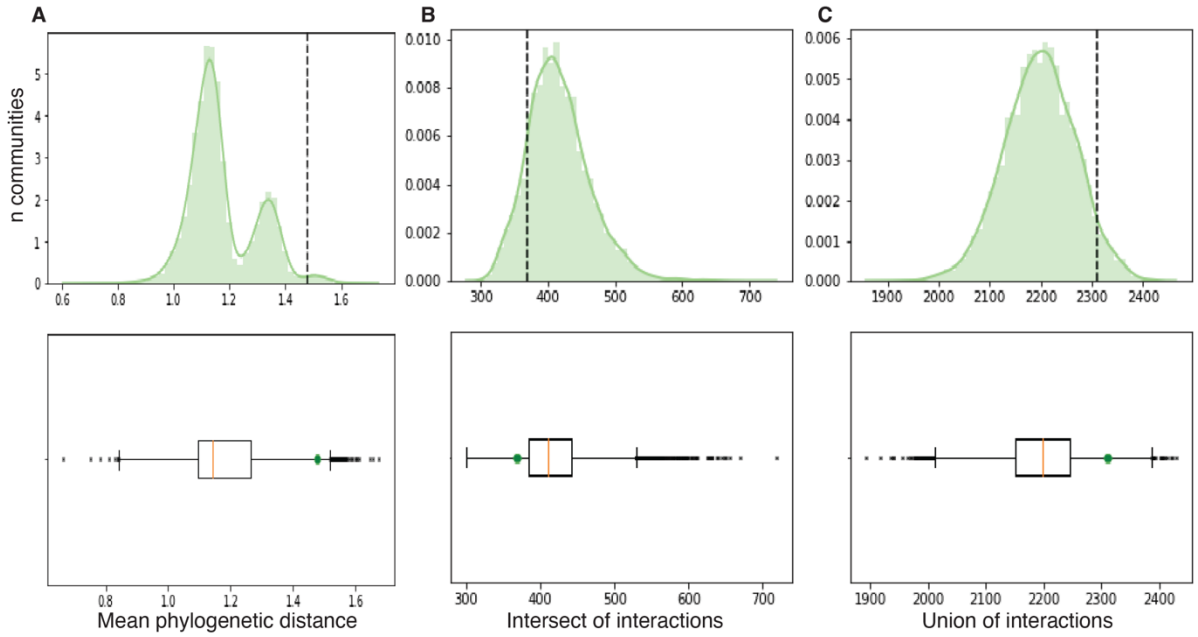

Figure S1 related to Figure 1, Bacteria within the MiniSynCom are highly phylogenetically and genetically diverse. (A–C) Genome-based comparisons of the 11-member bacterial fraction of the MiniSynCom and randomly generated 11-member SynComs, based on *At*-RSphere genomes. The upper and lower panels represent the same data as density curves and boxplots, respectively. The 11-member bacterial fraction of the MiniSynCom is indicated by a dashed line or green dot, in the upper and lower panels, respectively. **(A)** Mean of whole genome phylogenetic distance between each member of randomly generated 11-member SynComs. **(B)** Intersect of interactions, *i.e.*, overlap between metabolic reactions between the genomes within randomly generated 11-member SynComs. **(C)** Union of interactions, *i.e.*, number of total existing metabolic reactions, within all genomes of randomly generated 11-member SynComs.

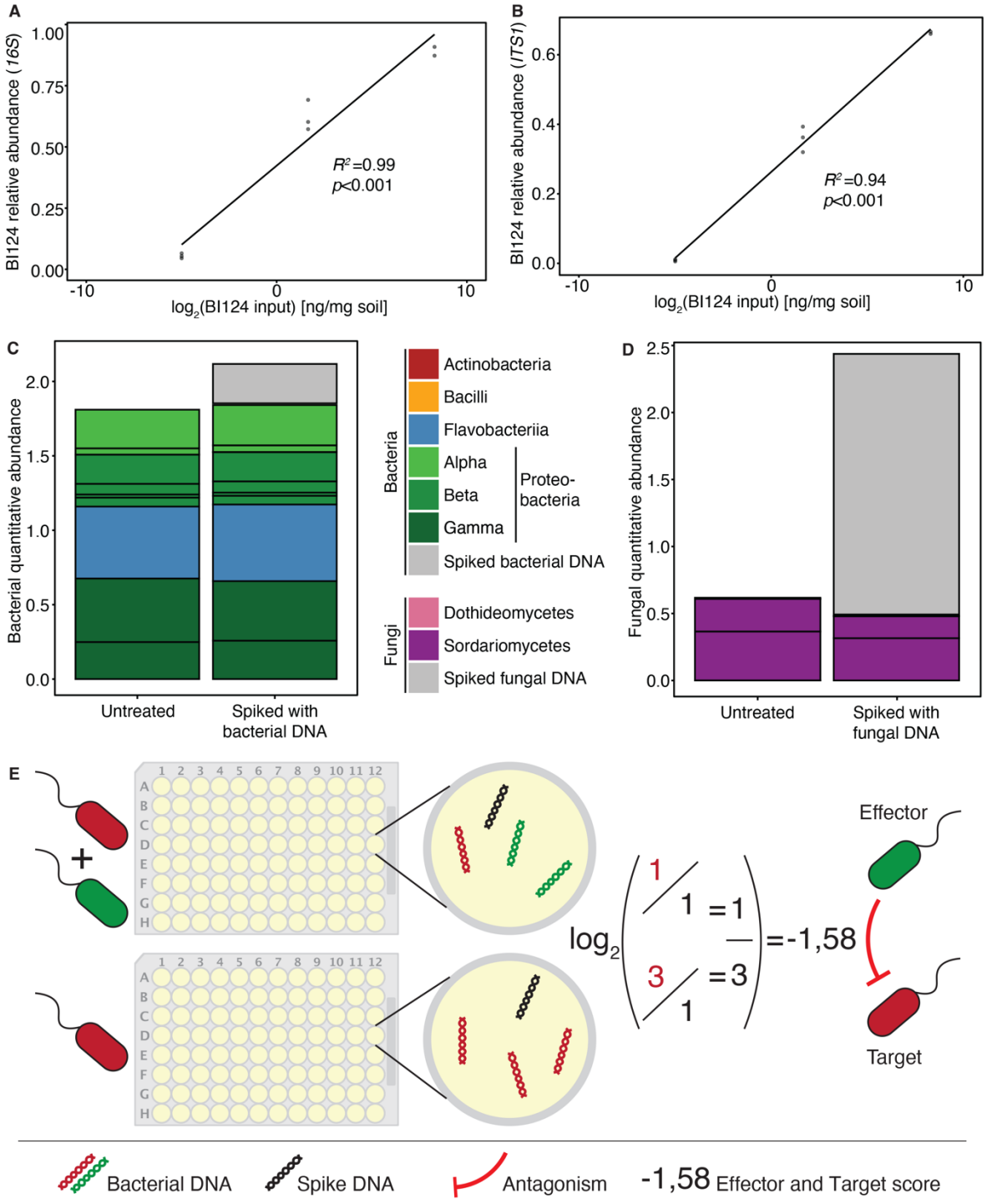

Figure S2 related to Figure 3 and 4, Spike-based assessment of quantitative microbial abundance *ex planta*. **(A–B)** Regression analysis between spike input and spike relative abundance in soil samples when amplifying the bacterial *16S* rRNA v5v7 **(A)** or the fungal ITS1 region **(B)**. *p*-values and R^2 derive from linear models. **(C–D)** Spike-normalized quantitative abundance of bacterial **(C)** and fungal **(D)** soil communities remains stable upon artificial introduction of bacterial or fungal DNA (light grey) prior to amplicon sequencing library establishment. Sub-bars represent the quantitative abundance of individual bacteria **(C)** or fungi **(D)** and are coloured by taxonomy. **(E)** Schematic representation of the spike-based normalisation of microbial relative abundances *ex planta* that has been deployed for the binary interaction screen.

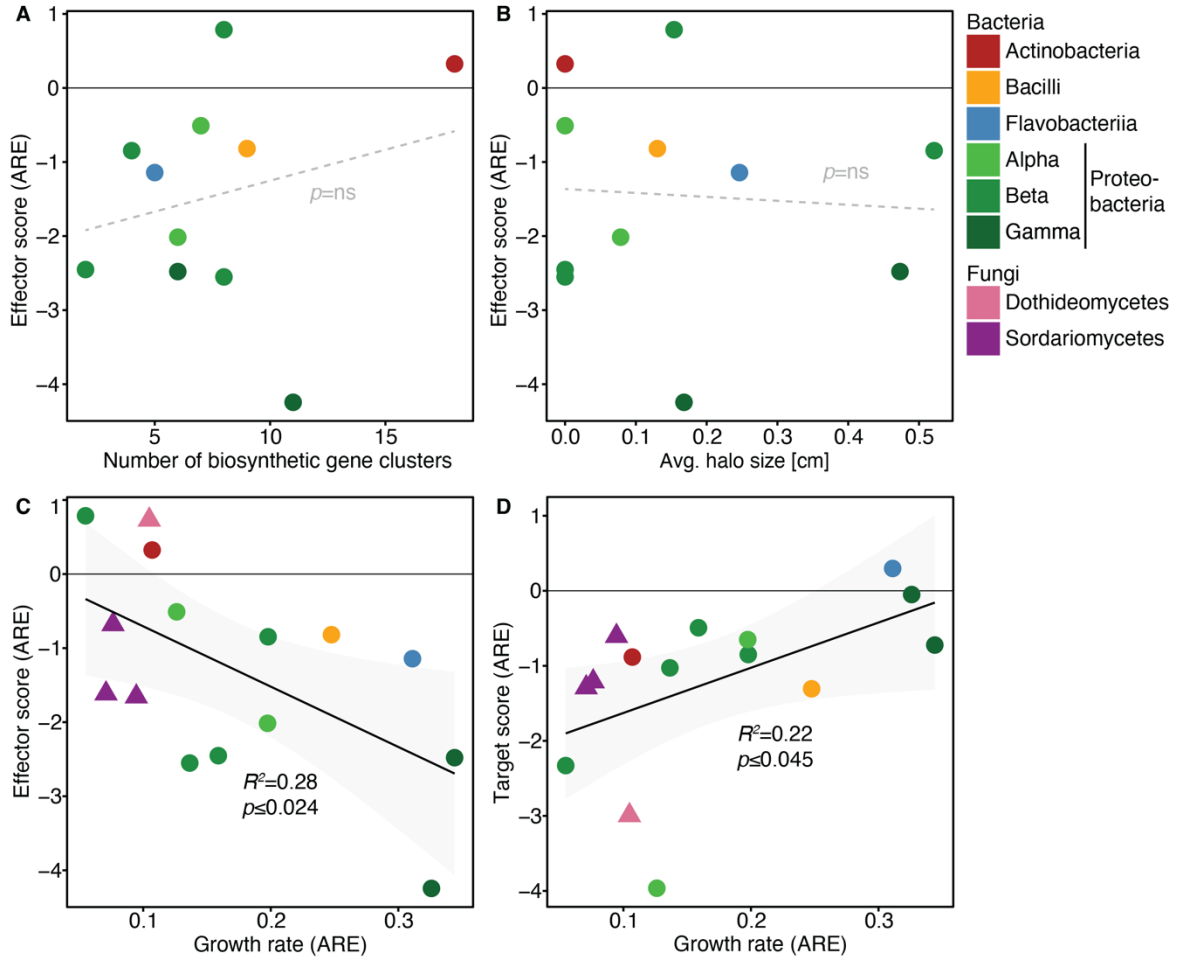

Figure S3 related to Figure 3, Microbial growth speed explains observed interaction profiles. (A–B) Regression analysis of number of antiSMASH predicted biosynthetic gene clusters **(A)** and average halo size as producer strain in binary interaction Burkholder assay experiment **(B)** with bacterial effector scores in ARE, as in **Fig. 3**. Using linear models, no significant association was found, as indicated by 'ns'. Biosynthetic gene cluster and Burkholder assay data derived from **Chapter I**. **(C–D)** Regression analysis of microbial growth rates under axenic conditions with effector **(C)** and target **(D)** scores. Growth rates, effector and target scores have all been determined in ARE. *p*-values and R^2 derive from linear models.

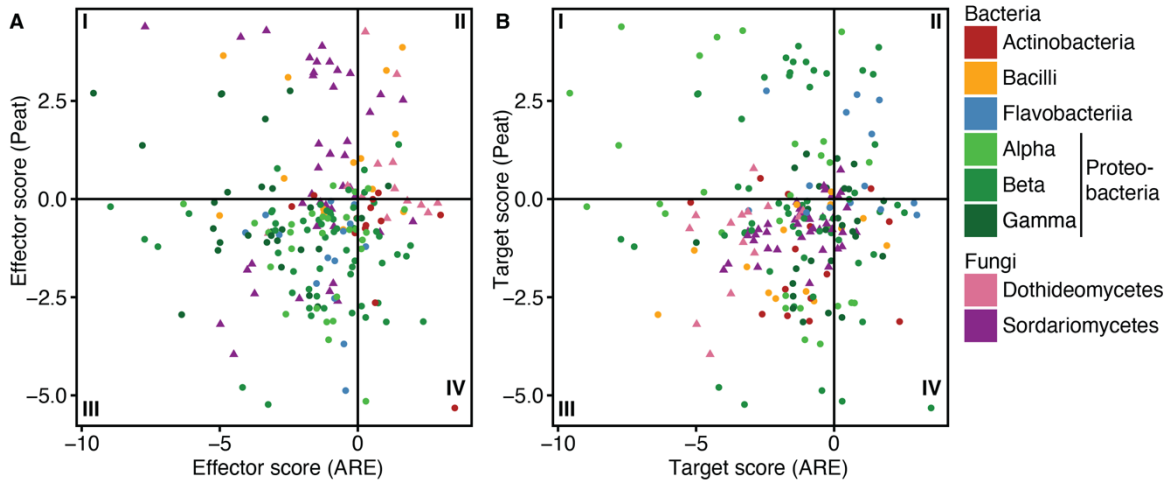

Figure S4 related to Figure 3 and 4, Effector scores of ARE and peat substantially overlap qualitatively. **(A–B)** Mean effector **(A)** or target **(B)** scores for each microbial combination have been computed for ARE and peat samples and plotted against each other. Dot colour depicts microbial classes, while dot shape indicates affiliation to either the bacterial (circle) or fungal (triangle) kingdom of effector **(A)** or target **(B)** strains. The different quadrants of the plot are indicated by roman numbers **(I–V)**. **(I)**, positive effect in ARE and negative effect in peat; **(II)** and **(III)**, similar qualitative effector score in ARE and Peat; **(IV)**, negative effect in ARE and positive effect in peat.

III.9 Supplementary tables

Table S10, Microorganisms used in this study

Table S11, Primers used in this study

All supplementary tables have been deposited at EDMOND and can be accessed *via* the following link: https://doi.org/10.17617/3.I1ABIM

General discussion:

Immense efforts to characterise the microbiota composition of aerial and subterranean organs of diverse plant species and the associated rhizospheres and bulk soils in various natural and agricultural environments have unrevealed the diversity of microbial species that robustly associate with plant tissues all over the world (Agler *et al.*, 2016; Bulgarelli *et al.*, 2015; Coleman-Derr *et al.*, 2016; Cregger *et al.*, 2018; Lundberg *et al.*, 2012; Thiergart *et al.*, 2019; Zgadzaj *et al.*, 2016). Such approaches however remain largely descriptive and rarely allow for the establishment of cause-consequence relationships in such highly complex systems. Subsequent efforts to isolate pure microbial cultures from roots of the model plant *Arabidopsis thaliana* revealed cultivability of especially highly abundant bacterial and fungal species that collectively constitute most of the root-associated microbial diversity (Bai *et al.*, 2015; Duran *et al.*, 2018; Karasov *et al.*, 2018; Levy *et al.*, 2017; Wippel *et al.*, 2021). Microbiota reconstitution experiments with defined – yet complex – synthetic microbial communities (SynComs) allowed for direct manipulation of ecological properties enabling the establishment of causal relationships between the presence of microbial taxa with community function and host health (Bai *et al.*, 2015; Duran *et al.*, 2018; Hou *et al.*, 2021; Wolinska *et al.*, 2021).

During my PhD, I intended to extend this knowledge with a focus on microbial interactions in the *A. thaliana* root microbiota and particularly with the aim of unrevealing microbial genetic determinants that affect root microbiota establishment and host health. I reasoned that the mechanistic assessment of microbe-microbe interactions *in planta*, requires tractable systems with defined, minimal microbial consortia that reduce functional redundancy and allow for genetic manipulation of individual microbiota members. Therefore, I established and utilized various genetic tools, including random transposon-mediated mutagenesis allowing for forward genetic screens, targeted mutagenesis, and genetic complementation approaches. Coupled, with microbiota reconstitution experiments in gnotobiotic systems, these approaches enabled us to experimentally test the involvement of secreted bacterial secondary metabolites (exometabolites) for microbiota establishment. Although, the involvement of bacterial exometabolites in pathogen protection and thereby microbe-microbe interactions has been described before (*e.g.*, Dimkic *et al.*, 2017; Dimkić *et al.*, 2022; Gu, Wei, *et al.*, 2020; Gu, Yang, *et al.*, 2020; Osbourn, 1996; Raaijmakers & Weller, 1998), we provide first evidence for their root-specific functioning in microbial communities. We demonstrate that the antimicrobial 2,4-Diacetylphloroglucinol (DAPG) and the siderophore pyoverdine have cumulative functions

as community-specific root competence determinants for the producer strain *Pseudomonas brassicacearum* Root401 (R401) by directly inhibiting sensitive community members and thereby affecting microbial diversity and community structure. The enrichment of the biosynthetic gene clusters (BGCs) encoding DAPG and pyoverdine biosynthetic genes in root-derived compared to leaf-derived *Pseudomonas spp.* isolates across different culture collections, further reinforces a root-specific functioning, and indicates modulation of microbe-microbe interactions by the host. The isolation of DAPG- and pyoverdine-producing pseudomonads from diverse host plants suggests a general principle beyond the model plant *A. thaliana*.

Furthermore, we identified the non-ribosomal peptide Brassicapeptin A produced by *P. brassicacearum* R401 as causal for the detrimental activity of R401 towards *A. thaliana* (Ma *et al.*, 2021). We demonstrate that Brassicapeptin A in combination with hyperosmotic conditions in the rhizosphere is required and sufficient to cause plant disease. Application of purified Brassicapeptin A resulted in ion leakage from *A. thaliana* tissues, suggesting that it caused imbalances in host ion homeostasis when challenged with an osmotic stress. In the absence of microbial competitors, Brassicapeptin production provided a root-specific benefit for R401 under hyperosmotic conditions, indicating that it functions as a root competence determinant by potentially allowing for increased leaking of carbon rich root solutes. Brassicapeptin A furthermore contributes to the remarkable antimicrobial activity we described for R401. Isolation of Brassicapeptin A from axenic R401 liquid cultures, demonstrates production in the absence of hyperosmotic stress. Therefore, it is likely Brassicapeptin, similarly to DAPG and pyoverdine, would provide a competitive advantage to R401 in the presence of competitors, even in the absence of hyperosmotic stress. This suggests a putative dual function of bacterial exometabolites in competition with other host-associated microorganisms and in host health.

Finally, I established multiple tools that facilitate synthetic ecology, including a minimal SynCom (MiniSynCom) that comprises some of the most prevalent bacterial and fungal strains found associated with *A. thaliana* roots across a European transect thereby likely constituting the *A. thaliana* core microbiota. This MiniSynCom is sufficient to reproduce microbiota functions of complex communities, suggesting that the core microbiota is sufficient for the protective activity of the root microbiota towards biotic and abiotic stresses. I also established a quantitative abundance-based binary interaction screen workflow, enabling simultaneous assessment of all interaction partners. This allowed for systematic characterisation of all

competitive and cooperative binary intra- and interkingdom interactions within the MiniSynCom, primarily revealing competition between root microbiota members. We demonstrate nutrient competition as predominant mechanism driving binary interactions between members of the *A. thaliana* core root microbiota. Collectively, this suggests that competition for nutrients drives competition between root microbiota members.

In conclusion, our data demonstrates that microbial interactions – as mediated by bacterial exometabolites – frequently occur between root-derived bacterial isolates. We provide genetic evidence that multiple exometabolites produced by *Pseudomonas brassicacearum* R401 cumulatively influence ecological properties of the root microbiota and function as root competence determinants in a community context. Given favourable environmental conditions, a single bacterial exometabolite is sufficient to modulate plant ion homeostasis with cascading consequences for host health. Collectively, this illustrates the functional diversity of bacterial exometabolites with involvement in microbe-microbe and plant-microbe interactions and demonstrates the fine line between a suitable biocontrol strain and an opportunistic pathogen, depending on environmental conditions.

References

Acosta-Motos, J. R., Ortuño, M. F., Bernal-Vicente, A., Diaz-Vivancos, P., Sanchez-Blanco, M. J., & Hernandez, J. A. (2017). **Plant Responses to Salt Stress: Adaptive Mechanisms.** *Agronomy 2017, Vol. 7, Page 18*, *7*(1), 18.

Adachi, H., Derevnina, L., & Kamoun, S. (2019). **NLR singletons, pairs, and networks: evolution, assembly, and regulation of the intracellular immunoreceptor circuitry of plants.** *Current Opinion in Plant Biology*, *50*, 121–131.

Agler, M. T., Ruhe, J., Kroll, S., Morhenn, C., Kim, S. T., Weigel, D., & Kemen, E. M. (2016). **Microbial Hub Taxa Link Host and Abiotic Factors to Plant Microbiome Variation.** *PLOS Biology*, *14*(1), e1002352.

Aldon, D., Brito, B., Boucher, C., & Genin, S. (2000). **A bacterial sensor of plant cell contact controls the transcriptional induction of Ralstonia solanacearum pathogenicity genes**. *The EMBO Journal*, *19*(10), 2304.

Almario, J., Jeena, G., Wunder, J., Langen, G., Zuccaro, A., Coupland, G., & Bucher, M. (2017). **Root-associated fungal microbiota of nonmycorrhizal Arabis alpina and its contribution to plant phosphorus nutrition.** *Proceedings of the National Academy of Sciences of the United States of America*, *114*(44), E9403–E9412.

Altschul, S. F., Gish, W., Miller, W., Myers, E. W., & Lipman, D. J. (1990). **Basic local alignment search tool.** *Journal of Molecular Biology*, *215*(3), 403–410.

Aron, A. T., Gentry, E. C., McPhail, K. L., Nothias, L. F., Nothias-Esposito, M., Bouslimani, A., Petras, D., Gauglitz, J. M., Sikora, N., Vargas, F., van der Hooft, J. J. J., Ernst, M., Kang, K. bin, Aceves, C. M., Caraballo-Rodríguez, A. M., Koester, I., Weldon, K. C., Bertrand, S., Roullier, C., Dorrestein, P. C. (2020). **Reproducible molecular networking of untargeted mass spectrometry data using GNPS.** *Nature Protocols 2020 15:6*, *15*(6), 1954–1991.

Arora, N. K., & Verma, M. (2017). **Modified microplate method for rapid and efficient estimation of siderophore produced by bacteria**. *3 Biotech*, *7*(6).

Ashraf, M., & Harris, P. J. C. (2004). **Potential biochemical indicators of salinity tolerance in plants.** *Plant Science*, *166*(1), 3–16.

Bahram, M., Hildebrand, F., Forslund, S. K., Anderson, J. L., Soudzilovskaia, N. A., Bodegom, P. M., Bengtsson-Palme, J., Anslan, S., Coelho, L. P., Harend, H., Huerta-Cepas, J., Medema, M. H., Maltz, M. R., Mundra, S., Olsson, P. A., Pent, M., Põlme, S., Sunagawa, S., Ryberg, M., Bork, P. (2018**). Structure and function of the global topsoil microbiome.** *Nature 2018 560:7717*, *560*(7717), 233–237.

Bai, Y., Müller, D. B., Srinivas, G., Garrido-Oter, R., Potthoff, E., Rott, M., Dombrowski, N., Münch, P. C., Spaepen, S., Remus-Emsermann, M., Hüttel, B., McHardy, A. C., Vorholt, J. A., & Schulze-Lefert, P. (2015). **Functional overlap of the Arabidopsis leaf and root microbiota**. *Nature 2015 528:7582*, *528*(7582), 364–369

Bakker, P. A. H. M., Glandorf, D. C. M., Viebahn, M., Ouwens, T. W. M., Smit, E., Leeflang, P., Wernars, K., Thomashow, L. S., Thomas-Oates, J. E., Leendert, &, & van Loon, C. (2002). **Effects of Pseudomonas putida modified to produce phenazine-1-carboxylic acid and 2,4-diacetylphloroglucinol on the microflora of field grown wheat.** *Antonie van Leeuwenhoek*, *81*, 617–624.

Bakshi, M., Vahabi, K., Bhattacharya, S., Sherameti, I., Varma, A., Yeh, K. W., Baldwin, I., Johri, A. K., & Oelmüller, R. (2015). **WRKY6 restricts Piriformospora indica-stimulated and phosphate-induced root development in Arabidopsis**. *BMC Plant Biology*, *15*(1), 1–19.

Baudoin, E., Benizri, E., & Guckert, A. (2003). **Impact of artificial root exudates on the bacterial community structure in bulk soil and maize rhizosphere.** *Soil Biology and Biochemistry*, *35*(9), 1183–1192.

Bensaci, M. F., & Takemoto, J. Y. (2007). **Syringopeptin SP25A-mediated killing of gram-positive bacteria and the role of teichoic acid d-alanylation.** *FEMS Microbiology Letters*, *268*(1), 106–111.

Bionda, N., Pitteloud, J. P., & Cudic, P. (2013). **Cyclic lipodepsipeptides: a new class of antibacterial agents in the battle against resistant bacteria.** *Future Medicinal Chemistry*, *5*(11), 1311–1330.

Blin, K., Shaw, S., Kloosterman, A. M., Charlop-Powers, Z., van Wezel, G. P., Medema, M. H., & Weber, T. (2021). **antiSMASH 6.0: improving cluster detection and comparison capabilities.** *Nucleic Acids Research*, *49*(W1), W29–W35.

Bolger, A. M., Lohse, M., & Usadel, B. (2014). **Trimmomatic: a flexible trimmer for Illumina sequence data**. *Bioinformatics*, *30*(15), 2114.

Boucher, A., Boucher, A., Barberis, P. A., Ph, A., Trigalet, & Demery, D. A. (1985). **Transposon mutagenesis of Pseudomonas solanacearum: isolation of Tn5induced avirulent mutants**. 131--2449.

Brakhage, A. A. (2013). **Regulation of fungal secondary metabolism**. *Nature Reviews. Microbiology*, *11*(1), 21–32.

Bulgarelli, D., Garrido-Oter, R., Münch, P. C., Weiman, A., Dröge, J., Pan, Y., McHardy, A. C., & Schulze-Lefert, P. (2015). **Structure and function of the bacterial root microbiota in wild and domesticated barley**. *Cell Host & Microbe*, *17*(3), 392–403.

Bulgarelli, D., Rott, M., Schlaeppi, K., ver Loren van Themaat, E., Ahmadinejad, N., Assenza, F., Rauf, P., Huettel, B., Reinhardt, R., Schmelzer, E., Peplies, J., Gloeckner, F. O., Amann, R., Eickhorst, T., & Schulze-Lefert, P. (2012). **Revealing structure and assembly cues for Arabidopsis root-inhabiting bacterial microbiota.** *Nature 2012 488:7409*, *488*(7409), 91–95.

Burkholder, P. R., Pfister, R. M., & Leitz, F. H. (1966). **Production of a Pyrrole Antibiotic by a Marine Bacterium.** *Applied Microbiology*, *14*(4), 649.

Caporaso, J. G., Kuczynski, J., Stombaugh, J., Bittinger, K., Bushman, F. D., Costello, E. K., Fierer, N., Pẽa, A. G., Goodrich, J. K., Gordon, J. I., Huttley, G. A., Kelley, S. T., Knights, D., Koenig, J. E., Ley, R. E., Lozupone, C. A., McDonald, D., Muegge, B. D., Pirrung, M., Knight, R. (2010). **QIIME allows analysis of high-throughput community sequencing data.** *Nature Methods*, *7*(5), 335–336.

Carbon, S., Dietze, H., Lewis, S. E., Mungall, C. J., Munoz-Torres, M. C., Basu, S., Chisholm, R. L., Dodson, R. J., Fey, P., Thomas, P. D., Mi, H., Muruganujan, A., Huang, X., Poudel, S., Hu, J. C., Aleksander, S. A., McIntosh, B. K., Renfro, D. P., Siegele, D. A., Westerfield, M. (2017). **Expansion of the Gene Ontology knowledgebase and resources**. *Nucleic Acids Research*, *45*(D1), D331–D338.

Carlström, C. I., Field, C. M., Bortfeld-Miller, M., Müller, B., Sunagawa, S., & Vorholt, J. A. (2019). **Synthetic microbiota reveal priority effects and keystone strains in the Arabidopsis phyllosphere.** *Nature Ecology & Evolution*, *3*(10), 1445–1454.

Carrión, V. J., Perez-Jaramillo, J., Cordovez, V., Tracanna, V., de Hollander, M., Ruiz-Buck, D., Mendes, L. W., van Ijcken, W. F. J., Gomez-Exposito, R., Elsayed, S. S., Mohanraju, P., Arifah, A., van der Oost, J., Paulson, J. N., Mendes, R., van Wezel, G. P., Medema, M. H., & Raaijmakers, J. M. (2019). **Pathogen-induced activation of disease-suppressive functions in the endophytic root microbiome.** *Science*, *366*(6465), 606–612.

Cartwright, D. K., Chilton, W. S., & Benson, D. M. (1995). **Pyrrolnitrin and phenazine production by Pseudomonas cepacia, strain 5.5B, a biocontrol agent of Rhizoctonia solani**. *Applied Microbiology and Biotechnology 1995 43:2*, *43*(2), 211–216.

Castrillo, G., Teixeira, P. J. P. L., Paredes, S. H., Law, T. F., de Lorenzo, L., Feltcher, M. E., Finkel, O. M., Breakfield, N. W., Mieczkowski, P., Jones, C. D., Paz-Ares, J., & Dangl, J. L. (2017). **Root microbiota drive direct integration of phosphate stress and immunity**. *Nature 2017 543:7646*, *543*(7646), 513–518.

Castro, B., Citterico, M., Kimura, S., Stevens, D. M., Wrzaczek, M., & Coaker, G. (2021). **Stress-induced reactive oxygen species compartmentalization, perception and signalling.** *Nature Plants 2021 7:4*, *7*(4), 403–412.

Chaisson, M. J., & Tesler, G. (2012). **Mapping single molecule sequencing reads using basic local alignment with successive refinement (BLASR): Application and theory**. *BMC Bioinformatics*, *13*(1), 1–18.

Challis, R., Richards, E., Rajan, J., Cochrane, G., & Blaxter, M. (2020). **BlobToolKit – Interactive Quality Assessment of Genome Assemblies.** *G3 Genes|Genomes|Genetics*, *10*(4), 1361–1374.

Charlop-Powers, Z., Owen, J. G., Reddy, B. V. B., Ternei, M. A., & Brady, S. F. (2014). **Chemical-biogeographic survey of secondary metabolism in soil.** *Proceedings of the National Academy of Sciences of the United States of America*, *111*(10), 3757–3762.

Chaves, M. M., Flexas, J., & Pinheiro, C. (2009). **Photosynthesis under drought and salt stress: regulation mechanisms from whole plant to cell**. *Annals of Botany*, *103*(4), 551–560.

Chen, Y. T., Wang, Y., & Yeh, K. C. (2017). **Role of root exudates in metal acquisition and tolerance.** *Current Opinion in Plant Biology*, *39*, 66–72.

Chin-A-Woeng, T. F. C., Bloemberg, G. v., & Lugtenberg, B. J. J. (2003). **Phenazines and their role in biocontrol by Pseudomonas bacteria.** *New Phytologist*, *157*(3), 503–523.

Chojak-Koźniewska, J., Linkiewicz, A., Sowa, S., Radzioch, M. A., & Kuźniak, E. (2017). **Interactive effects of salt stress and Pseudomonas syringae pv. lachrymans infection in cucumber: Involvement of antioxidant enzymes, abscisic acid and salicylic acid**. *Environmental and Experimental Botany*, *136*, 9–20.

Clough, S. E., Jousset, A., Elphinstone, J. G., & Friman, V. P. (2022). **Combining in vitro and in vivo screening to identify efficient Pseudomonas biocontrol strains against the phytopathogenic bacterium Ralstonia solanacearum.** *MicrobiologyOpen*, *11*(2).

Coleman-Derr, D., Desgarennes, D., Fonseca-Garcia, C., Gross, S., Clingenpeel, S., Woyke, T., North, G., Visel, A., Partida-Martinez, L. P., & Tringe, S. G. (2016). **Plant compartment and biogeography affect microbiome composition in cultivated and native Agave species**. *New Phytologist*, *209*(2), 798–811.

Conway, J. M., Walton, W. G., Salas-González, I., Law, T. F., Lindberg, C. A., Crook, L. E., Kosina, S. M., Fitzpatrick, C. R., Lietzan, A. D., Northen, T. R., Jones, C. D., Finkel, O. M., Redinbo, M. R., & Dangl, J. L. (2022). **Diverse MarR bacterial regulators of auxin catabolism in the plant microbiome.** *Nature Microbiology 2022 7:11*, *7*(11), 1817–1833.

Cornforth, D. M., & Foster, K. R. (2013). **Competition sensing: the social side of bacterial stress responses.** *Nature Reviews Microbiology 2013 11:4*, *11*(4), 285–293.

Corwin, D. L. (2021). **Climate change impacts on soil salinity in agricultural areas.** *European Journal of Soil Science*, *72*(2), 842–862.

Cregger, M. A., Veach, A. M., Yang, Z. K., Crouch, M. J., Vilgalys, R., Tuskan, G. A., & Schadt, C. W. (2018). **The Populus holobiont: Dissecting the effects of plant niches and genotype on the microbiome.** *Microbiome*, *6*(1), 1–14.

Crits-Christoph, A., Diamond, S., Butterfield, C. N., Thomas, B. C., & Banfield, J. F. (2018). **Novel soil bacteria possess diverse genes for secondary metabolite biosynthesis.** *Nature 2018 558:7710*, *558*(7710), 440–444.

Cunnac, S., Lindeberg, M., & Collmer, A. (2009). **Pseudomonas syringae type III secretion system effectors: repertoires in search of functions.** *Current Opinion in Microbiology*, *12*(1), 53–60.

Dakora, F. D., & Phillips, D. A. (2002). **Root exudates as mediators of mineral acquisition in low-nutrient environments.** *Food Security in Nutrient-Stressed Environments: Exploiting Plants' Genetic Capabilities*, 201–213.

Dalla Serra, M., Fagiuoli, G., Nordera, P., Bernhart, I., della Volpe, C., di Giorgio, D., Ballio, A., & Menestrina, G. (1999). **The interaction of lipodepsipeptide toxins from Pseudomonas syringae pv. syringae with biological and model membranes: a comparison of syringotoxin, syringomycin, and two syringopeptins.** *Molecular Plant-Microbe Interactions : MPMI*, *12*(5), 391–400.

de Maayer, P., Venter, S. N., Kamber, T., Duffy, B., Coutinho, T. A., & Smits, T. H. M. (2011). **Comparative genomics of the type VI secretion systems of Pantoea and Erwinia species reveals the presence of putative effector islands that may be translocated by the VgrG and Hcp proteins.** *BMC Genomics*, *12*(1), 1–15.

DeFalco, T. A., & Zipfel, C. (2021). **Molecular mechanisms of early plant pattern-triggered immune signaling.** *Molecular Cell*, *81*(17), 3449–3467.

Dehio, C., & Meyer, M. (1997). **Maintenance of broad-host-range incompatibility group P and group Q plasmids and transposition of Tn5 in Bartonella henselae following conjugal plasmid transfer from Escherichia coli.** *Journal of Bacteriology*, *179*(2), 538–540.

Deslandes, L., Pileur, F., Liaubet, L., Camut, S., Can, C., Williams, K., Holub, E., Beynon, J., Arlat, M., & Marco, Y. (2007). **Genetic Characterization of RRS1, a Recessive Locus in Arabidopsis thaliana that Confers Resistance to the Bacterial Soilborne Pathogen Ralstonia solanacearum**. *MPMI*, *11*(7), 659–667.

Dimartino, M. , P. S. , L. C. , C. I. , V. A. (2011). **Occurrence and Pathogenicity of Pseudomonas Fluorescens and P. Putida on Tomato Plants in Italy.** *Occurrence and Pathogenicity of Pseudomonas Fluorescens and P. Putida on Tomato Plants in Italy*, 79–87.

Dimkić, I., Janakiev, T., Petrović, M., Degrassi, G., & Fira, D. (2022). **Plant-associated Bacillus and Pseudomonas antimicrobial activities in plant disease suppression via biological control mechanisms - A review**. *Physiological and Molecular Plant Pathology*, *117*, 101754.

Dimkic, I., Stankovic, S., Nišavic, M., Petkovic, M., Ristivojevic, P., Fira, D., & Beric, T. (2017). **The Profile and Antimicrobial Activity of Bacillus Lipopeptide Extracts of Five Potential Biocontrol Strains.** *Frontiers in Microbiology*, *8*(MAY).

Dixon, P. (2003). **VEGAN, a package of R functions for community ecology**. *Journal of Vegetation Science*, *14*(6), 927–930.

Duca, D. R., & Glick, B. R. (2020). **Indole-3-acetic acid biosynthesis and its regulation in plant-associated bacteria.** *Applied Microbiology and Biotechnology 2020 104:20*, *104*(20), 8607–8619.

Durán, P., Thiergart, T., Garrido-Oter, R., Agler, M., Kemen, E., Schulze-Lefert, P., & Hacquard, S. (2018). **Microbial Interkingdom Interactions in Roots Promote Arabidopsis Survival**. *Cell*, *175*(4), 973-983.e14.

Edgar, R. C., & Bateman, A. (2010). **Search and clustering orders of magnitude faster than BLAST**. *Bioinformatics*, *26*(19), 2460–2461.

Edwards, J., Johnson, C., Santos-Medellín, C., Lurie, E., Podishetty, N. K., Bhatnagar, S., Eisen, J. A., Sundaresan, V., & Jeffery, L. D. (2015). **Structure, variation, and assembly of the root-associated microbiomes of rice.** *Proceedings of the National Academy of Sciences of the United States of America*, *112*(8), E911–E920.

Eichmann, R., Richards, L., & Schäfer, P. (2021). **Hormones as go-betweens in plant microbiome assembly**. *The Plant Journal*, *105*(2), 518–541.

Eilers, K. G., Lauber, C. L., Knight, R., & Fierer, N. (2010). **Shifts in bacterial community structure associated with inputs of low molecular weight carbon compounds to soil.** *Soil Biology and Biochemistry*, *42*(6), 896–903.

Eitzen, K., Sengupta, P., Kroll, S., Kemen, E., & Doehlemann, G. (n.d.). **A fungal member of the Arabidopsis thaliana phyllosphere antagonizes Albugo laibachii via a GH25 lysozyme**.

Emmett, B. D., Lévesque-Tremblay, V., & Harrison, M. J. (2021). **Conserved and reproducible bacterial communities associate with extraradical hyphae of arbuscular mycorrhizal fungi**. *The ISME Journal 2021 15:8*, *15*(8), 2276–2288.

Eswar, D., Karuppusamy, R., & Chellamuthu, S. (2021). **Drivers of soil salinity and their correlation with climate change.** *Current Opinion in Environmental Sustainability*, *50*, 310–318.

Eynard, A., Lal, R., & Wiebe, K. (2008). **Crop Response in Salt-Affected Soils**., *27*(1), 5–50.

Falardeau, J., Wise, C., Novitsky, L., & Avis, T. J. (2013). **Ecological and Mechanistic Insights Into the Direct and Indirect Antimicrobial Properties of Bacillus subtilis Lipopeptides on Plant Pathogens.** *Journal of Chemical Ecology 2013 39:7*, *39*(7), 869–878.

Fan, J., Hill, L., Crooks, C., Doerner, P., & Lamb, C. (2009). **Abscisic Acid Has a Key Role in Modulating Diverse Plant-Pathogen Interactions**. *Plant Physiology*, *150*(4), 1750–1761.

Feil, H., Feil, W. S., Chain, P., Larimer, F., DiBartolo, G., Copeland, A., Lykidis, A., Trong, S., Nolan, M., Goltsman, E., Thiel, J., Malfatti, S., Loper, J. E., Lapidus, A., Detter, J. C., Land, M., Richardson, P. M., Kyrpides, N. C., Ivanova, N., & Lindow, S. E. (2005). **Comparison of the complete genome sequences of Pseudomonas syringae pv. syringae B728a and pv. tomato DC3000.** *Proceedings of the National Academy of Sciences of the United States of America*, *102*(31), 11064–11069.

Fierer, N., & Jackson, R. B. (2006). **The diversity and biogeography of soil bacterial communities**. *Proceedings of the National Academy of Sciences of the United States of America*, *103*(3), 626–631.

Figueiredo, A. R. T., Özkaya, Ö., Kümmerli, R., & Kramer, J. (2022). **Siderophores drive invasion dynamics in bacterial communities through their dual role as public good versus public bad**. *Ecology Letters*, *25*(1), 138–150.

Finkel, O. M., Salas-González, I., Castrillo, G., Conway, J. M., Law, T. F., Teixeira, P. J. P. L., Wilson, E. D., Fitzpatrick, C. R., Jones, C. D., & Dangl, J. L. (2020). **A single bacterial genus maintains root growth in a complex microbiome.** *Nature 2020 587:7832*, *587*(7832), 103–108.

Finkel, O. M., Salas-González, I., Castrillo, G., Spaepen, S., Law, T. F., Teixeira, P. J. P. L., Jones, C. D., & Dangl, J. L. (2019). **The effects of soil phosphorus content on plant microbiota are driven by the plant phosphate starvation response**. *PLOS Biology*, *17*(11), e3000534.

Fira, D., Dimkić, I., Berić, T., Lozo, J., & Stanković, S. (2018). **Biological control of plant pathogens by Bacillus species.** *Journal of Biotechnology*, *285*, 44–55.

Francl, L. J. (2001). **The Disease Triangle: A Plant Pathological Paradigm Revisited.** *The Plant Health Instructor*.

Garrido-Oter, R., Nakano, R. T., Dombrowski, N., Ma, K. W., McHardy, A. C., & Schulze-Lefert, P. (2018). **Modular Traits of the Rhizobiales Root Microbiota and Their Evolutionary Relationship with Symbiotic Rhizobia.** *Cell Host & Microbe*, *24*(1), 155-167.e5.

Geng, Y., Wu, R., Wee, C. W., Xie, F., Wei, X., Chan, P. M. Y., Tham, C., Duan, L., & Dinneny, J. R. (2013). **A Spatio-Temporal Understanding of Growth Regulation during the Salt Stress Response in Arabidopsis.** *The Plant Cell*, *25*(6), 2132–2154.

Getzke, F., Thiergart, T., & Hacquard, S. (2019). **Contribution of bacterial-fungal balance to plant and animal health.** *Current Opinion in Microbiology*, *49*, 66–72.

Ghorbel, M., Brini, F., Sharma, A., & Landi, M. (2021). **Role of jasmonic acid in plants: the molecular point of view.** *Plant Cell Reports 2021 40:8*, *40*(8), 1471–1494.

Gibson, D. G., Young, L., Chuang, R. Y., Venter, J. C., Hutchison, C. A., & Smith, H. O. (2009). **Enzymatic assembly of DNA molecules up to several hundred kilobases.** *Nature Methods*, *6*(5), 343–345.

Glandorf, D. C. M., Verheggen, P., Jansen, T., Jorritsma, J. W., Smit, E., Leeflang, P., Wernars, K., Thomashow, L. S., Laureijs, E., Thomas-Oates, J. E., Bakker, P. A. H. M., & van Loon, L. C. (2001). **Effect of Genetically Modified Pseudomonas putida WCS358r on the Fungal Rhizosphere Microflora of Field-Grown Wheat**. *Applied and Environmental Microbiology*, *67*(8), 3371–3378.

Glick, B. R. (2014). **Bacteria with ACC deaminase can promote plant growth and help to feed the world.** *Microbiological Research*, *169*(1), 30–39.

Grgurina, I., Bensaci, M., Pocsfalvi, G., Mannina, L., Cruciani, O., Fiore, A., Fogliano, V., Sorensen, K. N., & Takemoto, J. Y. (2005). **Novel cyclic lipodepsipeptide from Pseudomonas syringae pv. lachrymans strain 508 and syringopeptin antimicrobial activities**. *Antimicrobial Agents and Chemotherapy*, *49*(12), 5037–5045.

Grgurina, I., Mariotti, F., Fogliano, V., Gallo, M., Scaloni, A., Iacobellis, N. S., lo Cantore, P., Mannina, L., van Axel Castelli, V., Greco, M. L., & Graniti, A. (2002). **A new syringopeptin produced by bean strains of Pseudomonas syringae pv. syringae.** *Biochimica et Biophysica Acta (BBA) - Protein Structure and Molecular Enzymology*, *1597*(1), 81–89.

Gu, S., Wei, Z., Shao, Z., Friman, V. P., Cao, K., Yang, T., Kramer, J., Wang, X., Li, M., Mei, X., Xu, Y., Shen, Q., Kümmerli, R., & Jousset, A. (2020). **Competition for iron drives phytopathogen control by natural rhizosphere microbiomes.** *Nature Microbiology*, *5*(8),

Gu, S., Yang, T., Shao, Z., Wang, T., Cao, K., Jousset, A., Friman, V.-P., Mallon, C., Mei, X., Wei, Z., Xu, Y., Shen, Q., & Pommier, T. (2020). **Siderophore-Mediated Interactions Determine the Disease Suppressiveness of Microbial Consortia**. *MSystems*, *5*(3).

Guo, M., Tian, F., Wamboldt, Y., & Alfano, J. R. (2009). **The Majority of the Type III Effector Inventory of Pseudomonas syringae pv. tomato DC3000 Can Suppress Plant Immunity.** *22*(9), 1069–1080.

Guo, X., Zhang, X., Qin, Y., Liu, Y. X., Zhang, J., Zhang, N., Wu, K., Qu, B., He, Z., Wang, X., Zhang, X., Hacquard, S., Fu, X., & Bai, Y. (2020). **Host-Associated Quantitative Abundance Profiling Reveals the Microbial Load Variation of Root Microbiome**. *Plant Communications*, *1*(1), 100003.

Haapalainen, M., Mosorin, H., Dorati, F., Wu, R. F., Roine, E., Taira, S., Nissinen, R., Mattinen, L., Jackson, R., Pirhonen, M., & Lin, N. C. (2012). **Hcp2, a secreted protein of the phytopathogen Pseudomonas syringae pv. tomato DC3000, is required for fitness for competition against bacteria and yeasts.** *Journal of Bacteriology*, *194*(18), 4810–4822.

Hacquard, S., Garrido-Oter, R., González, A., Spaepen, S., Ackermann, G., Lebeis, S., McHardy, A. C., Dangl, J. L., Knight, R., Ley, R., & Schulze-Lefert, P. (2015). **Microbiota and host nutrition across plant and animal kingdoms**. *Cell Host and Microbe*, *17*(5), 603–616.

Haichar, F. el Z., Heulin, T., Guyonnet, J. P., & Achouak, W. (2016). **Stable isotope probing of carbon flow in the plant holobiont.** *Current Opinion in Biotechnology*, *41*, 9–13.

Hanin, M., Ebel, C., Ngom, M., Laplaze, L., & Masmoudi, K. (2016). **New Insights on Plant Salt Tolerance Mechanisms and Their Potential Use for Breeding.** *Frontiers in Plant Science*, *7*(NOVEMBER2016).

Harbort, C. J., Hashimoto, M., Inoue, H., Niu, Y., Guan, R., Rombolà, A. D., Kopriva, S., Voges, M. J. E. E. E., Sattely, E. S., Garrido-Oter, R., & Schulze-Lefert, P. (2020). **Root-Secreted Coumarins and the Microbiota Interact to Improve Iron Nutrition in Arabidopsis.** *Cell Host & Microbe*, *28*(6), 825-837.e6.

Harcombe, W. (2010). **NOVEL COOPERATION EXPERIMENTALLY EVOLVED BETWEEN SPECIES.** *Evolution*, *64*(7), 2166–2172.

Hassani, M. A., Durán, P., & Hacquard, S. (2018). **Microbial interactions within the plant holobiont.** *Microbiome*, *6*(1), 58.

Helfrich, E. J. N., Vogel, C. M., Ueoka, R., Schäfer, M., Ryffel, F., Müller, D. B., Probst, S., Kreuzer, M., Piel, J., & Vorholt, J. A. (2018). **Bipartite interactions, antibiotic production and biosynthetic potential of the Arabidopsis leaf microbiome**. *Nature Microbiology 2018 3:8*, *3*(8), 909–919.

Hervé, V., le Roux, X., Uroz, S., Gelhaye, E., & Frey-Klett, P. (2014). **Diversity and structure of bacterial communities associated with Phanerochaete chrysosporium during wood decay.** *Environmental Microbiology*, *16*(7), 2238–2252.

Hiruma, K., Gerlach, N., Sacristán, S., Nakano, R. T., Hacquard, S., Kracher, B., Neumann, U., Ramírez, D., Bucher, M., O'Connell, R. J., & Schulze-Lefert, P. (2016). **Root Endophyte Colletotrichum tofieldiae Confers Plant Fitness Benefits that Are Phosphate Status Dependent.** *Cell*, *165*(2), 464–474.

Hjort, K., Bergström, M., Adesina, M. F., Jansson, J. K., Smalla, K., & Sjöling, S. (2009). **Chitinase genes revealed and compared in bacterial isolates, DNA extracts and a metagenomic library from a phytopathogen-suppressive soil.** *FEMS Microbiology Ecology*, *71*(2), 197–207.

Ho, B. T., Dong, T. G., & Mekalanos, J. J. (2014). **A View to a Kill: The Bacterial Type VI Secretion System.** *Cell Host & Microbe*, *15*(1), 9–21.

Hou, S., Thiergart, T., Vannier, N., Mesny, F., Ziegler, J., Pickel, B., & Hacquard, S. (2021). **A microbiota–root–shoot circuit favours Arabidopsis growth over defence under suboptimal light.** *Nature Plants 2021 7:8*, *7*(8), 1078–1092.

Hu, J., Wei, Z., Friman, V. P., Gu, S. H., Wang, X. F., Eisenhauer, N., Yang, T. J., Ma, J., Shen, Q. R., Xu, Y. C., & Jousset, A. (2016). **Probiotic diversity enhances rhizosphere microbiome function and plant disease suppression**. *MBio*, *7*(6).

Hu, L., Robert, C. A. M., Cadot, S., Zhang, X., Ye, M., Li, B., Manzo, D., Chervet, N., Steinger, T., van der Heijden, M. G. A., Schlaeppi, K., & Erb, M. (2018). **Root exudate metabolites drive plant-soil feedbacks on growth and defense by shaping the rhizosphere microbiota**. *Nature Communications 2018 9:1*, *9*(1), 1–13.

Hua, D., Wang, C., He, J., Liao, H., Duan, Y., Zhu, Z., Guo, Y., Chen, Z., & Gong, Z. (2012). **A Plasma Membrane Receptor Kinase, GHR1, Mediates Abscisic Acid- and Hydrogen Peroxide-Regulated Stomatal Movement in Arabidopsis.** *The Plant Cell*, *24*(6), 2546–2561.

Huerta-Cepas, J., Serra, F., & Bork, P. (2016). **ETE 3: Reconstruction, Analysis, and Visualization of Phylogenomic Data**. *Molecular Biology and Evolution*, *33*(6), 1635–1638.

Hutchison, M. L., & Gross, D. C. (1997). **Lipopeptide phytotoxins produced by Pseudomonas syringae pv. syringae: comparison of the biosurfactant and ion channel-forming activities of syringopeptin and syringomycin**. *Molecular Plant-Microbe Interactions : MPMI*, *10*(3), 347–354.

Isnansetyo, A., Cui, L., Hiramatsu, K., & Kamei, Y. (2003). **Antibacterial activity of 2,4-diacetylphloroglucinol produced by Pseudomonas sp. AMSN isolated from a marine alga, against vancomycin-resistant Staphylococcus aureus.** *International Journal of Antimicrobial Agents*, *22*(5), 545–547.

Jasim, B., Sreelakshmi, K. S., Mathew, J., & Radhakrishnan, E. K. (2016). **Surfactin, Iturin, and Fengycin Biosynthesis by Endophytic Bacillus sp. from Bacopa monnieri.** *Microbial Ecology 2016 72:1*, *72*(1), 106–119.

Jiang, C. J., Shimono, M., Sugano, S., Kojima, M., Yazawa, K., Yoshida, R., Lnoue, H., Hayashi, N., Sakakibara, H., & Takatsuji, H. (2010). **Abscisic acid interacts antagonistically with salicylic acid signaling pathway in rice-magnaporthe grisea interaction**. *Molecular Plant-Microbe Interactions*, *23*(6), 791–798.

Jones, J. D. G., & Dangl, J. L. (2006). **The plant immune system**. *Nature 2006 444:7117*, *444*(7117), 323–329.

Julian, W. T., Vasilchenko, A. v., Shpindyuk, D. D., Poshvina, D. v., & Vasilchenko, A. S. (2020). **Bacterial-Derived Plant Protection Metabolite 2,4-Diacetylphloroglucinol: Effects on Bacterial Cells at Inhibitory and Subinhibitory Concentrations.** *Biomolecules 2021, Vol. 11, Page 13*, *11*(1), 13.

Karasov, T. L., Almario, J., Friedemann, C., Ding, W., Giolai, M., Heavens, D., Kersten, S., Lundberg, D. S., Neumann, M., Regalado, J., Neher, R. A., Kemen, E., & Weigel, D. (2018). **Arabidopsis thaliana and Pseudomonas Pathogens Exhibit Stable Associations over Evolutionary Timescales.** *Cell Host & Microbe*, *24*(1), 168-179.e4.

Kassambara, A. (2020). **'ggplot2' Based Publication Ready Plots** *[R package ggpubr version 0.4.0]*.

Kassambara, A. (2021). **Pipe-Friendly Framework for Basic Statistical Tests** *[R package rstatix version 0.7.0]*.

Keel, C., Schnider, U., Maurhofer, M., Voisard, C., Laville, J., Burger, U., Wirthner, P. J., Haas, D., & Défago, G. (1992). **Suppression of Root Diseases by Pseudomonas fluorescens CHA0: Importance of the Bacterial Secondary Metabolite 2,4-Diacetylphloroglucinol.** *Molecular Plant-Microbe Interactions*, *5*(1), 4–13.

Keel, C., Weller, D. M., Natsch, A., Défago, G., Cook, R. J., & Thomashow, L. S. (1996). **Conservation of the 2,4-diacetylphloroglucinol biosynthesis locus among fluorescent Pseudomonas strains from diverse geographic locations**. *Applied and Environmental Microbiology*, *62*(2), 552–563.

Kim, D., Paggi, J. M., Park, C., Bennett, C., & Salzberg, S. L. (2019). **Graph-based genome alignment and genotyping with HISAT2 and HISAT-genotype.** *Nature Biotechnology 2019 37:8*, *37*(8), 907–915.

Knudsen, I. M. B., Hockenhull, J., Funck Jensen, D., Gerhardson, B., Hökeberg, M., Tahvonen, R., Teperi, E., Sundheim, L., & Henriksen, B. (1997). **Selection of biological control agents for controlling soil and seed-borne diseases in the field.** *European Journal of Plant Pathology*, *103*, 775–784.

Kobayashi, D. Y., Reedy, R. M., Bick, J. A., & Oudemans, P. v. (2002). **Characterization of a chitinase gene from Stenotrophomonas maltophilia strain 34S1 and its involvement in biological control.** *Applied and Environmental Microbiology*, *68*(3), 1047–1054.

Kobayashi, T., & Nishizawa, N. K. (2012). **Iron Uptake, Translocation, and Regulation in Higher Plants.** *Annurev-Arplant*, *63*, 131–152.

Kohlmeier, S., Smits, T. H. M., Ford, R. M., Keel, C., Harms, H., & Wick, L. Y. (2005). **Taking the fungal highway: Mobilization of pollutant-degrading bacteria by fungi.** *Environmental Science and Technology*, *39*(12), 4640–4646.

Kolmogorov, M., Yuan, J., Lin, Y., & Pevzner, P. A. (2019). **Assembly of long, error-prone reads using repeat graphs.** *Nature Biotechnology*, *37*(5), 540–546.

Koprivova, A., & Kopriva, S. (2022). **Plant secondary metabolites altering root microbiome composition and function.** *Current Opinion in Plant Biology*, *67*, 102227.

Koprivova, A., Schuck, S., Jacoby, R. P., Klinkhammer, I., Welter, B., Leson, L., Martyn, A., Nauen, J., Grabenhorst, N., Mandelkow, J. F., Zuccaro, A., Zeier, J., & Kopriva, S. (2019). **Root-specific camalexin biosynthesis controls the plant growth-promoting effects of multiple bacterial strains.** *Proceedings of the National Academy of Sciences of the United States of America*, *116*(31), 15735–15744.

Köster, P., DeFalco, T. A., & Zipfel, C. (2022). **Ca2+ signals in plant immunity.** *The EMBO Journal*, *41*(12), e110741.

Kremer, J. M., Sohrabi, R., Paasch, B. C., Rhodes, D., Thireault, C., Schulze-Lefert, P., Tiedje, J. M., & He, S. Y. (2021). **Peat-based gnotobiotic plant growth systems for Arabidopsis microbiome research.** *Nature Protocols 2021 16:5*, *16*(5), 2450–2470.

Kuiper, I., Lagendijk, E. L., Pickford, R., Derrick, J. P., Lamers, G. E. M., Thomas-Oates, J. E., Lugtenberg, B. J. J., & Bloemberg, G. v. (2004). **Characterization of two Pseudomonas putida lipopeptide biosurfactants, putisolvin I and II, which inhibit biofilm formation and break down existing biofilms.** *Molecular Microbiology*, *51*(1), 97–113.

Kvitko, B. H., & Collmer, A. (2011). **Construction of Pseudomonas syringae pv. tomato DC3000 mutant and polymutant strains.** *Methods in Molecular Biology (Clifton, N.J.)*, *712*, 109–128.

Kwak, Y. S., Han, S., Thomashow, L. S., Rice, J. T., Paulitz, T. C., Kim, D., & Weller, D. M. (2011). **Saccharomyces cerevisiae genome-wide mutant screen for sensitivity to 2,4-diacetylphloroglucinol, an antibiotic produced by Pseudomonas fluorescens.** *Applied and Environmental Microbiology*, *77*(5), 1770–1776.

Lahrmann, U., Strehmel, N., Langen, G., Frerigmann, H., Leson, L., Ding, Y., Scheel, D., Herklotz, S., Hilbert, M., & Zuccaro, A. (2015). **Mutualistic root endophytism is not associated with the reduction of saprotrophic traits and requires a noncompromised plant innate immunity**. *Source: The New Phytologist*, *207*(3), 841–857.

Lamont, I. L., Martin, L. W., Sims, T., Scott, A., & Wallace, M. (2006). **Characterization of a gene encoding an acetylase required for pyoverdine synthesis in Pseudomonas aeruginosa**. *Journal of Bacteriology*, *188*(8), 3149–3152.

Lanteigne, C., Gadkar, V. J., Wallon, T., Novinscak, A., & Filion, M. (2012). **Production of DAPG and HCN by Pseudomonas sp. LBUM300 Contributes to the Biological Control of Bacterial Canker of Tomato**. *PHYTO-11-11-0312*, *102*(10), 967–973.

Letunic, I., & Bork, P. (2021). **Interactive Tree Of Life (iTOL) v5: an online tool for phylogenetic tree display and annotation.** *Nucleic Acids Research*, *49*(W1), W293–W296.

Levy, A., Salas Gonzalez, I., Mittelviefhaus, M., Clingenpeel, S., Herrera Paredes, S., Miao, J., Wang, K., Devescovi, G., Stillman, K., Monteiro, F., Rangel Alvarez, B., Lundberg, D. S., Lu, T. Y., Lebeis, S., Jin, Z., McDonald, M., Klein, A. P., Feltcher, M. E., Rio, T. G., Dangl, J. L. (2017). **Genomic features of bacterial adaptation to plants.** *Nature Genetics 2017 50:1*, *50*(1), 138–150.

Leys, C., Ley, C., Klein, O., Bernard, P., & Licata, L. (2013). **Detecting outliers: Do not use standard deviation around the mean, use absolute deviation around the median.** *Journal of Experimental Social Psychology*, *49*(4), 764–766.

Liao, Y., Smyth, G. K., & Shi, W. (2014). **featureCounts: an efficient general purpose program for assigning sequence reads to genomic features.** *Bioinformatics*, *30*(7), 923–930.

Lim, C. K., Hassan, K. A., Tetu, S. G., Loper, J. E., & Paulsen, I. T. (2012). **The Effect of Iron Limitation on the Transcriptome and Proteome of Pseudomonas fluorescens Pf-5**. *PLOS ONE*, *7*(6), e39139.

Liu, Y., Dai, C., Zhou, Y., Qiao, J., Tang, B., Yu, W., Zhang, R., Liu, Y., & Lu, S. E. (2021). **Pyoverdines Are Essential for the Antibacterial Activity of Pseudomonas chlororaphis YL-1 under Low-Iron Conditions.** *Applied and Environmental Microbiology*, *87*(7), 1–17.

Loper, J. E., & Lindow, S. E. (1994). **A biological sensor for iron available to bacteria in their habitats on plant surfaces.** *Applied and Environmental Microbiology*, *60*(6), 1934–1941.

Love, M. I., Huber, W., & Anders, S. (2014). **Moderated estimation of fold change and dispersion for RNA-seq data with DESeq2**. *Genome Biology*, *15*(12), 1–21.

Lu, Y., & Tsuda, K. (2021). **Intimate Association of PRR- and NLR-Mediated Signaling in Plant Immunity.** *Molecular Plant-Microbe Interactions : MPMI*, *34*(1), 3–14.

Lundberg, D. S., Lebeis, S. L., Paredes, S. H., Yourstone, S., Gehring, J., Malfatti, S., Tremblay, J., Engelbrektson, A., Kunin, V., Rio, T. G. del, Edgar, R. C., Eickhorst, T., Ley, R. E., Hugenholtz, P., Tringe, S. G., & Dangl, J. L. (2012). **Defining the core Arabidopsis thaliana root microbiome.** *Nature 2012 488:7409*, *488*(7409), 86–90.

Ma, K. W., Niu, Y., Jia, Y., Ordon, J., Copeland, C., Emonet, A., Geldner, N., Guan, R., Stolze, S. C., Nakagami, H., Garrido-Oter, R., & Schulze-Lefert, P. (2021). **Coordination of microbe–host homeostasis by crosstalk with plant innate immunity.** *Nature Plants 2021 7:6*, *7*(6), 814–825.

Madeira, F., Pearce, M., Tivey, A. R. N., Basutkar, P., Lee, J., Edbali, O., Madhusoodanan, N., Kolesnikov, A., & Lopez, R. (2022). **Search and sequence analysis tools services from EMBL-EBI in 2022.** *Nucleic Acids Research*, *50*(W1), gkac240–gkac240.

Makovitzki, A., Avrahami, D., & Shai, Y. (2006). **Ultrashort antibacterial and antifungal lipopeptides.** *Proceedings of the National Academy of Sciences of the United States of America*, *103*(43), 15997–16002.

Marcec, M. J., Gilroy, S., Poovaiah, B. W., & Tanaka, K. (2019). **Mutual interplay of Ca2+ and ROS signaling in plant immune response.** *Plant Science*, *283*, 343–354.

Marín, O., González, B., & Poupin, M. J. (2021). **From Microbial Dynamics to Functionality in the Rhizosphere: A Systematic Review of the Opportunities With Synthetic Microbial Communities.** *Frontiers in Plant Science*, *12*, 843.

Martínez-García, E., Goñi-Moreno, A., Bartley, B., McLaughlin, J., Sánchez-Sampedro, L., Pascual Del Pozo, H., Prieto Hernández, C., Marletta, A. S., de Lucrezia, D., Sánchez-Fernández, G., Fraile, S., & de Lorenzo, V. (2020). **SEVA 3.0: an update of the Standard European Vector Architecture for enabling portability of genetic constructs among diverse bacterial hosts.** *Nucleic Acids Research*, *48*(D1), D1164–D1170.

Massoni, J., Bortfeld-Miller, M., Widmer, A., & Vorholt, J. A. (2021). **Capacity of soil bacteria to reach the phyllosphere and convergence of floral communities despite soil microbiota variation.** *Proceedings of the National Academy of Sciences of the United States of America*, *118*(41), e2100150118.

Mataigne, V., Vannier, N., Vandenkoornhuyse, P., & Hacquard, S. (2022). **Multi-genome metabolic modeling predicts functional inter-dependencies in the Arabidopsis root microbiome**. *Microbiome*.

McKay Fletcher, D. M., Ruiz, S., Dias, T., Petroselli, C., & Roose, T. (2020). **Linking root structure to functionality: the impact of root system architecture on citrate-enhanced phosphate uptake**. *New Phytologist*, *227*(2), 376–391.

McMurdie, P. J., & Holmes, S. (2013**). phyloseq: An R Package for Reproducible Interactive Analysis and Graphics of Microbiome Census Data**. *PLOS ONE*, *8*(4), e61217.

McMurdie, P. J., & Holmes, S. (2014). **Waste Not, Want Not: Why Rarefying Microbiome Data Is Inadmissible.** *PLOS Computational Biology*, *10*(4), e1003531.

Melnyk, R. A., Hossain, S. S., & Haney, C. H. (2019). **Convergent gain and loss of genomic islands drive lifestyle changes in plant-associated Pseudomonas**. *The ISME Journal 2019 13:6*, *13*(6), 1575–1588.

Mendes, R., Kruijt, M., de Bruijn, I., Dekkers, E., van der Voort, M., Schneider, J. H. M., Piceno, Y. M., DeSantis, T. Z., Andersen, G. L., Bakker, P. A. H. M., & Raaijmakers, J. M. (2011). **Deciphering the Rhizosphere Microbiome for Disease-Suppressive Bacteria**. *Science*, *332*(6033), 1097–1100.

Merrell, D. S., Hava, D. L., & Camilli, A. (2002). **Identification of novel factors involved in colonization and acid tolerance of Vibrio cholerae.** *Molecular Microbiology*, *43*(6), 1471–1491.

Mi, H., Muruganujan, A., Ebert, D., Huang, X., & Thomas, P. D. (2019**). PANTHER version 14: more genomes, a new PANTHER GO-slim and improvements in enrichment analysis tools.** *Nucleic Acids Research*, *47*(D1), D419–D426.

Mi, H., Muruganujan, A., Huang, X., Ebert, D., Mills, C., Guo, X., & Thomas, P. D. (2019). **Protocol Update for large-scale genome and gene function analysis with the PANTHER classification system (v.14.0)**. *Nature Protocols 2019 14:3*, *14*(3), 703–721.

Mirleau, P., Delorme, S., Philippot, L., Meyer, J.-M., Mazurier, S., & Lemanceau, P. (2000). **Fitness in soil and rhizosphere of Pseudomonas fluorescens C7R12 compared with a C7R12 mutant affected in pyoverdine synthesis and uptake.** *FEMS Microbiology Ecology*, *34*(1), 35–44.

Moormann, J., Heinemann, B., & Hildebrandt, T. M. (2022). **News about amino acid metabolism in plant–microbe interactions.** *Trends in Biochemical Sciences*, *47*(10), 839–850.

Mukhopadhyay, R., Sarkar, B., Jat, H. S., Sharma, P. C., & Bolan, N. S. (2021). **Soil salinity under climate change: Challenges for sustainable agriculture and food security.** *Journal of Environmental Management*, *280*, 111736.

Naylor, D., Degraaf, S., Purdom, E., & Coleman-Derr, D. (2017). **Drought and host selection influence bacterial community dynamics in the grass root microbiome.** *The ISME Journal 2017 11:12*, *11*(12), 2691–2704.

Nazir, R., Boersma, F. G. H., Warmink, J. A., & van Elsas, J. D. (2010**). Lyophyllum sp. strain Karsten alleviates pH pressure in acid soil and enhances the survival of Variovorax paradoxus HB44 and other bacteria in the mycosphere.** *Soil Biology and Biochemistry*, *42*(12), 2146–2152.

Neu, T. R., Härtner, T., & Poralla, K. (1990). **Surface active properties of viscosin: a peptidolipid antibiotic.** *Applied Microbiology and Biotechnology 1990 32:5*, *32*(5), 518–520.

Ngou, B. P. M., Jones, J. D. G., & Ding, P. (2022). **Plant immune networks.** *Trends in Plant Science*, *27*(3), 255–273.

Nielsen, T. H., Thrane, C., Christophersen, C., Anthoni, U., & Sørensen, J. (2000). **Structure, production characteristics and fungal antagonism of tensin – a new antifungal cyclic lipopeptide from Pseudomonas fluorescens strain 96.578**. *Journal of Applied Microbiology*, *89*(6), 992–1001.

Ogran, A., Yardeni, E. H., Keren-Paz, A., Bucher, T., Jain, R., Gilhar, O., & Kolodkin-Gal, I. (2019). **The plant host induces antibiotic production to select the most-beneficial colonizers.** *Applied and Environmental Microbiology*, *85*(13).

Osbourn, A. E. (1996). **Preformed Antimicrobial Compounds and Plant Defense against Funga1 Attack**. *The Plant Cell*, *8*, 1821–1831.

Palma, M., Worgall, S., & Quadri, L. E. N. (2003). **Transcriptome analysis of the Pseudomonas aeruginosa response to iron.** *Archives of Microbiology 2003 180:5*, *180*(5), 374–379.

Pascale, A., Proietti, S., Pantelides, I. S., & Stringlis, I. A. (2020). **Modulation of the Root Microbiome by Plant Molecules: The Basis for Targeted Disease Suppression and Plant Growth Promotion.** *Frontiers in Plant Science*, *10*, 1741.

Peypoux, F., Bonmatin, J. M., & Wallach, J. (1999). **Recent trends in the biochemistry of surfactin.** *Applied Microbiology and Biotechnology 1999 51:5*, *51*(5), 553–563.

Pfeilmeier, S., Petti, G. C., Bortfeld-Miller, M., Daniel, B., Field, C. M., Sunagawa, S., & Vorholt, J. A. (2021). T**he plant NADPH oxidase RBOHD is required for microbiota homeostasis in leaves.** *Nature Microbiology*, *6*(7), 852–864

Pieterse, C. M. J., van der Does, D., Zamioudis, C., Leon-Reyes, A., & van Wees, S. C. M. (2012). **Hormonal Modulation of Plant Immunity**. *Annurev-Cellbio*, *28*, 489–521.

Pohlert, T. (2022). **Calculate Pairwise Multiple Comparisons of Mean Rank Sums Extended** *[R package PMCMRplus version 1.9.6]*.

Purtschert-Montenegro, G., Cárcamo-Oyarce, G., Pinto-Carbó, M., Agnoli, K., Bailly, A., & Eberl, L. (2022). **Pseudomonas putida mediates bacterial killing, biofilm invasion and biocontrol with a type IVB secretion system**. *Nature Microbiology 2022 7:10*, *7*(10), 1547–1557.

Raaijmakers, J. M., de Bruijn, I., Nybroe, O., & Ongena, M. (2010). **Natural functions of lipopeptides from Bacillus and Pseudomonas: more than surfactants and antibiotics**. *FEMS Microbiology Reviews*, *34*(6), 1037–1062.

Raaijmakers, J. M., & Weller, D. M. (2007). **Natural Plant Protection by 2,4-Diacetylphloroglucinol-Producing Pseudomonas spp. in Take-All Decline Soils**. *MPMI*, *11*(2), 144–152.

Rahme, L. G., Stevens, E. J., Wolfort, S. F., Shao, J., Tompkins, R. G., & Ausubel, F. M. (1995). **Common virulence factors for bacterial pathogenicity in plants and animals.** *Science*, *268*(5219), 1899–1902.

Rajniak, J., Giehl, R. F. H., Chang, E., Murgia, I., von Wirén, N., & Sattely, E. S. (2018). **Biosynthesis of redox-active metabolites in response to iron deficiency in plants**. *Nature Chemical Biology 2018 14:5*, *14*(5), 442–450.

Ramírez-puebla, S. T., Servín-Garcidueñas, L. E., Jiménez-marín, B., Bolaños, L. M., Rosenblueth, M., Martínez, J., Rogel, M. A., Ormeño-orrillo, E., & Martínez-romero, E. (2013). **Gut and Root Microbiota Commonalities**. *Applied and Environmental Microbiology*, *79*(1), 2–9.

Records, A. R. (2011). **The Type VI Secretion System: A Multipurpose Delivery System with a Phage-Like Machinery**. *MPMI*, *24*(7), 751–757.

Russell, A. B., Peterson, S. B., & Mougous, J. D. (2014). **Type VI secretion system effectors: poisons with a purpose.** *Nature Reviews Microbiology 2014 12:2*, *12*(2), 137–148.

Rutledge, P. J., & Challis, G. L. (2015). **Discovery of microbial natural products by activation of silent biosynthetic gene clusters.** *Nature Reviews Microbiology 2015 13:8*, *13*(8), 509–523.

Santhanam, R., Luu, V. T., Weinhold, A., Goldberg, J., Oh, Y., & Baldwin, I. T. (2015**). Native root-associated bacteria rescue a plant from a sudden-wilt disease that emerged during continuous cropping.** *Proceedings of the National Academy of Sciences of the United States of America*, *112*(36), E5013–E5120.

Santos-Medellín, C., Liechty, Z., Edwards, J., Nguyen, B., Huang, B., Weimer, B. C., & Sundaresan, V. (2021). **Prolonged drought imparts lasting compositional changes to the rice root microbiome.** *Nature Plants 2021 7:8*, *7*(8), 1065–1077.

Savary, S., Willocquet, L., Pethybridge, S. J., Esker, P., McRoberts, N., & Nelson, A. (2019). **The global burden of pathogens and pests on major food crops.** *Nature Ecology & Evolution*, *3*(3), 430–439.

Schellenberg, B., Ramel, C., & Dudler, R. (2010). **Pseudomonas syringae virulence factor syringolin A counteracts stomatal immunity by proteasome inhibition.** *Molecular Plant-Microbe Interactions : MPMI*, *23*(10), 1287–1293.

Scholz-Schroeder, B. K., Hutchison, M. L., Grgurina, I., & Gross, D. C. (2001). **The contribution of syringopeptin and syringomycin to virulence of Pseudomonas syringae pv. syringae strain B301D on the basis of sypA and syrB1 biosynthesis mutant analysis.** *Molecular Plant-Microbe Interactions*, *14*(3), 336–348.

Schroth, M. N., & Hancock, J. G. (1982). **Disease-Suppressive Soil and Root-Colonizing Bacteria**. *Science*, *216*(4553), 1376–1381.

Schwyn, B., & Neilands, J. B. (1987). **Universal chemical assay for the detection and determination of siderophores.** *Analytical Biochemistry*, *160*(1), 47–56.

Seemann, T. (2014). **Prokka: rapid prokaryotic genome annotation.** *Bioinformatics (Oxford, England)*, *30*(14), 2068–2069.

Seppey, M., Manni, M., & Zdobnov, E. M. (2019). **BUSCO: Assessing genome assembly and annotation completeness.** *Methods in Molecular Biology*, *1962*, 227–245.

Shannon, P., Markiel, A., Ozier, O., Baliga, N. S., Wang, J. T., Ramage, D., Amin, N., Schwikowski, B., & Ideker, T. (2003). **Cytoscape: a software environment for integrated models of biomolecular interaction networks**. *Genome Research*, *13*(11), 2498–2504.

Shtienberg, D., & Elad, Y. (2007). **Incorporation of Weather Forecasting in Integrated, Biological-Chemical Management of Botrytis cinerea**. *PHYTO*, *87*(3), 332–340.

Sivakumaran, A., Akinyemi, A., Mandon, J., Cristescu, S. M., Hall, M. A., Harren, F. J. M., & Mur, L. A. J. (2016**). ABA suppresses botrytis cinerea elicited NO production in tomato to influence H2O2 generation and increase host susceptibility**. *Frontiers in Plant Science*, *7*(MAY2016), 709.

Song, Y., Wilson, A. J., Zhang, X. C., Thoms, D., Sohrabi, R., Song, S., Geissmann, Q., Liu, Y., Walgren, L., He, S. Y., & Haney, C. H. (2021). **FERONIA restricts Pseudomonas in the rhizosphere microbiome via regulation of reactive oxygen species**. *Nature Plants 2021 7:5*, *7*(5), 644–654.

Sprouffske, K., & Wagner, A. (2016). **Growthcurver: An R package for obtaining interpretable metrics from microbial growth curves**. *BMC Bioinformatics*, *17*(1), 1–4.

Stevens, R. B. (1960). **Plant Pathology, an Advanced Treatise**. In *Plant Pathology, an Advanced Treatise : Vol. Vol. 3* (pp. 357–429). J.G. Horsfall and A.E. Dimond, eds. Academic Press, NY.

Tedersoo, L., Bahram, M., Põlme, S., Kõljalg, U., Yorou, N. S., Wijesundera, R., Ruiz, L. V., Vasco-Palacios, A. M., Thu, P. Q., Suija, A., Smith, M. E., Sharp, C., Saluveer, E., Saitta, A., Rosas, M., Riit, T., Ratkowsky, D., Pritsch, K., Põldmaa, K., Abarenkov, K. (2014). **Global diversity and geography of soil fungi.** *Science*, *346*(6213).

Teixeira, P. J. P., Colaianni, N. R., Fitzpatrick, C. R., & Dangl, J. L. (2019). **Beyond pathogens: microbiota interactions with the plant immune system.** *Current Opinion in Microbiology*, *49*, 7–17.

Teixeira, P. J. P. L., Colaianni, N. R., Law, T. F., Conway, J. M., Gilbert, S., Li, H., Salas-González, I., Panda, D., del Risco, N. M., Finkel, O. M., Castrillo, G., Mieczkowski, P., Jones, C. D., & Dangl, J. L. (2021). **Specific modulation of the root immune system by a community of commensal bacteria**. *Proceedings of the National Academy of Sciences of the United States of America*, *118*(16), e2100678118.

Thiergart, T., Durán, P., Ellis, T., Vannier, N., Garrido-Oter, R., Kemen, E., Roux, F., Alonso-Blanco, C., Ågren, J., Schulze-Lefert, P., & Hacquard, S. (2019). **Root microbiota assembly and adaptive differentiation among European Arabidopsis populations.** *Nature Ecology & Evolution 2019 4:1*, *4*(1), 122–131.

Timilsina, S., Potnis, N., Newberry, E. A., Liyanapathiranage, P., Iruegas-Bocardo, F., White, F. F., Goss, E. M., & Jones, J. B. (2020). **Xanthomonas diversity, virulence and plant–pathogen interactions.** *Nature Reviews Microbiology 2020 18:8*, *18*(8), 415–427.

Torres, M. A., Dangl, J. L., & Jones, J. D. G. (2002). **Arabidopsis gp91phox homologues Atrbohd and Atrbohf are required for accumulation of reactive oxygen intermediates in the plant defense response.** *Proceedings of the National Academy of Sciences of the United States of America*, *99*(1), 517–522.

Tracanna, V., Ossowicki, A., Petrus, M. L. C., Overduin, S., Terlouw, B. R., Lund, G., Robinson, S. L., Warris, S., Schijlen, E. G. W. M., van Wezel, G. P., Raaijmakers, J. M., Garbeva, P., & Medema, M. H. (2021). **Dissecting Disease-Suppressive Rhizosphere Microbiomes by Functional Amplicon Sequencing and 10× Metagenomics**. *MSystems*, *6*(3).

Tringe, S. G., von Mering, C., Kobayashi, A., Salamov, A. A., Chen, K., Chang, H. W., Podar, M., Short, J. M., Mathur, E. J., Detter, J. C., Bork, P., Hugenholtz, P., & Rubin, E. M. (2005). **Comparative metagenomics of microbial communities.** *Science*, *308*(5721), 554–557.

Trivedi, P., Leach, J. E., Tringe, S. G., Sa, T., & Singh, B. K. (2020). **Plant–microbiome interactions: from community assembly to plant health.** *Nature Reviews Microbiology 2020 18:11*, *18*(11), 607–621.

Vlot, A. C., Sales, J. H., Lenk, M., Bauer, K., Brambilla, A., Sommer, A., Chen, Y., Wenig, M., & Nayem, S. (2021). **Systemic propagation of immunity in plants.** *New Phytologist*, *229*(3), 1234–1250.

Vorholt, J. A. (2012). **Microbial life in the phyllosphere.** *Nature Reviews Microbiology 2012 10:12*, *10*(12), 828–840.

Wagner, S., Grin, I., Malmsheimer, S., Singh, N., Torres-Vargas, C. E., & Westerhausen, S. (2018). **Bacterial type III secretion systems: a complex device for the delivery of bacterial effector proteins into eukaryotic host cells**. *FEMS Microbiology Letters*, *365*(19), 201.

Wang, L., Linares-Otoya, V., Liu, Y., Mettal, U., Marner, M., Armas-Mantilla, L., Willbold, S., Kurtán, T., Linares-Otoya, L., & Schäberle, T. F. (2022**). Discovery and Biosynthesis of Antimicrobial Phenethylamine Alkaloids from the Marine Flavobacterium Tenacibaculum discolor sv11.** *Journal of Natural Products*, *85*(4), 1039–1051.

Wang, M., Carver, J. J., Phelan, V. v., Sanchez, L. M., Garg, N., Peng, Y., Nguyen, D. D., Watrous, J., Kapono, C. A., Luzzatto-Knaan, T., Porto, C., Bouslimani, A., Melnik, A. v., Meehan, M. J., Liu, W. T., Crüsemann, M., Boudreau, P. D., Esquenazi, E., Sandoval-Calderón, M., Bandeira, N. (2016). **Sharing and community curation of mass spectrometry data with Global Natural Products Social Molecular Networking**. *Nature Biotechnology*, *34*(8), 828–837.

Warmink, J. A., Nazir, R., & van Elsas, J. D. (2009). **Universal and species-specific bacterial 'fungiphiles' in the mycospheres of different basidiomycetous fungi**. *Environmental Microbiology*, *11*(2), 300–312.

Weeraratne, N., Stodart, B. J., Venturi, V., Hofte, M., Hua, G. K. H., Ongena, M., Savocchia, S., Steel, C. C., & Ash, G. J. (2020). **Syringopeptin contributes to the virulence of pseudomonas fuscovaginae, based on sypA biosynthesis mutant analysis**. *Phytopathology*, *110*(4), 780–789.

Wei, Z., Gu, Y., Friman, V. P., Kowalchuk, G. A., Xu, Y., Shen, Q., & Jousset, A. (2019). **Initial soil microbiome composition and functioning predetermine future plant health**. *Science Advances*, *5*(9), 759–784.

Wei, Z., Yang, T., Friman, V. P., Xu, Y., Shen, Q., & Jousset, A. (2015). **Trophic network architecture of root-associated bacterial communities determines pathogen invasion and plant health.** *Nature Communications 2015 6:1*, *6*(1), 1–9.

Wensing, A., Braun, S. D., Büttner, P., Expert, D., Völksch, B., Ullrich, M. S., & Weingart, H. (2010). **Impact of siderophore production by pseudomonas syringae pv. syringae 22d/93 on epiphytic fitness and biocontrol Activity against Pseudomonas syringae pv. glycinea 1a/96.** *Applied and Environmental Microbiology*, *76*(9), 2704–2711.

Whitaker, B. K., & Bakker, M. G. (2019). **Bacterial endophyte antagonism toward a fungal pathogen in vitro does not predict protection in live plant tissue.** *FEMS Microbiology Ecology*, *95*(2).

Wick, R. R., Schultz, M. B., Zobel, J., & Holt, K. E. (2015). **Bandage: interactive visualization of de novo genome assemblies.** *Bioinformatics*, *31*(20), 3350–3352.

Wintermute, E. H., & Silver, P. A. (2010). **Emergent cooperation in microbial metabolism.** *Molecular Systems Biology*, *6*(1), 407.

Wippel, K., Tao, K., Niu, Y., Zgadzaj, R., Kiel, N., Guan, R., Dahms, E., Zhang, P., Jensen, D. B., Logemann, E., Radutoiu, S., Schulze-Lefert, P., & Garrido-Oter, R. (2021). **Host preference and invasiveness of commensal bacteria in the Lotus and Arabidopsis root microbiota**. *Nature Microbiology 2021 6:9*, *6*(9), 1150–1162.

Wolinska, K. W., Vannier, N., Thiergart, T., Pickel, B., Gremmen, S., Piasecka, A., Piślewska-Bednarek, M., Nakano, R. T., Belkhadir, Y., Bednarek, P., & Hacquard, S. (2021). **Tryptophan metabolism and bacterial commensals prevent fungal dysbiosis in Arabidopsis roots**. *Proceedings of the National Academy of Sciences of the United States of America*, *118*(49), e2111521118.

Worrich, A., König, S., Miltner, A., Banitz, T., Centler, F., Frank, K., Thullner, M., Harms, H., Kästner, M., & Wick, L. Y. (2016). **Mycelium-like networks increase bacterial dispersal, growth, and biodegradation in a model ecosystem at various water potentials**. *Applied and Environmental Microbiology*, *82*(10), 2902–2908.

Xin, X. F., Nomura, K., Aung, K., Velásquez, A. C., Yao, J., Boutrot, F., Chang, J. H., Zipfel, C., & He, S. Y. (2016). **Bacteria establish an aqueous living space in plants crucial for virulence**. *Nature 2016 539:7630*, *539*(7630), 524–529.

Xu, F., Liao, H., Zhang, Y., Yao, M., Liu, J., Sun, L., Zhang, X., Yang, J., Wang, K., Wang, X., Ding, Y., Liu, C., Rensing, C., Zhang, J., Yeh, K., & Xu, W. (2021). **Coordination of root auxin with the fungus Piriformospora indica and bacterium Bacillus cereus enhances rice rhizosheath formation under soil drying**. *The ISME Journal 2021 16:3*, *16*(3), 801–811.

Xu, L., Dong, Z., Chiniquy, D., Pierroz, G., Deng, S., Gao, C., Diamond, S., Simmons, T., Wipf, H. M. L., Caddell, D., Varoquaux, N., Madera, M. A., Hutmacher, R., Deutschbauer, A., Dahlberg, J. A., Guerinot, M. lou, Purdom, E., Banfield, J. F., Taylor, J. W., Coleman-Derr, D. (2021). **Genome-resolved metagenomics reveals role of iron metabolism in drought-induced rhizosphere microbiome dynamics.** *Nature Communications 2021 12:1*, *12*(1), 1–17.

Yasuda, M., Ishikawa, A., Jikumaru, Y., Seki, M., Umezawa, T., Asami, T., Maruyama-Nakashita, A., Kudo, T., Shinozaki, K., Yoshida, S., & Nakashita, H. (2008). **Antagonistic Interaction between Systemic Acquired Resistance and the Abscisic Acid–Mediated Abiotic Stress Response in Arabidopsis**. *The Plant Cell*, *20*(6), 1678–1692.

Yu, K., Liu, Y., Tichelaar, R., Savant, N., Lagendijk, E., van Kuijk, S. J. L., Stringlis, I. A., van Dijken, A. J. H., Pieterse, C. M. J., Bakker, P. A. H. M., Haney, C. H., & Berendsen, R. L. (2019). **Rhizosphere-Associated Pseudomonas Suppress Local Root Immune Responses by Gluconic Acid-Mediated Lowering of Environmental pH**. *Current Biology*, *29*(22), 3913-3920.e4.

Yuan, J., Zhao, J., Wen, T., Zhao, M., Li, R., Goossens, P., Huang, Q., Bai, Y., Vivanco, J. M., Kowalchuk, G. A., Berendsen, R. L., & Shen, Q. (2018). **Root exudates drive the soil-borne legacy of aboveground pathogen infection.** *Microbiome*, *6*(1), 1–12.

Zgadzaj, R., Garrido-Oter, R., Jensen, D. B., Koprivova, A., Schulze-Lefert, P., & Radutoiu, S. (2016). **Root nodule symbiosis in Lotus japonicus drives the establishment of distinctive rhizosphere, root, and nodule bacterial communities.** *Proceedings of the National Academy of Sciences of the United States of America*, *113*(49), E7996–E8005.

Zhang, P., Spaepen, S., Bai, Y., Hacquard, S., & Garrido-Oter, R. (2021). **Rbec: a tool for analysis of amplicon sequencing data from synthetic microbial communities.** *ISME Communications 2021 1:1*, *1*(1), 1–3.

Zhang, Y., Kastman, E. K., Guasto, J. S., & Wolfe, B. E. (2018). **Fungal networks shape dynamics of bacterial dispersal and community assembly in cheese rind microbiomes**. *Nature Communications 2018 9:1*, *9*(1), 1–12.

Zhang, Y., & Li, X. (2019). **Salicylic acid: biosynthesis, perception, and contributions to plant immunity.** *Current Opinion in Plant Biology*, *50*, 29–36.

Zhang, Y., Zhu, H., Zhang, Q., Li, M., Yan, M., Wang, R., Wang, L., Welti, R., Zhang, W., & Wang, X. (2009). **Phospholipase Dα1 and Phosphatidic Acid Regulate NADPH Oxidase Activity and Production of Reactive Oxygen Species in ABA-Mediated Stomatal Closure in Arabidopsis**. *The Plant Cell*, *21*(8), 2357–2377.

Zhang, Z., & Yuen, G. Y. (2007). **The Role of Chitinase Production by Stenotrophomonas maltophilia Strain C3 in Biological Control of Bipolaris sorokiniana**. *PHYTO*, *90*(4), 384–389.

Zhou, H., Wei, H., Liu, X., Wang, Y., Zhang, L., & Tang, W. (2005). **Improving biocontrol activity of Pseudomonas fluorescens through chromosomal integration of 2,4-diacetylphloroglucinol biosynthesis genes.** *Chinese Science Bulletin 2005 50:8*, *50*(8), 775–781.

Zhou, T. T., Li, C. Y., Chen, D., Wu, K., Shen, Q. R., & Shen, B. (2014). **phlF− mutant of Pseudomonas fluorescens J2 improved 2,4-DAPG biosynthesis and biocontrol efficacy against tomato bacterial wilt.** *Biological Control*, *78*, 1–8.

Zhou, Y., Zhou, B., Pache, L., Chang, M., Khodabakhshi, A. H., Tanaseichuk, O., Benner, C., & Chanda, S. K. (2019). **Metascape provides a biologist-oriented resource for the analysis of systems-level datasets.** *Nature Communications*, *10*(1).

Zhu, A., Ibrahim, J. G., & Love, M. I. (2019). **Heavy-tailed prior distributions for sequence count data: removing the noise and preserving large differences**. *Bioinformatics (Oxford, England)*, *35*(12), 2084–2092.

Zhu, J. K. (2002). **Salt and Drought Stress Signal Transduction in Plants.** *Annual Review of Plant Biology*, *53*, 247.

Zhu, J. K. (2016). **Abiotic Stress Signaling and Responses in Plants**. *Cell*, *167*(2), 313–324.

Acknowledgements

First and foremost, I would like to thank Dr. Stéphane Hacquard for providing me with the opportunity to carry out the research for this PhD thesis in his group and for providing me with the freedom to develop my own ideas and guidance when needed. In line with this, I am grateful for the close collaborations with Prof. Dr. Paul Schulze-Lefert, his financial support, and his scientific guidance throughout my PhD. I thank my other Thesis Advisory Committee members Prof. Dr. Alga Zuccaro and Dr. Thomas Nakano for their valuable suggestions and Prof. Dr. Till F. Schäberle and his research group for supporting this research with various metabolomic analyses. Similarly, I am grateful for all collaborators that contributed to data analysis, data acquisition or data interpretation.

I thank all members of the Plant-Microbe Interaction department at Max Planck Institute for Plant Breeding Research, mainly the 'Rooters', who always provided critical feedback. I want to thank the current and former members of the 'AG Hacquard', especially Brigitte Pickel for her great support during experiments.

I am very grateful for the technical support I received from the everyone working in the media kitchen, Elke Logemann, Diana Dresbach, and the MPIPZ genome centre – especially Dr. Bruno Hüttel. I thank Meagan Sierz, Sabine Goertz and Priska Dormels for their help with various bureaucratic hurdles. And I am very thankful for Dr. Neysan Donnelly's feedback on text drafts, including this thesis.

I thank the IMPRS for funding the first year of my PhD and especially PhD coordinator Dr. Stephan Wagner for his seemingly endless support of me and all other PhD students at the MPIPZ.

I want to thank my amazing office for all scientific and non-scientific conversations, especially Jana Ordon for enduring the highs and lows of a PhD with me.

Finally, I am grateful for Prof. Dr. Paul Schulze-Lefert and Prof. Stanislav Kopriva who kindly accepted to evaluate this thesis.